



Publication Year	2015
Acceptance in OA	2020-05-15T13:50:26Z
Title	Plasma Sources in Planetary Magnetospheres: Mercury
Authors	Raines, J. M., DiBraccio, G. A., Cassidy, T. A., Delcourt, D. C., Fujimoto, M., Jia, X., MANGANO, VALERIA, MILILLO, Anna, Sarantos, M., Slavin, J. A., Wurz, P.
Publisher's version (DOI)	10.1007/s11214-015-0193-4
Handle	http://hdl.handle.net/20.500.12386/24876
Journal	SPACE SCIENCE REVIEWS
Volume	192

1 Plasma Sources in Planetary 2 Magnetospheres: Mercury

3
4 *J.M. Raines(1), G.A. DiBraccio(1,2), T.A. Cassidy(3), D.C.*
5 *Delcourt(4), M. Fujimoto(5), X. Jia(1), V. Mangano(6), A. Milillo(6), M.*
6 *Sarantos(7), J.A. Slavin(1), P. Wurz(8)*

- 7
8 (1) Department of Atmospheric, Oceanic and Space Sciences, University of
9 Michigan, Ann Arbor, MI, 48109., USA.
10 (2) Solar System Exploration Divison, NASA Goddard Space Flight Center,
11 Greenbelt, MD, 20771, USA.
12 (3) Laboratory for Atmospheric and Space Physics, University of Colorado, Boulder,
13 CO, 80303, USA.
14 (4) LPP, Ecole Polytechnique-CNRS, Université Pierre et Marie Curie, 4 Place
15 Jussieu, 75252 Paris, France.
16 (5) ISAS, Kanagawa, Japan
17 (6) Institute of Space Astrophysics and Planetology, INAF, Rome, Italy.
18 (7) Heliophysics Science Division, NASA Goddard Space Flight Center, Greenbelt,
19 MD, USA.
20 (8) Physics Institute, University of Bern, CH-3012 Bern, Switzerland.

21 **1 Introduction**

22 The proximity of Mercury to the Sun makes this planet a particularly
23 interesting subject because of the extreme environmental conditions that led to its
24 unique evolutionary history. Mercury's present plasma environment has its
25 foundation in a weak intrinsic global magnetic field that supports a small, but
26 dynamic, magnetosphere. The plasma in Mercury's space environment coexists with
27 the planet's exosphere and strongly interacts with the surface. In fact, Mercury's
28 environment is a complex and tightly coupled system where the magnetosphere,
29 exosphere, and surface are linked by interaction processes that facilitate material
30 production and energy exchange [Killen and Ip, 1999; Killen et al., 2007; Milillo et
31 al., 2010]. Investigations regarding the coupling of Mercury's magnetosphere with the
32 interplanetary magnetic field (IMF) of the Sun, as well as the planet's interaction with
33 solar radiation (both electromagnetic and particle) and with interplanetary dust, can
34 provide important clues to the process of planetary evolution [Orsini et al., 2014].
35 The study of Mercury may reveal processes fundamental to the interpretation of
36 exoplanet observations: In fact, many discovered exoplanets are located only a few
37 stellar radii away from their parent star, even closer than Mercury is to the Sun. The
38 resulting effects and type of interactions in these particular situations are among the
39 key questions to be answered in the future.

40 The first in situ measurements provided by three flybys of Mariner 10 [Vilas et
41 al., 1988] in 1974–1975 revealed the weak, intrinsic magnetic field of Mercury that
42 gives rise to its small magnetosphere [for a review, see Russell et al., 1988; Wurz and
43 Blomberg, 2001; Slavin et al., 2007]. Plasma sheet electrons were measured during
44 the first flyby, though no ion measurements were made due to a hardware failure

45 [Ogilvie *et al.*, 1974]. After those measurements, the scientific community had to
46 wait almost 40 years until MErcury Surface, Space ENvironment, GEochemistry, and
47 Ranging (MESSENGER) was launched in August 2004 [Solomon *et al.*, 2007] and
48 became the first spacecraft to obtain systematic measurements by orbiting Mercury.
49 The MESSENGER magnetic field measurements indicate that Mercury's magnetic
50 dipole moment is offset northward from the planet's center by $0.2 R_M$ (where R_M is
51 Mercury's radius, or 2440 km) [Alexeev *et al.*, 2010; Anderson *et al.*, 2011]. Now we
52 know that Mercury's magnetosphere is highly dynamic [e.g., Slavin *et al.*, 2009,
53 2010; DiBraccio *et al.*, 2013], so it cannot be considered as a stable structure where
54 plasma distributes according to well-characterized populations, like in the Earth's
55 magnetosphere. At Mercury, no stable ring current is observed and magnetic storms
56 driven by adiabatic convection cannot develop. On the contrary, fast (few seconds)
57 events like Flux Transfer Events (FTEs) [Slavin *et al.*, 2012b], dipolarizations
58 [Sundberg *et al.*, 2012], plasmoids [Slavin *et al.*, 2012a; DiBraccio *et al.*, 2014] are
59 observed. Further, bursts of low- and moderate energy (tens to hundreds keV)
60 electrons [Ho *et al.*, 2012] are often recorded.

61 Together with the protons and He^{2+} of solar wind origin, MESSENGER's Fast
62 Imaging Plasma Spectrometer (FIPS) detected ions of planetary origin like He^+ , Na^+ -
63 Mg^+ and several other heavy ion species [Zurbuchen *et al.*, 2008] while Mercury
64 Atmospheric and Surface Composition Spectrometer (MASCS) UltraViolet and
65 Visible Spectrometer (UVVS) [McClintock *et al.*, 2007] mapped the Ca^+ tail on the
66 nightside [Vervack *et al.*, 2010]. In particular, on the dayside, a solar wind-
67 originating plasma population mixed with heavy planetary ions (Na^+ group) was
68 observed in the region of the magnetospheric cusp. On the nightside, plasma ions
69 were observed near the equator, in the central plasma sheet [Raines *et al.*, 2013].
70 Finally, increased plasma fluxes were observed in the magnetosheath as well as
71 sparsely distributed planetary ions that span the magnetopause boundary (as identified
72 in magnetic field measurements [Anderson *et al.*, 2012; Winslow *et al.*, 2013]). These
73 features are observed on nearly every orbit, despite highly variable solar wind and
74 IMF conditions [Gershman *et al.*, 2012; Baker *et al.*, 2013].

75 The solar wind and planetary ions interact with the surface to produce ion
76 sputtering, backscattering, and internal structure alteration via chemical sputtering
77 and/or enhanced diffusion [Mura *et al.*, 2009; Sarantos *et al.*, 2009]. The surface-
78 released material populates the neutral gas environment of Mercury as a tenuous and
79 non-collisional regime, constituting the exosphere.

80 The presence of neutral atoms in Mercury's environment was also discovered
81 during the Mariner 10 flybys; H, He, and O were detected in the atmosphere by the
82 onboard UV spectrometer [Broadfoot *et al.*, 1974]. Later, Na, K, and Ca were
83 detected through ground-based Earth observations [Potter and Morgan, 1985, 1986;
84 Bida *et al.*, 2000]. Doressoundiram *et al.* [2009] defined an upper limit for Al, Fe, and
85 Si by ground-based observations. Finally, MESSENGER UVVS provided a
86 systematic in situ detection of Na, Ca and Mg [McClintock *et al.*, 2009; Domingue *et al.*,
87 2007]. New ground-based observations and new methods and technologies [e.g.,
88 Leblanc *et al.*, 2008; Mangano *et al.*, 2013], coupled with simulations [e.g., Schmidt,
89 2013] permit the investigation of spatial and temporal variations in the exosphere,
90 providing insight to magnetospheric and solar activity variation dependencies. UVVS
91 measurements, surprisingly, have shown little exospheric response to magnetospheric
92 activity.

93 The most globally and systematically observed element at Mercury is Na,
94 since its doublet is relatively easy to detect through the Earth's atmosphere and its

95 abundance is high in Mercury's exosphere. A clear relation of Na distribution and its
96 variability has been observed throughout the exosphere. The Na exosphere peaks
97 frequently at mid-latitudes in the dayside, corresponding to the magnetic cusp regions
98 where solar wind plasma is able to access the planetary surface [e.g., *Killen et al.*,
99 2001]. Nevertheless, experimental results exclude that the yield of direct sputtering
100 can account for the observed Na intensity [*McGrath et al.*, 1986; *Johnson and*
101 *Baragiola*, 1991]. Modeling and recent Na temperature obtained by MESSENGER
102 show that Photon Stimulated Desorption (PSD) is by far the most efficient process to
103 release Na into the exosphere on the day side of Mercury [*Wurz et al.*, 2010; *Mura et*
104 *al.*, 2009; *Cassidy et al.*, 2015; *Sarantos et al.*, 2009], indicating that the processes are
105 independent from each other [*Leblanc et al.*, 2010; *Mura et al.*, 2009]. Also, the
106 measurements by MESSENGER UVVS have shown evidence that variation of global
107 intensity are well reproduced year by year [*Cassidy et al.*, 2015], showing that solar
108 wind action could account only for variation in the distribution, not in the global
109 exosphere density..

110 Mercury's exosphere is continuously emptied and filled through a variety of
111 chemical and physical processes acting on the planet's surface and environment
112 [*Killen et al.*, 2007; *Leblanc et al.*, 2007]. The neutral environment of the planet is not
113 only generated by plasma-surface interactions, but it also interacts with the circulating
114 plasma via charge exchange, and it also undergoes electron-impact and photo-
115 ionization, creating a population of low-energy ions. These newly generated ions are
116 accelerated [*Delcourt et al.*, 2003; *Seki et al.*, 2013] and contribute to the mini-
117 magnetosphere. At a further step, the ions are either lost into the solar wind or impact
118 again onto the surface.

119 Finally, we can conclude that the sources of the magnetospheric ions are
120 mostly solar wind plasma entering the magnetosphere, ionization of exospheric
121 species, and planetary ions from the surface. On the other hand, sinks of the ion
122 populations are the surface, where plasma directly impacts, and the solar wind, that
123 picks up ions as it flows past the planet. To evaluate the source and sink balance in
124 the Mercury environment, this global complex system should be investigated as a
125 whole.

126 The forthcoming ESA - JAXA BepiColombo mission to Mercury (to be
127 launched in 2016) [*Benkhoff et al.*, 2010], consists of two Mercury-orbiting spacecraft
128 to provide the opportunity for simultaneous two-point measurements. Thanks to this,
129 the BepiColombo mission will offer an unprecedented opportunity to deeply
130 investigate magnetospheric and exospheric dynamics at Mercury as well as their
131 interactions with solar radiation and interplanetary dust [*Milillo et al.*, 2010].

132 In the following sections of this chapter, the structure and dynamics of
 133 Mercury's magnetosphere are reviewed, with an emphasis on its local plasma
 134 environment. We examine both global and kinetic features that have been identified
 135 through magnetic field and plasma observations, organized into plasma sources and
 136 losses, as well as the exosphere and the surface processes that generate it. Finally, we
 137 discuss the contribution that modeling has made to our understanding of Mercury's
 138 magnetosphere and of the behavior of its plasma populations.

139 2 Magnetospheric Structure and Dynamics

140 2.1 Global Magnetosphere Configuration

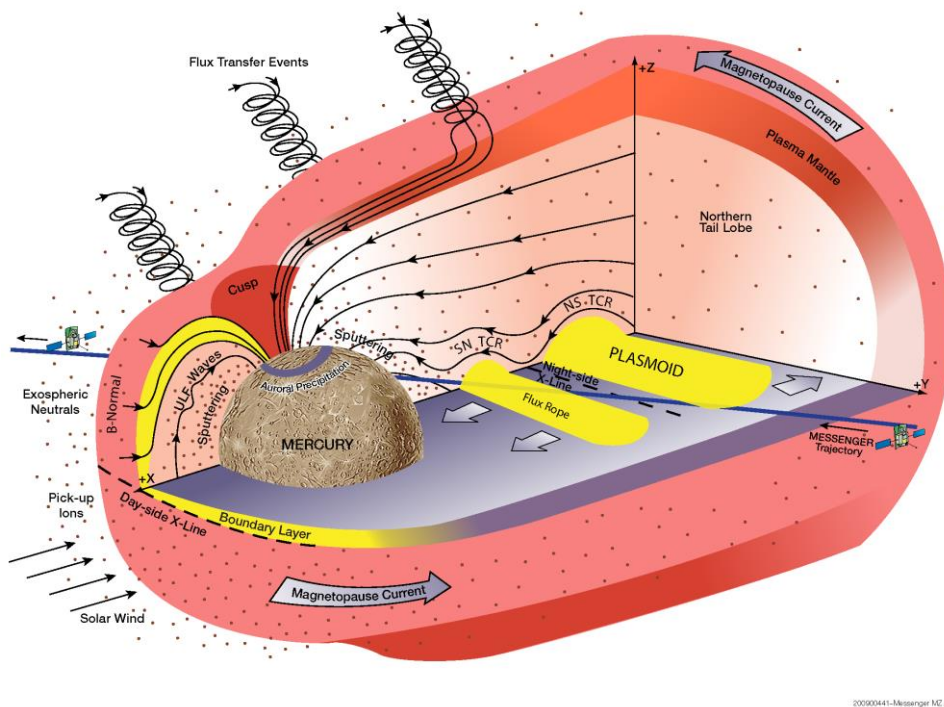


Figure 1. Schematic of Mercury's Dungey cycle. This large-scale magnetospheric convection, responsible for the circulation of plasma and magnetic flux, is driven by steady and impulsive reconnection. Note the strong magnetic field normal to the dayside magnetopause, the large FTEs, and the reconnection line in the near-tail region. Figure from Slavin et al. [2009].

141 The magnetosphere of Mercury is of interest in many respects. It is
 142 characterized by spatial and temporal scales much smaller than those at Earth (by a
 143 factor of 8 and 30, respectively [e.g., Russell and Walker, 1985]). Boundary
 144 conditions also are quite different as compared to those at Earth with a dense solar
 145 wind and B_x dominated IMF at the outer boundary as well as a tenuous atmosphere at
 146 the inner boundary. Mercury's intrinsic magnetic field has a dipole moment of 195
 147 nT- R_M^3 , that is aligned to within 3 deg of the planet's spin-axis but has a northward
 148 offset of 484 km [Anderson et al., 2011]. As the supersonic, super-Alfvénic solar
 149 wind interacts with Mercury's intrinsic magnetic field, a planetary magnetosphere
 150 with an elongated magnetotail is formed. There are, however, notable differences
 151 between Mercury's magnetosphere and those of other planets with intrinsic magnetic
 152 field: Mercury possesses only a very tenuous exosphere consisting of planetary
 153 atoms, with some of them being ionized from the high solar radiation at Mercury's

154 orbit [Zurbuchen *et al.*, 2008, 2011; Raines *et al.*, 2011, 2013]. The lack of a
155 conducting ionosphere implies that any field-aligned currents must close through the
156 planet's regolith [Anderson *et al.*, 2014]. The solar wind is much more intense at
157 Mercury's orbit than at any other planet of the solar system [Burlaga, 2001].
158 Although the solar wind velocity remains relatively constant throughout the
159 heliosphere, its density at Mercury's orbit is 5–10 times larger than typical values at
160 Earth. Additionally, the strength of the IMF is, on average, about 30 nT, increasing
161 the solar wind Alfvén speed and enhancing the rate of reconnection with Mercury's
162 magnetic field [Slavin and Holzer, 1979].

163 The combination of Mercury's small dipole moment with the extreme solar
164 parameters results in a small but dynamic magnetosphere (Figure 1). In terms of
165 planetary radii, the planet Mercury accounts for a much larger volume of its
166 magnetosphere than Earth. At Mercury, the average subsolar magnetopause standoff
167 distance is $\sim 1.45 R_M$ [Winslow *et al.*, 2013] where the typical standoff distance is ~ 10
168 R_E at Earth [Fairfield, 1971]. Upstream of the magnetosphere, Mercury's bow shock
169 is located at an average distance of $1.96 R_M$ away from the planet [Winslow *et al.*,
170 2013]. Due to the low Alfvénic Mach number (M_A) and low β , the ratio of plasma
171 pressure to magnetic pressure, solar wind conditions at Mercury's orbit, the bow
172 shock is weaker and exhibits smaller magnetic overshoots compared to the outer
173 planets [Masters *et al.*, 2013].

174 Like Earth, the open-closed field line boundaries of Mercury's magnetosphere
175 map to high latitude, dayside magnetospheric cusps. The northern cusp is evident in
176 both MESSENGER plasma and magnetic field data in the vast majority of orbits that
177 cross the region. MESSENGER's passages over southern cusp were at much larger
178 altitudes and can only be indirectly inferred from measurements. The cusp appears as
179 a strong enhancement in plasma flux, composed of solar wind and planetary ions
180 [Zurbuchen *et al.*, 2011; Raines *et al.*, 2013] standing between two regions of much
181 lower plasma density. These enhancements span Mercury latitudes $\sim 30^\circ$ – 80° N and
182 local times 6–14 h. The cusp is manifested in magnetic field data mainly as
183 depressions in the field, attributed to the diamagnetic influence of the plasma present
184 there. Winslow *et al.* [2012] performed a statistical analysis of these depressions.
185 Their analysis showed that the cusp is a broad, highly variable region located around
186 56° – 84° N magnetic latitude and 7–16 h local time, marking a similar region on
187 Mercury's dayside as the plasma enhancements inferred from diamagnetic
188 depressions. This spatial extent is more similar to the V-shaped outer cusp at Earth
189 than the narrow cleft found at lower altitudes [Smith and Lockwood, 1996; Lavraud *et al.*
190 *et al.*, 2005].

191 Ion measurements from MESSENGER's first Mercury flyby confirmed that
192 Mercury's magnetosphere has an Earth-like central plasma sheet [Raines *et al.*, 2011].
193 The trajectory of this flyby was unique in that it passed nearby and almost parallel to
194 Mercury's equatorial plane, providing an opportunity to observe across the plasma
195 sheet not available in the orthogonal passes provided throughout the orbital phase.
196 Those authors compared measurements at Mercury to a long baseline study of the
197 plasma sheet at Earth [Baumjohann and Paschmann, 1989]. Accounting for the
198 expected 5–10 fold higher solar wind densities at Mercury's orbit in the heliosphere,
199 the measured proton density in Mercury's plasma sheet of 1 – 12 cm^{-3} , was comparable
200 with those at Earth (0.2 – 0.5 cm^{-3}) during similarly quiet magnetospheric conditions.
201 Proton temperature was much lower than the average at Earth, 2 MK versus 30–56
202 MK, respectively. Plasma beta, the ratio of magnetic to plasma pressure, was also
203 found to be lower and more steady at ~ 2 in Mercury's central plasma sheet. At the

204 Earth, plasma beta varies from ~ 0.3 near the edges of the plasma sheet, to ~ 30 in the
205 center. More details concerning plasma sheet observations are included in Section 3
206 below.

207 **2.1.1 Plasma depletion layers**

208 The low- β conditions in Mercury's magnetosheath are further exacerbated by
209 the frequent presence of plasma depletion layers (PDLs), caused by the draping and
210 compression of the IMF as it encounters the magnetopause boundary (Figure 2). This
211 concept of PDLs was initially introduced by *Zwan and Wolf* [1976], who predicted
212 that the natural draping of the IMF would lead to the formation of low- β layers
213 adjacent to the dayside magnetopause which they termed plasma depletion layers. It
214 was also predicted that the PDL thickness would be larger for low M_A and β
215 conditions, when magnetic pressure is dominating the magnetosheath, as is the case at
216 Mercury [*Zwan and Wolf*, 1976]. Consistent with this prediction, *Gershman et al.*
217 [2013] analyzed MESSENGER MAG and FIPS measurements to determine that
218 lower upstream M_A ($M_A \sim 3-5$) values led to stronger depletion effects in the PDLs at
219 Mercury. In this study, *Gershman et al.* [2013] identified 40 orbits where a PDL,
220 adjacent to the dayside magnetopause, was observed as MESSENGER crossed
221 through the magnetosheath. A typical PDL thickness was determined to be ~ 300 km,
222 or $\sim 0.12 R_M$. The PDLs were observed for both quasi-perpendicular and quasi-parallel
223 shock geometries as well as for all IMF orientations. Despite the high frequency of
224 reconnection occurring at Mercury's dayside magnetopause due to the low- β
225 environment [*DiBraccio et al.*, 2013], this substantial reconnection is not sufficient
226 enough to transport all of the magnetic flux pileup and therefore the PDLs are a
227 persistent feature of Mercury's magnetosheath. However, *Gershman et al.* [2013] also
228 concluded that plasma depletion does not appear to exist during times of extended
229 northward IMF.
230

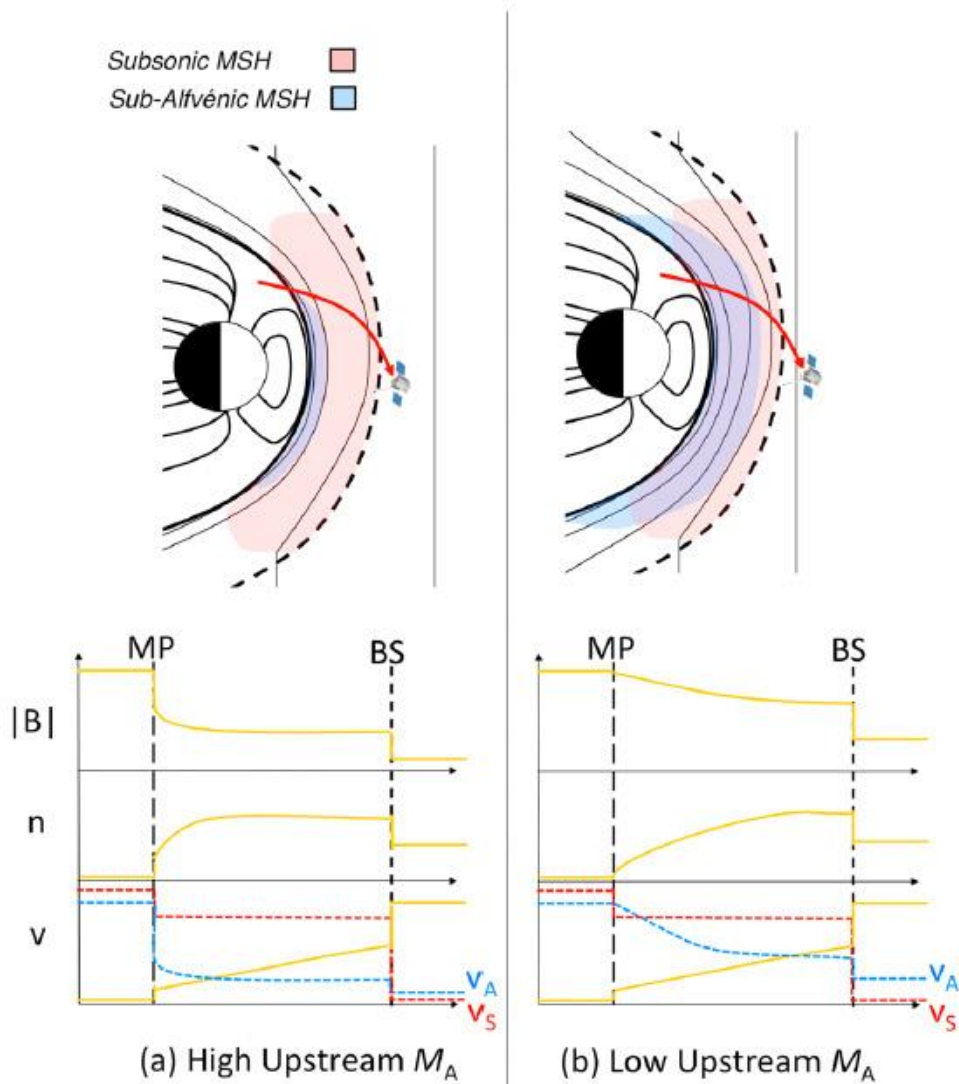


Figure 2. Illustration of a spacecraft pass through the subsolar magnetosheath (MSH) for (a) high solar wind Mach number (M_A) and (b) low solar wind M_A . The MSH plasma is subsonic equatorward of the approximately $\pm 45^\circ$ latitude. With decreasing M_A , a larger fraction of the subsolar magnetosheath is sub-Alfvénic, as indicated by the blue shaded region. In addition, a thicker region of magnetic flux pileup is evident by an increase in $|\mathbf{B}|$ and a decrease in plasma density, n . The Alfvén speed (V_A) and sound speed (V_S) are also shown for both cases. *Adapted from Gershman et al., 2013.*

231

232 2.1.2 Observations of induction effects

233 Given the mean subsolar magnetopause distance of only $1.45 R_M$ from the
 234 center of the planet [Winslow et al., 2013] and the high magnetopause reconnection
 235 rate [Slavin et al., 2009; DiBraccio et al., 2013], it seems reasonable to conclude that
 236 Mercury's surface may become directly exposed to the solar wind. Slavin and Holzer
 237 [1979] predicted that the low- M_A nature of Mercury's space environment, especially
 238 during periods of high solar wind pressure, would allow reconnection to erode the
 239 magnetopause down to the planetary surface. However, at the same time Hood and

240 *Schubert [1979]* and *Suess and Goldstein [1979]* predicted that induction effects at
241 Mercury would cause the subsolar magnetopause to remain at or above $1.2 R_M$.

242 Mercury's 2000 km radius, iron-rich, highly electrically conducting core
243 [*Smith et al., 2012*] gives rise an interaction that sets it apart from all other planetary
244 magnetospheres. In the presence of this electrically conducting sphere, changes in
245 upstream solar wind pressure will create changes in the magnetic field normal to the
246 planetary surface. According to Faraday's law, these time-dependent changes will
247 generate currents in the conducting core, which will serve to oppose this change in
248 magnetic field and temporarily increase Mercury's magnetic moment, therefore
249 limiting how far the magnetopause will be compressed [*Hood and Schubert, 1979*;
250 *Suess and Goldstein, 1979*; *Glassmeier et al., 2007*].

251 To test these predictions and assess the roles of reconnection erosion and
252 induction effects at Mercury, *Slavin et al. [2014]* analyzed three extreme solar wind
253 dynamic pressure events using MESSENGER magnetic field and plasma
254 measurements. Two of these events were due to coronal mass ejections (CMEs) and
255 the third one was due to a high-speed stream. During these orbits, the magnetic field
256 just inside the dayside magnetopause exceeded 300 nT with inferred solar wind
257 pressures of $\sim 45\text{--}65$ nPa. This field magnitude is double the typical strength of ~ 150
258 nT just inside the magnetopause [*DiBraccio et al., 2013*; *Winslow et al., 2013*], which
259 corresponds to solar wind ram pressures of ~ 10 nPa. During these events, intense
260 reconnection was observed in the form of frequent Flux Transfer Events (FTEs) and
261 steady reconnection rates derived from the normal magnetic field component to the
262 magnetopause of 0.03 - 0.20..

263 In Figure 3, the thin dashed curve illustrates the observed sixth-root
264 relationship between solar wind dynamic pressure and magnetopause standoff
265 distance determined by *Winslow et al. [2013]*. The thick dashed line shows the
266 predicted relationship between solar wind ram pressure and magnetopause standoff
267 distance when induction effects are included. As evident in the figure, induction effect
268 models predict that the magnetopause standoff distance will only be compressed
269 below $\sim 1.2 R_M$ for solar wind pressures larger than ~ 60 nT. The points on this plot
270 indicate the magnetopause standoff distances, extrapolated to the subsolar point, for
271 the boundary crossings observed during the three extreme solar wind events. The
272 subsolar magnetopause was observed at much lower altitudes than predicted during
273 these extreme solar wind intervals [*Hood and Schubert, 1979*; *Glassmeier et al., 2007*]
274 due to reconnection, which appears to be opposing the shielding effects of the
275 induction currents. Therefore, during these days of extreme solar wind pressure,
276 Mercury's magnetopause remains close to the surface due to the strong effect of
277 dayside reconnection, which transfers magnetic flux into the magnetotail [*Slavin and*
278 *Holzer, 1979*]. This result confirms that magnetic reconnection at Mercury is very
279 intense and that both high-intensity reconnection as well as magnetosphere-core
280 coupling must be included in global models of Mercury's magnetosphere during
281 extreme solar wind pressure conditions.

282

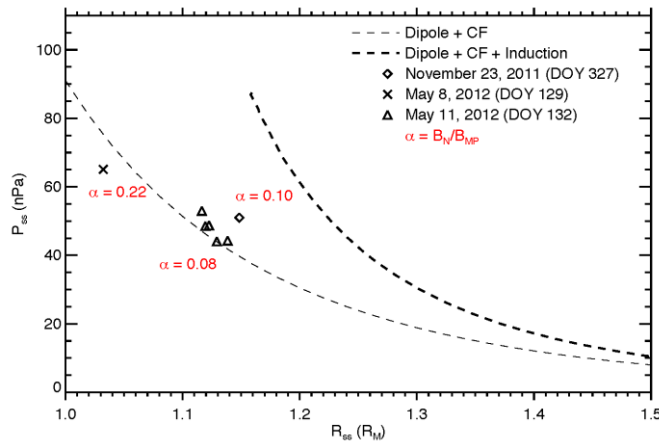


Figure 3. Solar wind ram pressure, P_{sw} , versus extrapolated magnetopause standoff distance, R_{ss} , for the magnetopause crossings of *Slavin et al.* [2014]. The magnetopause crossings on 23 November 2011, 8 May 2012, and 11 May 2012 are shown as a diamond, cross, and triangles, respectively. The dimensionless reconnection rate, α , averaged over the magnetopause crossings for each event, is also displayed for each event. The sixth-root relationship (thin dashed line) determined from a large data set of MESSENGER magnetopause encounters at typical upstream pressures of ~ 5 to 15 nPa [*Winslow et al.*, 2013] is compared with a theoretical model that includes the effects of induction in Mercury's interior [*Glassmeier et al.*, 2007] (thick dashed line). Figure from *Slavin et al.* [2014].

283

284 2.2 Dungey cycle at Mercury

285 Mercury's solar wind-driven magnetosphere experiences a circulation of
 286 plasma and magnetic flux similar to that of the Earth. This process is termed the
 287 Dungey cycle [*Dungey*, 1961; *Cowley*, 1982; see also *Seki et al.*, this volume]. The
 288 Dungey cycle begins with magnetic reconnection between the IMF and planetary
 289 magnetic field at the dayside magnetopause, resulting in open fields with one end
 290 rooted to the planet and the other in the solar wind. This open magnetic flux facilitates
 291 the exchange of solar wind and planetary plasma to and from the magnetosphere. The
 292 open fields are then carried downstream by the solar wind flow until they join the
 293 north and south lobes of the magnetotail. The oppositely directed fields of these tail
 294 lobes meet at the cross-tail current sheet where they reconnect. Tail reconnection
 295 creates two new magnetic field lines, a detached field line that rejoins the IMF and a
 296 closed field line with both ends attached to the planet. This closed field line convects
 297 sunward toward the planet, eventually moving toward the dayside and completing the
 298 cycle. Using observations from the second MESSENGER flyby of Mercury, *Slavin et al.*
 299 *et al.* [2009; 2010] determined Dungey cycle times of ~ 2 min, which is much shorter
 300 than the 1 h convection times at Earth [*Siscoe et al.*, 1975].

301 The Dungey cycle time is one of the keys for understanding the dynamical
 302 response of planetary magnetospheres to changes in the rates of magnetic
 303 reconnection at the magnetopause and in the magnetotail. It is determined by
 304 observing the rate of convection at various points in the cycle, as depicted in Figure 1.
 305 For example, the cycle time may be deduced from the time for ionospheric plasma to
 306 $\mathbf{E} \times \mathbf{B}$ drift anti-sunward across the polar cap and return at lower latitudes to its point
 307 of initiation. Alternatively, the cross-magnetospheric electric field may be inferred

308 from observations of the rate of magnetic flux being reconnected and transferred
309 to/from the magnetotail or measured directly with electric field instrumentation. At
310 Earth the time necessary for this cycle is in the range of 1–2 hr [Cowley, 1982].
311 However at Mercury, Hill *et al.* [1976] noted that the lack of an ionosphere, and the
312 expected resistive nature of the regolith, eliminates the need to take into account
313 “line-tying” or “saturation” effects [see Kivelson and Ridley, 2008] that reduce the
314 cross-magnetospheric electric field at Earth from the maximum value, $-\mathbf{V}_{\text{SW}} \times \mathbf{B}_{\text{SW}}$,
315 applied by the solar wind. Siscoe *et al.* [1975] then used scaling arguments and typical
316 solar wind and IMF parameters to estimate that the Dungey cycle at Mercury would
317 be of the order of 1 min.

318 MESSENGER’s observations taken during its second flyby on 6 October 2008
319 provided the first opportunity to more directly infer the Dungey cycle time at
320 Mercury. Slavin *et al.* [2009] used the magnetometer measurements [Anderson *et al.*,
321 2007] to determine the magnetic field normal to the magnetopause and, with
322 assumptions, calculated a cross-magnetospheric electric field of about 2 mV/m, which
323 corresponds to a Dungey cycle time of 2 min. MESSENGER’s third flyby on 29
324 September 2009 provided another opportunity to determine the Dungey cycle time
325 when a series of loading – unloading events were observed as the magnetotail was
326 traversed. At Earth magnetospheric substorms are often associated first with an
327 interval of net magnetic flux transfer to the magnetotail, termed loading, which ends
328 with the onset of magnetic reconnection in the cross-tail current layer and the
329 dissipation of the magnetic flux stored in the tail [Baker *et al.*, 1996]. The duration of
330 the tail loading and unloading intervals, sometimes referred to as the “growth” and
331 “expansion” phases of the substorm because of the accompanying auroral signatures
332 [McPherron *et al.*, 1973], are typically on the order of the Dungey cycle time. Slavin
333 *et al.* [2010] analyzed the magnetic field measurements during the third flyby and
334 found a total of four loading – unloading events. In each case the duration of the event
335 was $\sim 2 - 3$ min and in reasonable agreement with the earlier estimate based upon the
336 magnetic field normal to the magnetopause (i.e., dayside reconnection rate). We will
337 show below that analogues to many aspects of the terrestrial substorm have been
338 observed at Mercury, but on a time scale comparable to this miniature
339 magnetosphere’s Dungey cycle.

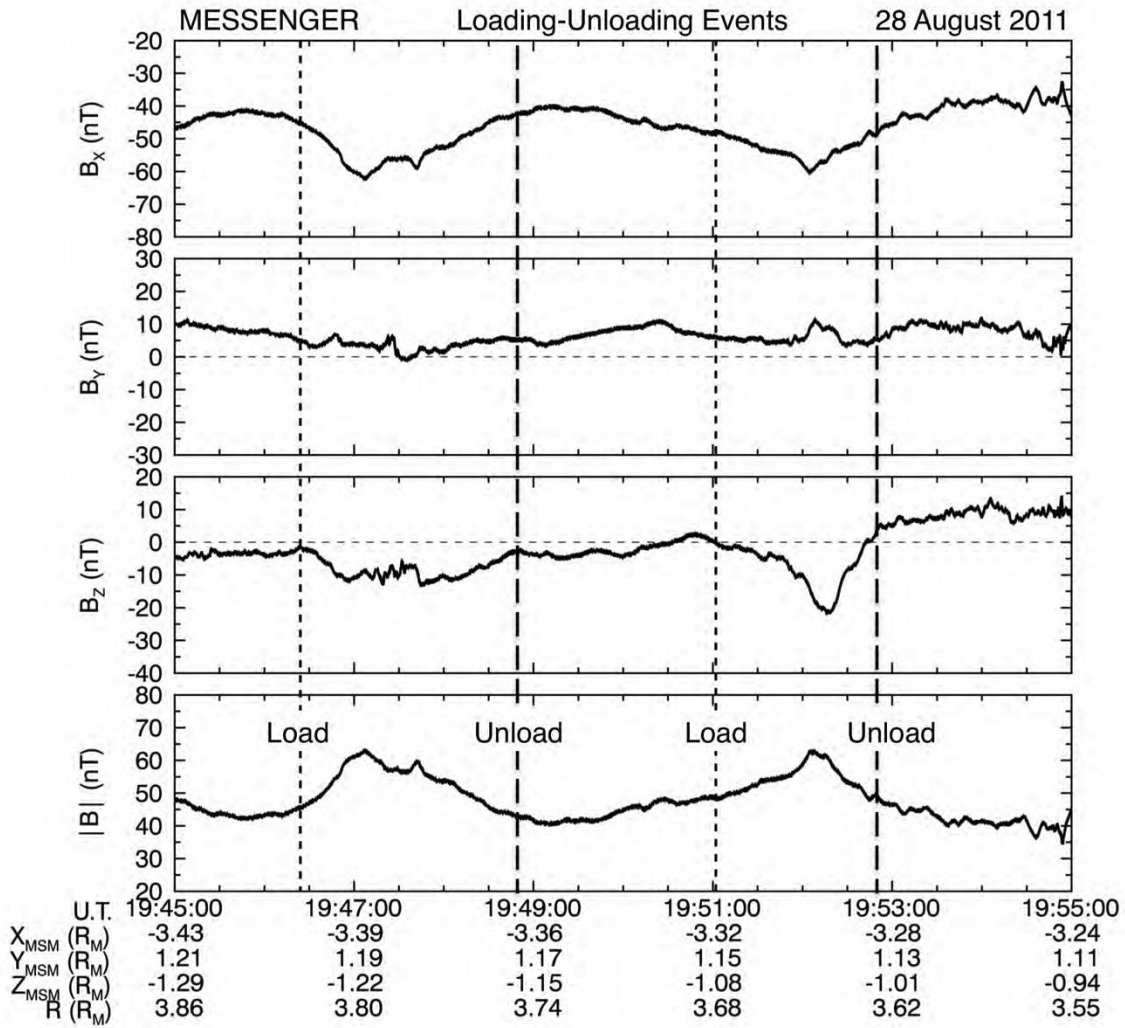


Figure 3: Substorms at Mercury – Loading/Unloading Events.

341

342

343

344

345

346

347

348

349

350

351

352

353

354

355

356

357

358

As already discussed, dayside reconnection at Earth loads the tail lobes with magnetic flux and increases the tail's overall energy levels, which are later dissipated via tail reconnection and substorms. This enhanced loading of the tail lobes with magnetic flux causes the enhanced flaring of the flank magnetopause and increases the fraction of solar wind ram pressure applied directly to the magnetotail [Caan *et al.*, 1973]. In this manner, loading of the tail with magnetic flux is reflected in the magnetic field measurements both as an increase the flaring of the magnetic field (i.e., $|B_z|$ and/or $|B_y|$) and in the total magnetic field magnitude. At Earth, the increase in the intensity of the lobe region magnetic field intensity during the substorm loading – unloading cycle is typically ~ 10 to 30% [Milan *et al.*, 2004; Huang *et al.*, 2009]. However, the fractional enhancement in the lobe magnetic field observed at Mercury during the third flyby loading events appeared much larger, perhaps even reaching 100% [Slavin *et al.*, 2010].

MESSENGER observations since orbit insertion on 18 March 2011 have provided many opportunities to observe these loading – unloading events in the magnetotail. A comprehensive analysis has yet to be carried out, but Figure 3 shows

359 two examples of this phenomenon on 28 August 2011 where, between 19:45 and
 360 19:55 UTC, two loading – unloading events are evident. MESSENGER was located
 361 in the south lobe of the tail at a distance of $\sim 3.3 R_M$ behind the planet. Each event
 362 begins with a total magnetic field intensity of ~ 40 nT directed primarily in the $-X_{MSM}$
 363 direction. The field then increases for ~ 1 min until it reaches at peak value of ~ 65 nT.
 364 This increase in total field is closely correlated with the B_Z component becoming
 365 more negative as the magnetic field flares away from the central axis of the tail. After
 366 the peak in total intensity the B_Z component becomes less negative as the intensity
 367 decreases back to its pre-substorm levels. The total increase in field magnitude during
 368 these events, $\sim 50\%$, is significantly larger than observed at Earth, but below the larger
 369 values observed during the third flyby. The duration of the events, ~ 2 min, is very
 370 close to the value determined from measurements of dayside magnetopause
 371 reconnection rate [Slavin *et al.*, 2009; DiBraccio *et al.*, 2013].

372 3 Sources

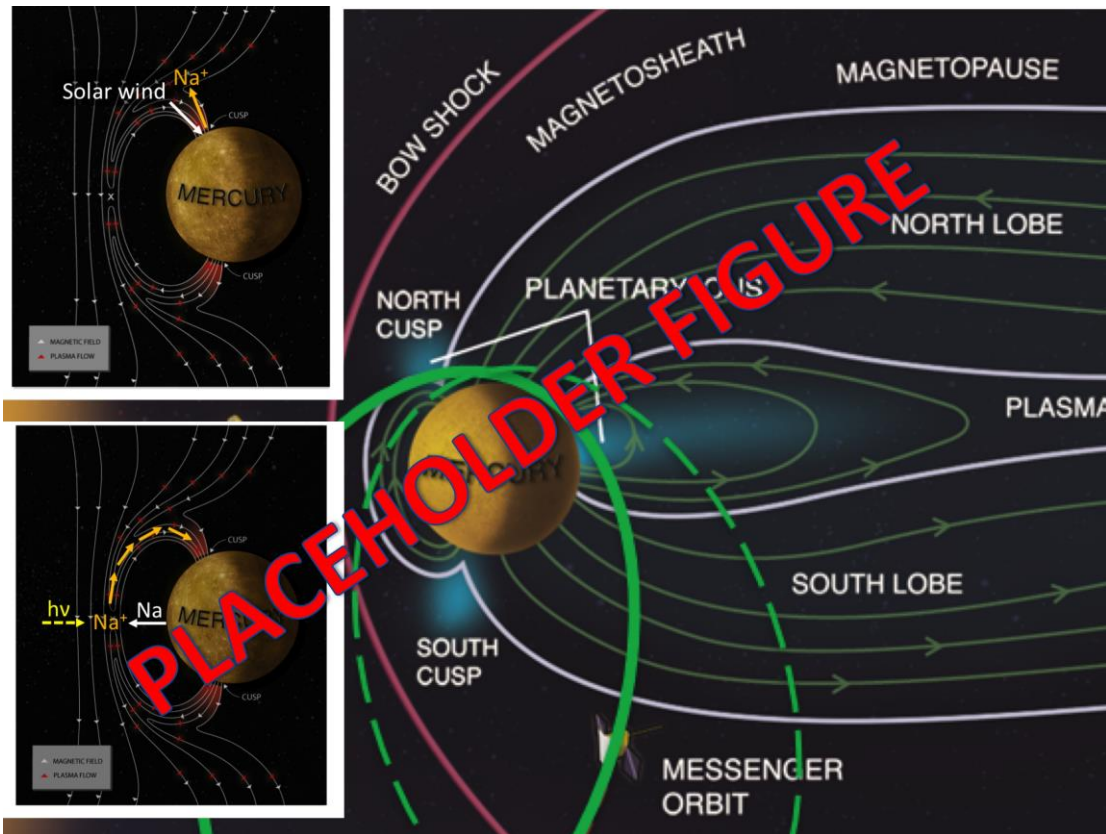


Figure AA. Plasma sources to Mercury's magnetosphere.

373 3.1 Solar wind entry

374 The solar wind is an important source of plasma to Mercury's magnetosphere.
 375 It can enter the magnetosphere mainly through five processes, studied in detail at
 376 Mercury: Magnetopause reconnection followed by entry via the plasma mantle, Flux
 377 Transfer Events (FTEs), and Kelvin-Helmholtz waves are described below. Cusp
 378 precipitation following magnetopause reconnection is described in Section 3.2.3.2.
 379 The fifth process, direct impact of the solar wind on the surface, due either to erosion

380 or compression of the dayside magnetopause, has been studied only indirectly
 381 (Section 2.1.2).
 382
 383

384 3.1.1 Magnetopause reconnection and the plasma mantle

385 Magnetopause magnetic reconnection is the dominant process for the transfer
 386 of mass, momentum, and energy between the solar wind and Mercury's
 387 magnetosphere. The resulting field topology exhibits a magnetic field component that
 388 is normal to the magnetopause, B_N . This was first observed at Mercury's
 389 magnetopause, indicating that magnetic reconnection had occurred, during the second
 390 MESSENGER flyby of Mercury on 6 October 2008 [Slavin *et al.*, 2009]. During this
 391 period, the IMF was oriented southward, a configuration that is conducive to
 392 reconnection. Using a minimum variance analysis (MVA), Slavin *et al.* [2009]
 393 determined a significant, non-zero B_N , ~13 nT, at the outbound magnetopause
 394 crossing, indicating that the boundary was a rotational discontinuity. The
 395 dimensionless reconnection rate, α , is determined by:

396
$$\alpha = \frac{B_N}{B_{MP}}$$

397 where B_{MP} is the magnitude of the field just inside the magnetopause. During this
 398 second flyby, Slavin *et al.* [2009] calculated a reconnection rate of $\alpha = 0.13$.

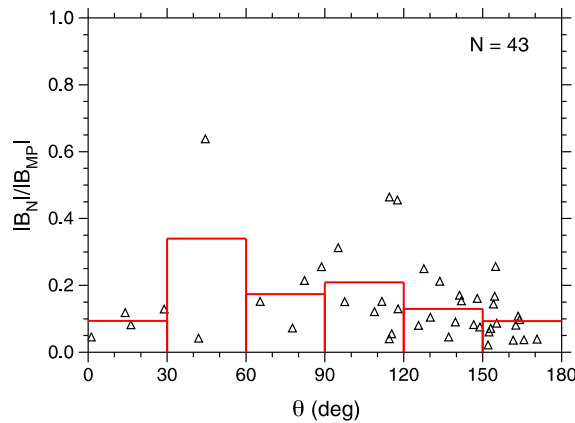


Figure 4. Magnetopause shear angle θ compared with the rate of reconnection for the magnetopause crossings. The average reconnection rate was calculated in 30° bins, as indicated by the red rectangles. Little correlation between the two quantities is evident, indicating that the reconnection occurs at Mercury for a large range of shear angles

399 In a statistical survey of magnetopause reconnection at Mercury, DiBraccio *et*
 400 *al.* [2013] identified 43 events with well-determined boundary normal vectors. The
 401 average B_N was ~20 nT, an order of magnitude larger than typical measurements at
 402 Earth. Additionally, the mean rate of reconnection resulting from this study was $\alpha =$
 403 0.15 ± 0.02 , which is about a factor of three larger than the most extensive studies at
 404 Earth. However, more importantly, this study revealed that reconnection occurs at
 405 Mercury's magnetopause independent of the magnetic shear angle θ , the angle

406 between the planetary field and the IMF (Figure 4). In fact, *DiBraccio et al.* [2013]
407 identified several reconnection events with $\theta < 30^\circ$, including one event where $\theta \sim 1^\circ$.
408 Upon further inspection, the low-shear reconnection at Mercury appears to be a
409 product of the low plasma β and decreased Alfvénic Mach number (M_A) of the solar
410 wind in the inner heliosphere, as predicted by *Slavin and Holzer* [1979]. The
411 frequency of strong PDLs [*Gershman et al.*, 2013] to also appears enhance the
412 occurrence of reconnection for all IMF shear angles at Mercury [*Slavin et al.*, 2014].

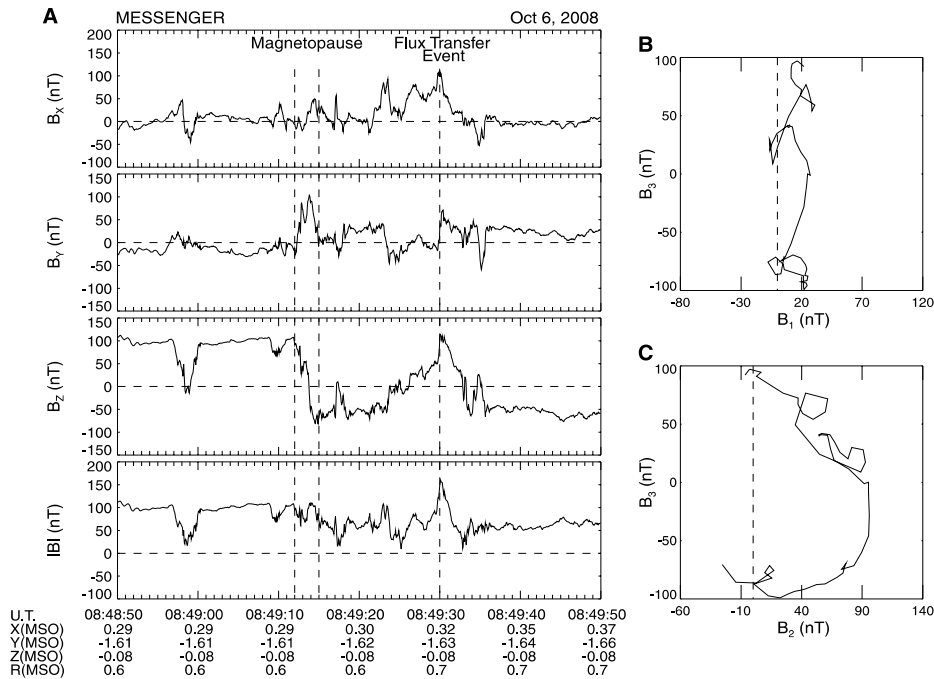
413 Using MESSENGER FIPS and MAG data, *DiBraccio et al.* [in prep]
414 presented the first observations of Mercury’s plasma mantle, a main source for solar
415 wind entry into the planet’s magnetosphere, located in the high-latitude magnetotail.
416 The plasma mantle is created as reconnected fields, populated with solar wind plasma,
417 convects downstream of the planet and rejoin the magnetosphere as part of the
418 Dungey cycle. The analysis of two successive orbits on 10 November 2012, revealed
419 a dense population of solar wind protons present just inside the high-latitude tail
420 magnetopause [*DiBraccio et al.*, in prep]. These two events, with durations of 16 and
421 21 min, exhibited clear dispersions in the proton energy distributions observed by
422 FIPS. This dispersion indicated that low-energy protons were transported much
423 deeper into the magnetosphere than the higher energy particles, which escape to large
424 downtail distances before they can $\mathbf{E} \times \mathbf{B}$ drift deeper toward the plasma sheet, where
425 \mathbf{E} and \mathbf{B} is the cross-tail electric field and magnetic field magnitude, respectively.
426 Frequent FTEs observed throughout the magnetosheath, cusp, and into the
427 magnetotail during these orbits are supportive of the high reconnection rates measured
428 at Mercury and suggest that intense dayside reconnection is responsible for
429 transporting solar wind plasma into Mercury’s magnetosphere just as at Earth.
430 Observations of Mercury’s plasma mantle have provided direct evidence of one
431 mechanism responsible for transporting solar wind plasma into the magnetosphere,
432 which has consequences for surface space weathering especially through nightside
433 plasma precipitation.

434 3.1.2 Flux Transfer Events

435 Reconnection is also observed at Mercury’s magnetopause in the form of
436 FTEs [*Slavin et al.*, 2008, 2009, 2010, 2012b; *Imber et al.*, 2014]. FTEs are created as
437 reconnection occurs between the IMF and planetary magnetic field at multiple
438 dayside X-lines. They are identified by their flux rope topology: a strong, axial-
439 aligned core field with helical outer wraps increasing in pitch angle with radial
440 distance from the center. In magnetic field data, the helical wraps are typically
441 indicated by a bipolar signature, which also provides information about the direction
442 that the flux rope is traveling. The core field is designated by a local field
443 enhancement that is coincident with the inflection point of the bipolar signature. Flux
444 ropes may also be remotely observed if the spacecraft does not directly pass through
445 the FTE, but rather, encounters the draped and compressed fields surrounding the flux
446 rope. These perturbations, called traveling compression regions (TCRs), are used to
447 infer the dimensions of a flux rope.

448 During the first MESSENGER flyby of Mercury, *Slavin et al.* [2008]
449 identified a ~ 4 -s-duration FTE in the magnetosheath using magnetic field data
450 implying a size of ~ 1200 km, or $0.5 R_M$. The bipolar signature is evident in the B_Y
451 component with an enhancement in both B_X and B_Z . During the second MESSENGER
452 flyby, *Slavin et al.* [2009] reported a FTE with a core field strength of 160 nT and a
453 duration of ~ 3 s (Figure 5). The size of this flux rope was estimated to be ~ 900 km, or

454 0.4 R_M . After a more extensive review of the MESSENGER flybys, *Slavin et al.*
 455 [2010] reported on six FTEs encountered during the first and second Mercury flybys.
 456 The durations of these events ranged from 1–6 s and a flux rope modeling technique
 457 [Lepping *et al.*, 1990, 1995, 1996] was implemented and determined the FTE
 458 diameters to range from 0.15–1.04 R_M . Additionally, the model results indicated that
 459 the magnetic flux content of these structures ranges from 0.001–0.2 MWb, or about
 460 5% of the 4–6 MWb tail lobe flux [Slavin *et al.*, 2010]. Additionally, the largest of
 461 these events may contribute up to ~30 kV to the cross-magnetospheric electric
 462 potential.
 463



464 **Figure 5. (A) Magnetic field observations of the inner current sheet and MP boundary observed**
 465 **as MESSENGER exited the dawn-side magnetosphere. (B) Magnetic field measurements across**
 466 **the MP graphed in the plane of maximum and minimum variance. (C) Magnetic field**
 467 **measurements across the MP graphed in the plane of maximum and intermediate variance**
 468 *Adapted from Slavin et al., 2009.*

469 At Mercury’s magnetopause, flux ropes have been identified to occur as “FTE
 470 showers” [Slavin *et al.*, 2012b]. During a MESSENGER noon-midnight orbit on 11
 471 April 2011, a combination of 163 FTEs and TCRs were observed over a 25 min
 472 interval as the spacecraft traversed the southern tail magnetopause (Figure 6). During
 473 this orbit, the IMF was predominantly oriented northward. The average duration of
 474 the FTEs and TCRs was 1.7 s and 3.2 s, respectively, and all events were separated by
 475 periods of ~8–10 s. By implementing the flux rope modeling technique of *Hidalgo et*
 476 *al.* [2002a, 2002b], the mean semimajor axis of the flux ropes was determined to be
 477 0.15 R_M .

478 Most recently, *Imber et al.* [2014] performed a statistical study on FTEs
 479 observed in Mercury’s subsolar magnetosheath. In this study, 58 large-amplitude
 480 FTEs, with core fields larger than the magnitude of the planetary field just inside the
 481 magnetopause, were selected. The average durations of these events were 2.5 s. MVA
 482 was used to determine their orientation and the force-free flux rope model of *Lepping*
 483 *et al.* [1990, 1995, 1996] was applied to estimate an average flux content of 0.06
 484 MWb. *Imber et al.* [2014] concluded that unlike Earth, where FTEs contribute to <

485 2% of substorm flux transport, at least 30% of the flux transport required to drive
 486 Mercury's 2–3 min substorms is contributed by FTEs.
 487

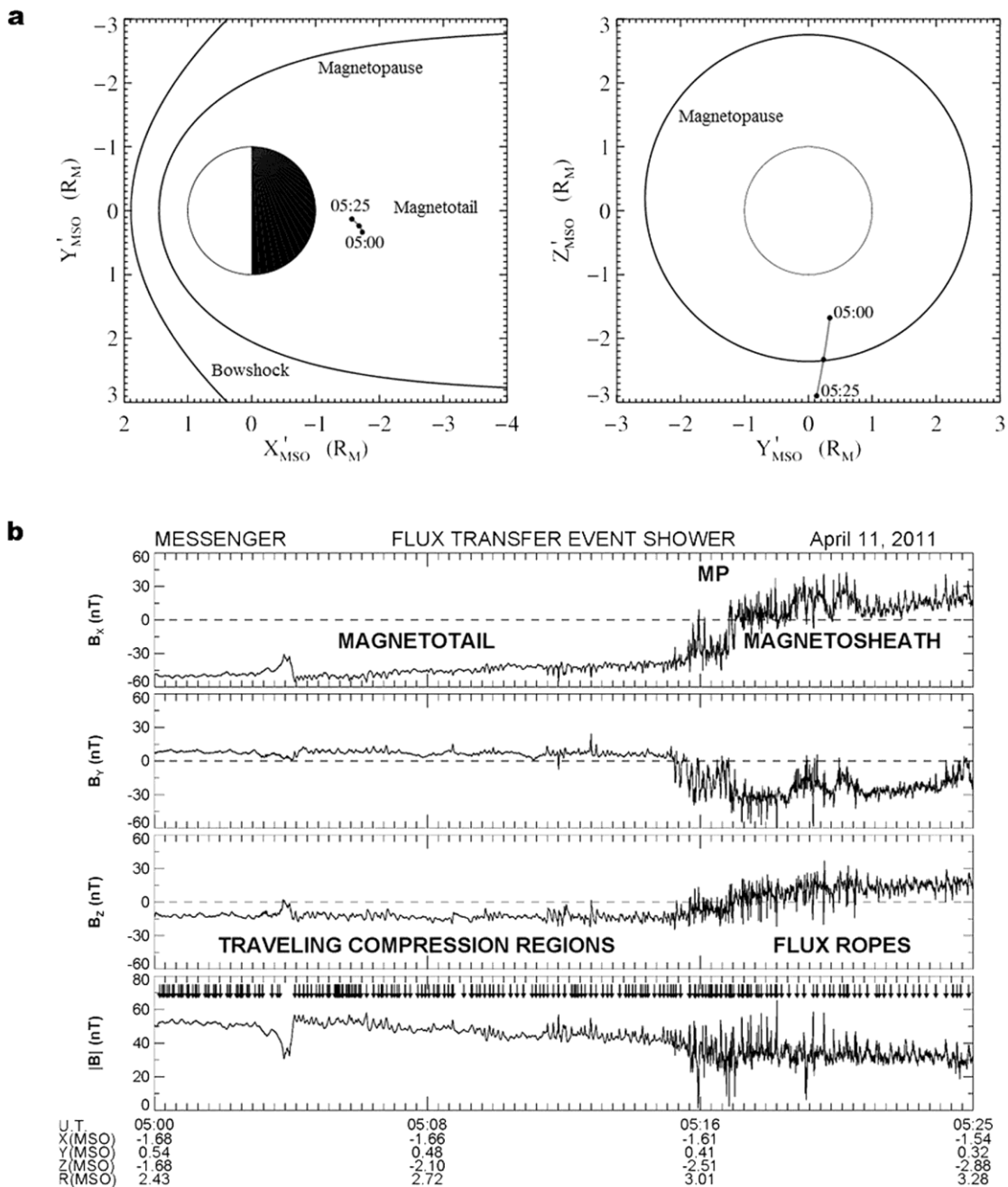


Figure 6. MESSENGER trajectory from 05:00 to 05:25 UTC on 11 April 2011, projected on to the aberrated MSO X-Y and Y-Z planes. Note that the bow shock and magnetopause surfaces are shifted northward by $0.20 R_M$ to match the northward offset in Mercury's internal magnetic dipole. (b) Magnetic field measurements taken during this interval span the outer portion of the southern lobe of Mercury's magnetotail, the magnetopause, and the nearby magnetosheath. Vertical arrows in the fourth panel mark 97 TCRs inside the magnetotail and 66 FTE-type flux ropes in the adjacent magnetosheath. *Adapted from Slavin et al., [2012b].*

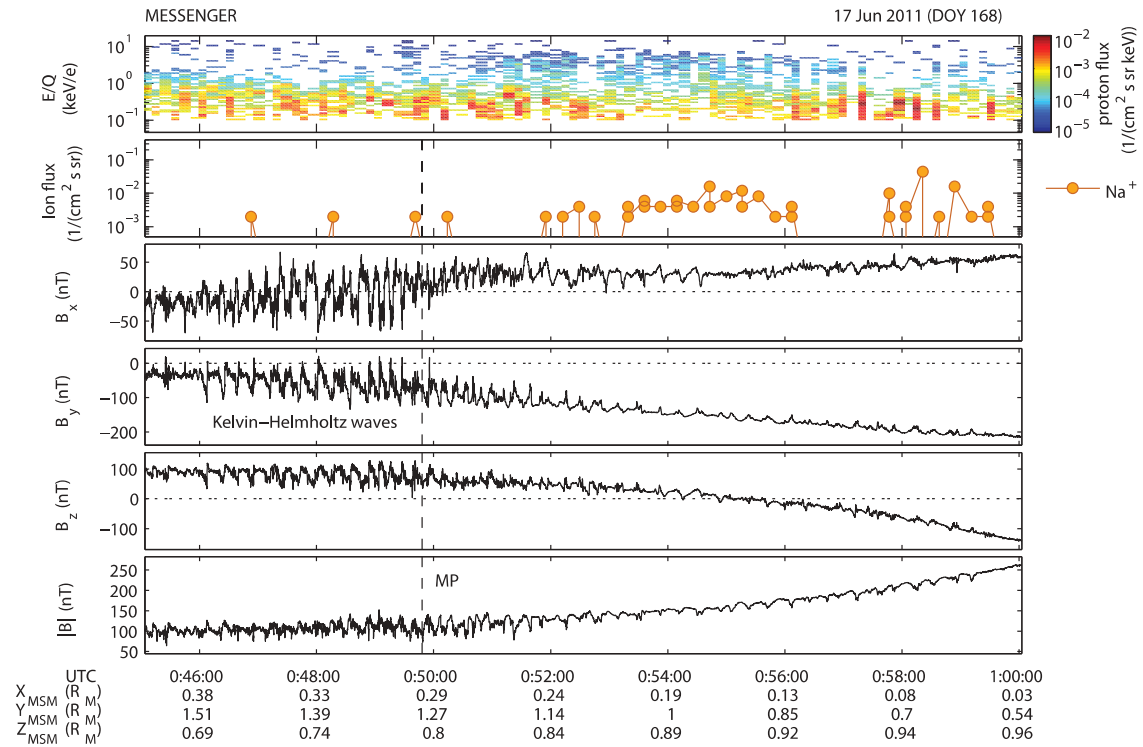
488
 489

490 3.1.3 Kelvin-Helmholtz waves

491 Kelvin-Helmholtz (KH) instabilities are another well-known mechanism
492 responsible for the transfer of mass, momentum, and energy from the solar wind into
493 planetary magnetospheres. In situ observations of KH waves at a planetary
494 magnetopause can be identified as surface waves creating a series of periodic
495 magnetopause crossings. Indeed, the growth rate of KH waves relies on the velocity
496 shear and finite Larmor radius effects. During the first MESSENGER flyby of
497 Mercury, *Slavin et al.* [2008, 2009] reported possible KH wave activity after
498 identifying three rotations along the dusk magnetopause while the IMF had a
499 northward orientation. The durations of these field rotations were $\sim 5\text{--}25$ s, implying
500 spatial scales of $\sim 0.2\text{--}2 R_M$. *Sundberg et al.* [2010] studied these events in further
501 detail and concluded that the observed waves were not due to KH instabilities but
502 might possibly indicate an initial perturbation leading to KH vortices further down the
503 tail.

504 During the third MESSENGER flyby, *Boardsen et al.* [2010] identified
505 magnetic field variations indicated by 15 dusk-side magnetopause crossings over a
506 short 2-minute interval, likely suggesting the presence of KH instabilities.
507 Additionally, a distinct sawtooth pattern present in B_Y and, to a lesser extent, B_X ,
508 supports the conclusion of highly steepened KH wave activity. *Sundberg et al.* [2011]
509 revisited these observations and performed a reconstruction of the KH vortex, with
510 the assumption that the wave pattern is quasi-stationary. This analysis concludes that
511 the spatial reconstruction of a vortex pattern is in agreement with the field rotations
512 located at the dusk-side magnetopause during the third MESSENGER flyby.

513 To understand the general characteristics of KH waves at Mercury's
514 magnetopause, *Sundberg et al.* [2012] performed a survey of six KH wave trains by
515 identifying the events based on sawtooth wave patterns (Figure 7) and periodic
516 magnetopause crossings in magnetic field data. The results provide clear evidence
517 that KH waves are frequently observed at Mercury's dusk-side magnetopause with
518 wave periods ranging from 10–40 s and large-amplitude oscillations ranging from 70–
519 150 nT.



520 **Figure 7. KH observations on 17 June 2011. The first and second panels show the FIPS**
 521 **spectrogram of E/Q for the measured proton flux and the sodium ion count rate, respectively.**
 522 **The third–fifth panels are the magnetic field components and the sixth panel is magnetic field**
 523 **strength. Adapted from Sundberg et al. [2012].**

524 *Gershman et al. [2015]* showed that KH waves observed on Mercury’s dusk-
 525 side (~18–21 h local time) magnetopause can be affected by the presence of heavy
 526 planetary ions. On the dusk-side, where Na^+ -group ions (m/q 21–30) can dominate
 527 the pressure, KH waves appear at the Na^+ ion gyrofrequency. This kinetic-scale
 528 behavior is due to the large gyroradii of these planetary ions. This is contrasted with
 529 the fluid-scale behavior of other KH waves observed at Mercury, especially on the
 530 dayside region around the dusk terminator (12–18 h local time). This work constitutes
 531 the best evidence to date that Na^+ -group ions can be dynamically important in the
 532 magnetosphere, an open question since the discovery of the Na-dominated exosphere
 533 at Mercury.

534 3.2 Planetary ions

535 Planetary ions are formed at Mercury, either by ionization from exospheric
 536 neutral atoms or from processes that act directly on the surface. As a result, both the
 537 surface and the exosphere are significant plasma sources to Mercury’s
 538 magnetosphere.

539 3.2.1 Surface processes

540 Exogenic processes acting on the surface causing particle release permanently
 541 populate Mercury’s exosphere, the thin, collision-free, gaseous envelope around the
 542 planet. Ionization of these exospheric particles contributes significantly to the
 543 magnetospheric population of ions. Four processes have long been considered for
 544 particle release at Mercury: thermal desorption (TD), photon-stimulated desorption

545 (PSD), micro-meteoritic impact vaporisation (MIV), and ion-induced particle
546 sputtering (IS). These particle release processes have been reviewed several times
547 [e.g., *Wurz and Lammer, 2003; Killen et al., 2007* and General Processes chapter of
548 this volume] and have been extensively studied for Mercury [e.g., *Mura et al., 2009;*
549 *Wurz et al., 2010*].

550 The intense solar irradiation of the surface is responsible for TD and PSD, i.e.,
551 these processes are confined to the dayside of Mercury. TD is restricted to volatile
552 species, i.e., species that have an appreciable sublimation rate at the surface
553 temperatures of Mercury, 100–700K. These volatiles (H₂, N₂, O₂, H₂O, CO₂, He, Ne,
554 Ar and molecular fragments thereof) are expected to constitute the major part of
555 Mercury's dayside exosphere, but only He has been detected so far. Contributions by
556 the other three processes are orders of magnitude lower [*Wurz and Lammer, 2003;*
557 *Wurz et al., 2010*]. Since the evaporation rates for the dayside temperatures are large,
558 volatile species falling onto the surface will be re-emitted almost immediately into the
559 exosphere and will be thermally accommodated with the surface temperature. Only at
560 the night side some volatiles can condense and are thus removed from the exosphere.
561 Thus, a day-night modulation in exospheric density of some volatiles is expected, as
562 was observed for argon in the lunar exosphere [*Stern, 1999*]. Since TD-released
563 particles have thermal energies, they all fall back onto the surface and escape (Jeans
564 escape) is negligible. The contribution to the magnetosphere is via photoionization of
565 exospheric gas. Since the scale heights of thermal particles are low, and thus the
566 ballistic travel times are low, the flux of photoions from thermal species is moderate.

567 PSD, also driven by solar irradiation, is even more restricted than TD for
568 species it can release from the surface: at Mercury only Na and K are released by this
569 process. However, appreciable PSD yields of Na and K are only observed if the alkali
570 metal is freed from the mineral bound in the crystal and is available as adsorbed atom
571 on the surface [*Yakshinskiy and Madey, 1999, 2004*]. Impacting energetic plasma ions
572 may cause the liberation of the alkali metal from the mineral, which was used in a
573 recent 3D model to explain Na observations during Mercury transit of the Sun [*Mura*
574 *et al., 2009*]. Alternatively, a surface reservoir of Na was postulated to model the
575 exospheric Na observations during a Mercury year [*Leblanc and Johnson, 2010*]. A
576 part of these models is the consideration of the fate of alkali atoms when they fall
577 back to the surface, which is discussed as sticking probability in surface physics. The
578 sticking probability for atomic K is nearly constant over the surface temperature range
579 of 100–500 K, whereas for Na it decreases with increasing temperature in this range
580 [*Yakshinskiy and Madey, 2005*], which influences the Na/K ratio to be observed in the
581 exosphere. More recently, extensive UVVS observations of Na (K has not been
582 observed by the MESSENGER) have shown that TD is not a significant process for
583 Na [*Cassidy et al., 2015*]. It is also not seen in the other species regularly observed by
584 UVVS: Ca [*Burger et al., 2014*] and Mg. The lack of TD is surprising for Na given
585 that it is relatively volatile [*Hunten et al., 1988*] but may be explained by the
586 relatively large binding energy seen for Na adsorbed on an ion-bombarded surface
587 [*Yakshinskiy et al., 2000*].

588 MIV will take place everywhere on the surface of Mercury, on the day- and
589 nightside. MIV fluxes at Mercury have been modeled by several authors [*Cintala,*
590 *1992; Müller et al., 2002; Cremonese et al., 2005; Bruno et al., 2006; Borin et al.,*
591 *2010*]. These fluxes are usually considered omni-directional, though *Killen et al.*
592 [*2014*] showed that preferential dust bombardment on the dawn hemisphere could
593 explain the concentration of Ca exosphere there [*Burger et al., 2014*]. The impact of
594 micro-meteorites and meteorites results in the release of surface material in form of

595 gas and solid fragments [e.g., *Cintala*, 1992] where the gas fraction is a hot thermal
596 expanding cloud composed from all the material of the impact site. Most of the micro-
597 meteorites are indeed very small particles, and thus a constant flux bombards
598 Mercury's surface resulting in a constant contribution to the exosphere [*Wurz et al.*,
599 2010]. For typical solar wind conditions, MIV and IS give similar exospheric particle
600 populations [*Wurz et al.*, 2010]. However, larger projectiles may sometimes hit the
601 surface causing the exospheric density contribution from MIV to temporarily increase
602 (for about 1 hour) by up to a factor of 100 for projectiles of 0.1 m [*Mangano et al.*,
603 2007]. Nevertheless, such episodic events have not been observed for the 15+
604 Mercury years that UVVS has been regularly observing Na, Ca, and Mg.

605 IS is the process of particle release upon the impact of an energetic ion on a
606 solid surface. IS is a very well understood process because of its application in semi-
607 conductor industry [*Behrisch and Eckstein*, 2007]. IS depends on the energy of the
608 impacting ion, and the sputter yield, i.e., the number of surface atoms sputtered per
609 incoming ion, is maximal for ions with energy of 1 keV/nuc. All atoms on the surface
610 are released by IS more or less stoichiometrically causing a continuous erosion of the
611 surface. IS arises either from solar wind ions at the locations where solar wind ions
612 have access to the surface of Mercury or by magnetospheric ions, both given by the
613 topology of Mercury's magnetosphere. For typical solar wind conditions the
614 sputtering contribution to the exosphere is small [*Wurz et al.*, 2010], but for CMEs
615 with significantly higher plasma density and increased He⁺⁺ contents the ion
616 sputtering contribution may increase dramatically for the duration of the CME
617 passage, as was recently discussed for the Moon [*Farell et al.*, 2012]. Sputtered
618 particles have high kinetic energies, and a significant fraction of them can escape the
619 gravitational field of the planet [*Wurz et al.*, 2007, 2010]. Because of their large
620 exospheric scale height and the resulting long ballistic flight times, significant
621 ionization of sputtered atoms occurs, which is species dependent, providing input to
622 the ion population of Mercury's magnetosphere. In addition, about 0.1 to 10% of the
623 sputtered atoms are already ionized when sputtered from the surface [*Benninghoven*,
624 1975], thus contributing directly to the magnetospheric ion population.
625 Magnetospheric dynamics may cause some of these ions to return to the surface
626 [*Delcourt et al.*, 2003] and cause sputtering themselves, including on locations on the
627 night side surface.

628 3.2.2 Neutral observations

629 The components of Mercury's exosphere are sources of the magnetospheric
630 ion population mostly through the photoionization process. For this reason, it is
631 important to investigate the density, distribution and variability of the neutral
632 component to understand the plasma populations.

633 Generally, the observation of the exosphere can be performed by ground-
634 based telescopes in the spectroscopic regions free of Earth atmospheric lines or by in
635 situ measurements with ultraviolet-visible (UV-Vis) spectrometers and mass
636 spectrometers. Particularly in the case of Mercury, ground-based observations can
637 take advantage of both night telescopes and solar telescopes/towers and can provide
638 global imaging of the extended exosphere (disk and tail). So far, only the elements
639 Na, K, and Ca have been observed by ground based telescopes. In situ measurements,
640 instead, can provide high-resolution imaging of local density and allow the detection
641 of lower intensity signals to extend the list of observable species. In both cases the

642 exosphere brightness is calibrated using photometric models of Mercury's surface
643 [Hapke, 1981, 1984, 1986; Domingue et al., 1997].

644 Mercury's exosphere was discovered by a UV spectrometer onboard Mariner
645 10 [Broadfoot et al., 1977] that covered part of the extreme and far wavelength ranges
646 (30–167 nm). It discovered atomic H and He, and made a possible detection of O. An
647 occultation experiment on Mariner 10 also provided an upper limit of the total
648 atmospheric abundance, which was higher than the sum of detected constituents
649 [Fjelbo et al., 1976], meaning that some exospheric species remained still undetected.
650 About a decade later, ground-based observations discovered Na, identified via the D1
651 and D2 emission lines (near 589 nm wavelength), which are caused by resonant
652 scattering of sunlight [Potter and Morgan, 1985]. Later, also K and Ca have been
653 detected by ground-based observations [Potter and Morgan, 1986, 1997; Bida et al.,
654 2000] and an upper limit for Al, Fe and Si was defined [Doressoundiram et al., 2009].
655 MESSENGER UVVS discovered Mg and Ca⁺, and in its orbital phase regularly
656 observed Na, Ca, Mg, and occasionally H. Its wavelength range (115 nm – 600 nm)
657 precluded observations of He and K.

658 The Broadfoot et al. [1976] Mariner 10 detection of atomic oxygen was 'very
659 tentative', and it was not replicated by MESSENGER UVVS, which could have
660 easily seen the claimed ~60 Rayleigh emission [Vervack et al., 2011]. Wurz et al.
661 [2010] predicted that ion sputtering and impact vaporization should produce large
662 atomic oxygen column density (comparable in magnitude to the observed sodium),
663 but it would be difficult to detect with UVVS given the poor efficiency with which
664 atomic oxygen scatters sunlight [Killen et al., 2009]. This hypothesized oxygen
665 exosphere is a likely source for the abundant oxygen ions detected by FIPS
666 [Zurbuchen et al., 2011; Raines et al., 2013].

667 Neutral observation of Na revealed, since their first detection, very distinctive
668 features, such as recurrent peaks at mid latitudes [e.g., Potter et al., 1999] and a
669 significant neutral tail in the anti-sunward direction [Potter et al., 2002; Schmidt et
670 al., 2012; Kameda et al., 2009]. Moreover, the variability of these features has been

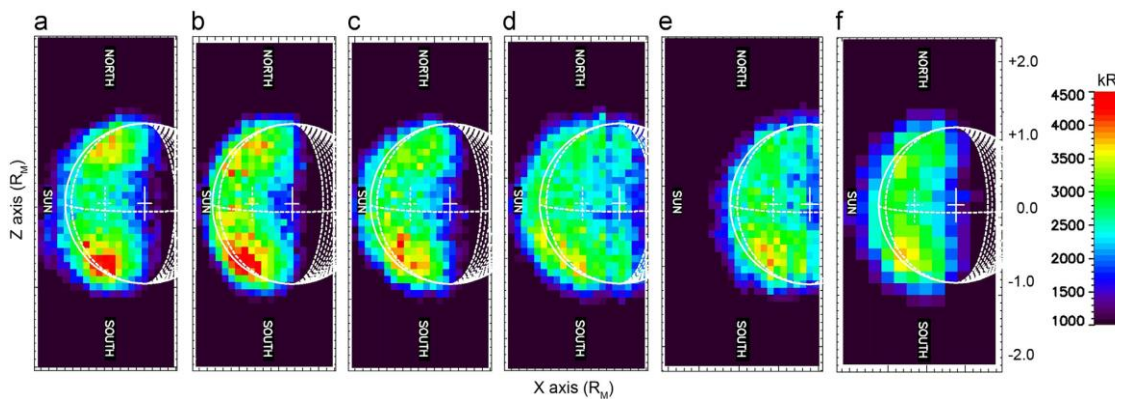


Figure 8. Time sequence of scans of Na emission intensity (in kiloRayleigh) obtained in July 13th 2008 from 7 to 17 UT. The X–Z plane is the projection plane, with the Z-axis pointing northward; the Y-axis is along the direction Earth–Mercury (with the center being the sub-Earth point). The Sun is on the left. The solid white line denotes the disk of the planet and the cross indicating the center of the disk; in white dashed the region of the disk not illuminated by the Sun, the sub-solar meridian, and the cross indicating the point of highest emission brightness due to solar reflection of the surface [Mangano et al., 2013].

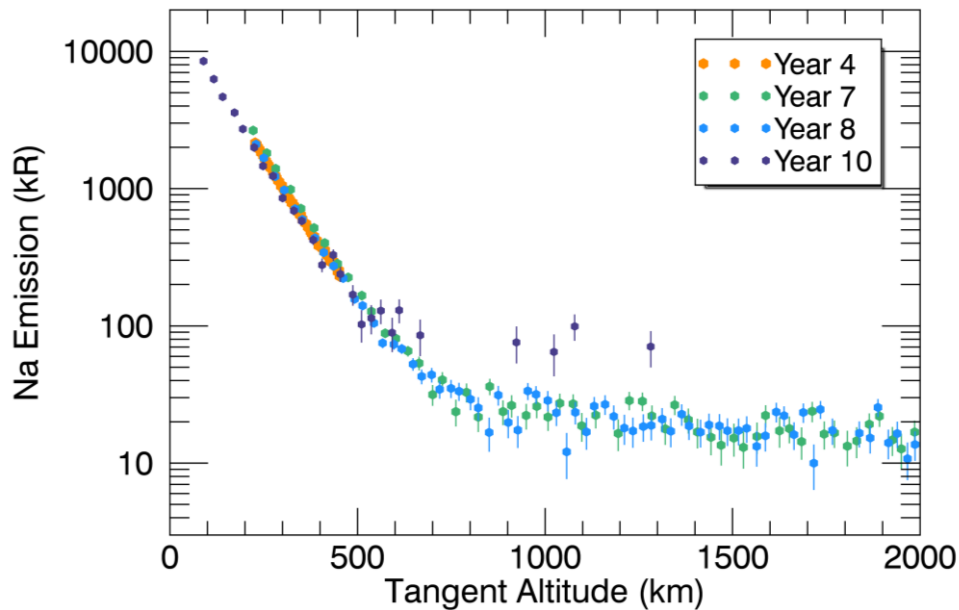
671 seen in almost three decades of Earth-based observations [Sprague et al., 1997; Potter
672 et al., 2006; Leblanc et al., 2009]. The average intensity and tail length modulate

673 along the Mercury orbit in relation to the solar radiation pressure, which maximizes
674 together with the velocity radial component [Leblanc *et al.*, 2008]. Kameda *et al.*
675 [2009] related the average intensity modulation to the crossing of the interplanetary
676 dust disk. The seasonal variation has been confirmed by MESSENGER UVVS
677 [Cassidy *et al.*, 2015]. Most of the sodium exosphere is confined to low altitudes on
678 the dayside; the scale height is only ~100 km at low latitudes [Cassidy *et al.*, 2015].
679 This means that most of the ion source is deep within the magnetosphere, which has
680 consequences for sodium ion kinetics [Raines *et al.*, 2013, 2014; Gershman *et al.*,
681 2014].

682 The improved spectral and temporal resolution of ground based observations
683 allowed investigation of speed distributions [Leblanc *et al.*, 2009] and detection of
684 even more detailed features of the Na exosphere, which now range from time-scales
685 of days to hours. Daily variations are often due to changes in the position of Mercury
686 around its orbit and to solar events [Killen *et al.*, 2001; Potter *et al.*, 2007]. Hourly
687 variations are attributed to normal solar wind fluctuations (mostly density and speed)
688 and to rapidly changing IMF coupling with the planetary magnetic field [Mangano *et al.*
689 *et al.*, 2013]. Figure 8 shows an example of hourly variations of high latitude peaks in
690 exospheric Na emission when observed from Earth. Similar double peaks at mid
691 latitudes have been reported for the K exospheric distribution [Potter and Morgan,
692 1986]. This may indicate that both of these volatile species are linked to the solar
693 wind impact onto the Mercury dayside surface below the cusps, even if it cannot be
694 generated by direct ion sputtering [Mura *et al.*, 2009]. Observations of Ca [Burger *et al.*
695 *et al.*, 2014] and UVVS observations of Na [Cassidy *et al.*, 2015], instead, show
696 different behavior apparently not related to solar wind impact but probably to MIV
697 processes acting more efficiently in certain regions of the orbit due to higher MIV
698 fluxes [Killen and Hahn, 2015]. In contrast to the rapid variability of the ground-
699 based observations, UVVS observations of Na and Ca show little episodic variability
700 as described below.

701 MESSENGER UVVS observations are quite different from, and
702 complementary to, ground-based observations. UVVS provided unprecedented
703 temporal coverage, observing the exosphere almost daily for over 16 Mercury years.
704 It also provided unprecedented spatial resolution: altitude profiles of exospheric
705 emission resolve details down to the km scale (Figure 9). UVVS had the advantage of
706 *not* observing through Earth's atmosphere, but it had limitations, too. It was not an
707 imaging spectrometer, and its field of view (FOV) and observation geometries were
708 restricted by the many considerations of spacecraft operations in a challenging
709 environment. It also had a relatively poor spectral resolution compared to the ground-
710 based observations (~0.5 nm).

711



712
 713 Figure 9. Altitude profiles of sodium emission observed above Mercury’s subsolar
 714 point by the MESSENGER MASCS UVVS instrument. These were taken over
 715 several Mercury years (as indicated by the legend), but all were taken near the same
 716 true anomaly angle, between 65°-70° in this example. Although the sodium exosphere
 717 varies temporally, this figure highlights the seasonal repeatability of MASCS
 718 observations.

719
 720 Some of the UVVS results are surprising in light of the decades of work
 721 published on Mercury’s exosphere. In particular, ground observations (e.g. *Mangano*
 722 *et al.*, 2013, above) and models show a Na exosphere that is highly variable on the
 723 time scale of hours. These sudden changes are thought to be in response to changing
 724 solar wind and IMF conditions. UVVS observations do not show this. The species
 725 that were regularly observed (sodium, calcium, magnesium) look quite similar from
 726 one Mercury year to the next, at least wherever consistent observing geometries were
 727 used over long periods of time [*Burger et al.*, 2014; *Cassidy et al.*, 2015]. On the
 728 other hand, operational constraints have severely limited UVVS observations in the
 729 cusp, the most variable region. This may explain the differences, at least in part.
 730 Much of the UVVS data remains to be analyzed, so more progress on the variability
 731 of these exospheric species can be expected.

732 3.2.3 Plasma observations

733 3.2.3.1 Overall planetary ion composition and distribution

734 Plasma observations at Mercury began with the electron observations of
 735 Mariner 10 through three flybys in 1974–1975. Measurements from the first flyby
 736 convincingly showed Mercury to have an Earth-like interaction with the solar wind:
 737 There was a well-developed bow shock and a dense, hot plasma magnetosheath,
 738 surrounding a small magnetosphere [*Ogilvie et al.*, 1974]. Magnetometer
 739 measurements were compared with the plasma electron measurements and
 740 corroborated this interpretation [*Ness et al.*, 1974]. Within the magnetosphere,
 741 electrons were detected over the full energy range of the instrument, 13.4 – 687 eV,
 742 with a significant population in 200 – 680 eV range. These measurements were later

743 interpreted as being from a hot plasma sheet [Ogilvie *et al.*, 1977]. Several energetic
744 electron bursts were detected by the energetic particle instrument [Simpson *et al.*,
745 1974; see also discussion in Wurz and Blomberg, 2001], though they were later re-
746 interpreted as being due to > 36 keV electrons [Armstrong *et al.*, 1975; Christon *et al.*
747 *et al.*, 1987]. Siscoe *et al.* [1975], Baker *et al.* [1986] and Christon *et al.* [1987]
748 attributed these energetic bursts to substorms at Mercury. Fluxes and spectral shape of
749 plasma electrons were observed to be partially correlated with these energetic bursts.
750 A hardware failure in the plasma ion instrument prevented any ion observations by
751 Mariner 10 [Ogilvie *et al.*, 1977]. Measurements from both flybys were combined
752 with neutral atom measurements from the ultraviolet spectrometer [Broadfoot *et al.*,
753 1974, 1976] to infer that Mercury has no ionosphere, making the magnetosphere
754 effectively bounded on the inside by the planet's surface.

755 The first plasma ion measurements at Mercury came with the first flyby of the
756 MESSENGER spacecraft on January 15, 2008. The Fast Imaging Plasma
757 Spectrometer (FIPS) [Andrews *et al.*, 2007] detected ions throughout the entire
758 Mercury space environment, confirming predictions of their presence [Zurbuchen *et al.*
759 *et al.*, 2008]. Protons and alpha particles (He^{2+}) from the solar wind were observed as
760 the spacecraft traversed the magnetosphere, with highest abundance in the
761 magnetosheath. Many heavy ions were also detected, ranging in mass per charge
762 (m/q) from 6–40 amu/e. These ions were found with highest abundance within the
763 magnetosphere, with Na^+ (or Mg^+) ions dominating the heavy ion population. As Na
764 is one of the dominant atoms in the exosphere and is easily ionized [Wurz and
765 Lammer, 2003], these ions are generally taken to be Na^+ , though the separation of Na^+
766 from Mg^+ ion has not yet been accomplished from FIPS data.

767 Once MESSENGER went into orbit around Mercury on March 18, 2011, the
768 vast increase in the amount of data also necessitated a change in approach to a more
769 automated approach of assigning counts to individual ion species that could be
770 applied to the data in a largely automatic fashion. The main effect of this change was
771 grouping of ions into ranges of m/q : O^+ group, m/q 14–20, including O^+ and any water
772 group ions (e.g., H_2O^+ , OH^+); Na^+ group, m/q 21–30, including Na^+ , Mg^+ and Si^+ .
773 Substantially improved background removal was also accomplished in this new
774 method, along with a much better estimation of signal to noise. The use of counts as
775 measurement units was also replaced with a more physically relevant unit, the
776 observed density (n_{obs}). This is the density computed from the counts measured,
777 without any correction for those unobserved due to the limited FIPS field of view
778 (FOV) on the three-axis stabilized MESSENGER spacecraft. These methods are
779 explained in more detail in Raines *et al.* [2013].

780 A more complete picture of the distribution of ions in Mercury's space
781 environment emerged from this much larger dataset. First, planetary ions were found
782 throughout this space environment, both inside and outside of the magnetosphere. For
783 the two most abundant species, Na^+ -group and O^+ -group ions, this distribution is not
784 at all uniform. These ions show a very substantial abundance enhancement in the
785 region of Mercury's northern magnetospheric cusp. Na^+ -group and O^+ -group ions are
786 also very abundant in the nightside near-equatorial region, and often near high-
787 latitude, dayside crossings of the magnetopause [Zurbuchen *et al.*, 2011]. Figure 10
788 shows this distribution, as a function of planetary latitude and local time, accumulated
789 from 25 March 2011 through 31 December 2011. The different panels are
790 accumulations over more than 500 orbits, indicating that these enhancements are very
791 likely permanent features of Mercury's magnetosphere.

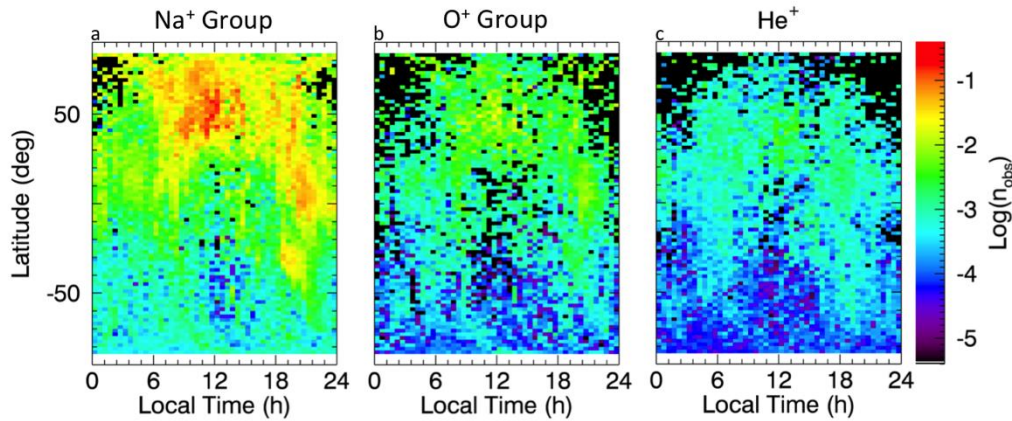


Figure 10. Na⁺-group (a), O⁺-group (b), and He⁺ (c) ion observed density as a function of local time and planetary latitude. Observed density is averaged within each 0.5 h by 2° local time - latitude bin. Unobserved regions are colored white while observed regions with zero counts are coloured black. *Updated from Zurbuchen et al. [2011].*

792

793 In contrast to Na⁺-group and O⁺-group ions, He⁺ is much more evenly
 794 distributed throughout the space environment [Zurbuchen et al., 2011; Raines et al.,
 795 2013]. This ion is present in the solar wind, but its enhanced abundance around the
 796 planet indicates that a significant fraction of its population comes from Mercury,
 797 either from the surface or exosphere. For example, He⁺ has a distinct distribution from
 798 alpha particles (He²⁺), not showing the magnetosheath enhancements very clearly
 799 observed in the doubly ionized He²⁺. Very low plasma densities in Mercury's space
 800 environment make formation of He⁺ from He²⁺ unlikely in any substantial quantities.

801 Of course, the distribution of planetary ions does not directly infer their
 802 sources. In the absence of a collisional atmosphere or ionosphere, the inner boundary
 803 of Mercury's magnetosphere is essentially the surface of the planet. Ions observed
 804 anywhere in this environment have been subject to the electromagnetic forces and
 805 processes of the magnetosphere, and their trajectories have been substantially
 806 affected. Furthermore, most of these processes are expected to be highly variable in
 807 time. One strategy employed for examining the relationship between observations and
 808 sources has been to look at the average behavior of ion distributions, hoping to find
 809 some commonality with the expected exosphere or surface sources. Raines et al.
 810 [2013] showed that the average observed density of Na⁺-group and O⁺-group ions
 811 varied substantially with true anomaly angle, the angle between Mercury and its
 812 orbital periapsis around its Keplerian orbit (Figure 2c of that work). He⁺ ions showed
 813 a much less pronounced variation. These results were compared notionally with
 814 ground observations of the same variation of the exosphere. No clear correlation was
 815 apparent. In that same work *e*-folding heights of observed density versus altitude were
 816 computed for those same three planetary ion species, around three local times (dawn,
 817 noon and dusk). These heights showed substantial differences across local time and
 818 species, with the smallest height always at noon and those of Na⁺ group ~2–6 times
 819 smaller than other ions. These ion *e*-folding heights are much larger, at least 5-10
 820 times, than calculated scale heights for species of the neutral exosphere [Wurz and
 821 Lammer, 2003; Wurz et al., 2010], likely confirming expectations that
 822 magnetospheric dynamics plays a substantial role.

823 3.2.3.2 Cusp

824 Mercury's magnetospheric cusps have long been thought to be major sources
825 of planetary ions for its magnetosphere, primarily through the process of solar wind
826 sputtering [Lammer *et al.*, 2003; Leblanc and Johnson, 2003, 2010; Massetti *et al.*,
827 2003]. As discussed above, the abundance of planetary ions is largest there
828 [Zurbuchen *et al.*, 2011; Raines *et al.*, 2013]. The cusps, however, are very active, and
829 dynamic regions at Mercury, so a more detailed analysis was required to connect
830 observed ions to cusp sources.

831 *Raines et al.* [2014] performed such a study of Mercury's Northern cusp
832 region. Focusing on Na⁺-group ions and protons, these authors selected 77 cusps with
833 significant Na⁺-group ion content from 518 orbits, spanning observations from
834 September 2011 through May 2012. They examined ion flow directions, energy-
835 resolved pitch angle, energy and spatial distributions for these two species. Their
836 main result was that Na⁺-group ions in Mercury's cusp are too high in energy (2.7
837 keV on average) to be produced locally in the cusp. They also found a regular
838 occurrence of keV-energy Na⁺-group ions flowing northward in the dayside
839 magnetosphere. From these measurements, the authors hypothesized that neutral Na
840 atoms were ionized in the vicinity of the subsolar magnetopause and accelerated into
841 the cusp by reconnection. This process may constitute a significant source of keV-
842 energy planetary ions in Mercury's magnetosphere.

843 Two other interesting results emerged from this work, both of which can be
844 more easily seen from energy-resolved pitch angle distributions. These plots (Figure
845 11), which show the flow direction of ions relative to the magnetic field, are
846 particularly interesting in the cusp because the magnetic field is largely radial there.
847 This means that ions traveling in the anti-parallel magnetic field direction are
848 effectively headed away from the surface, while those parallel ions are headed toward
849 the surface. The energy-resolved pitch angle distribution for protons (Figure 13)
850 shows a distinct depletion in flux coming up from the surface (anti-parallel, left side
851 of figure), when compared with the flux going down toward the surface (parallel,
852 right side of figure). This asymmetry likely results from the fact that a fraction of
853 protons traveling toward the surface are lost to surface precipitation, rather than being
854 reflected in the increasing magnetic field there. This loss cone appears to be >40° and
855 constitutes a strong indication that protons are impacting Mercury's surface in the
856 cusp. The opposite is observed for Na⁺-group ions (Figure 10e): At energies of 100–
857 300 eV, they are enhanced in the anti-parallel direction and therefore appear to be
858 streaming out of the cusp. This is also visible as a small bump in the anti-parallel
859 phase space density shown in the left half of Figure 10f. Taken together, these two
860 results may constitute a cause and effect observation of solar wind sputtering at
861 Mercury, though some additional explanation of Na⁺-group acceleration is required.
862 Several studies provided a more quantitative look at proton precipitation at the cusp.
863 Those are reviewed in Section 4.3.1.

864
865
866

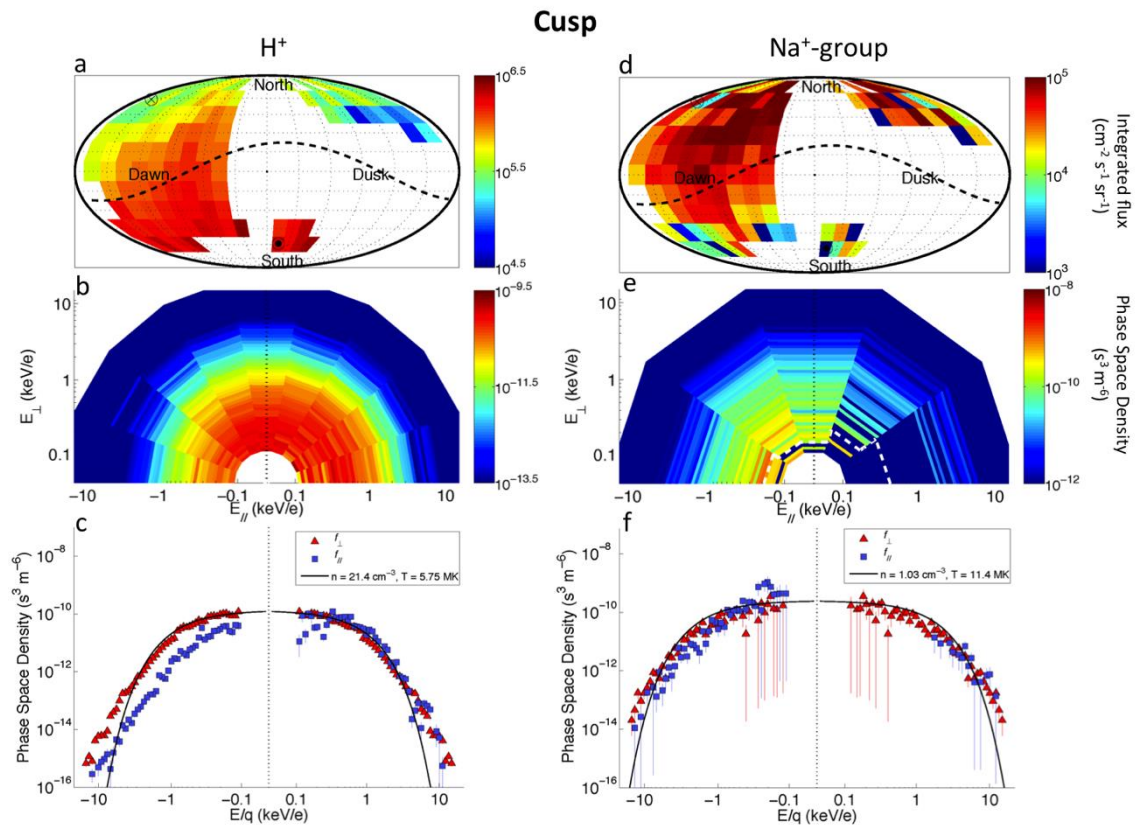


Figure 11. Kinetic properties of protons and Na⁺-group ions within the cusp, accumulated over 77 cusp crossings. Top panels (a, d) show flow direction histograms for protons and Na⁺-group ions. The middle panels (b, e) are energy-resolved pitch angle distributions, which show the flow direction and energy of ions relative to the magnetic field in 20° (protons) and 36° (Na⁺-group) bins. Slices through these distributions in the parallel, anti-parallel and perpendicular directions are shown in the bottom panels (c,f). These figures show protons which are flowing down toward the surface, as well as loss cone of >40° in width. Low energy (100-300 eV) Na⁺-group ions appear to be upwelling from the surface, while those at energies up to 10 keV have large perpendicular energy components. *Reproduced from Raines et al. [2014].*

867 3.2.3.3 Central Plasma Sheet

868 A large collection of data from the orbital phase showed that average plasma
 869 sheet densities were in line with those observed in the first flyby, though average
 870 temperatures were higher [Gershman et al., 2014]. In addition to values for protons,
 871 average density and temperature were also reported for alpha particles and Na⁺-group
 872 ions (Table 1), giving a good average picture of plasma sheet ions for consideration
 873 by other studies. The estimated pressure contribution from plasma sheet protons was
 874 found to be in good agreement with the observed magnetic depressions there [Korth et
 875 al., 2011], providing an independent validation of these recovered plasma parameters.
 876

Species	Density (cm ⁻³)	Temperature (MK)
H ⁺	7.81	9.29
He ²⁺	0.265	30.3
Na ⁺ -group	0.663	15.7

877 Table 1. Average kinetic properties in the central plasma sheet. From Gershman et al.,
 878 2014.

879 One of the most interesting results from *Gershman et al.* [2014] comes from
 880 the relative temperatures of plasma sheet ions (Figure 12). For solar wind ions, alpha
 881 particles and solar wind heavy ions (mostly O^{6+} and C^{5+}), the ratio of their
 882 temperature to that of protons is mass-proportional, i.e., $T_i/T_{H^+} = m_i$. This is expected
 883 for ions that are accelerated to the same speed, as is often the case in the solar wind
 884 and reconnection outflow. However, planetary Na^+ -group and O^+ -group ion
 885 temperatures show a roughly constant ratio to protons, as if they were accelerated
 886 through a potential. This may result from them having gyroradii which are large
 887 compared to plasma sheet magnetic field gradients, so that their motion in the plasma
 888 sheet is dominated by the cross-tail electric field. This result is consistent with
 889 findings by *Raines et al.* [2013] that Na^+ -group ions are substantially enhanced in the
 890 pre-midnight plasma sheet when compared to the post-midnight side. These may both
 891 be observational evidence of the expected non-adiabatic behavior of heavy ions at
 892 Mercury, a point to which we return in some detail below.

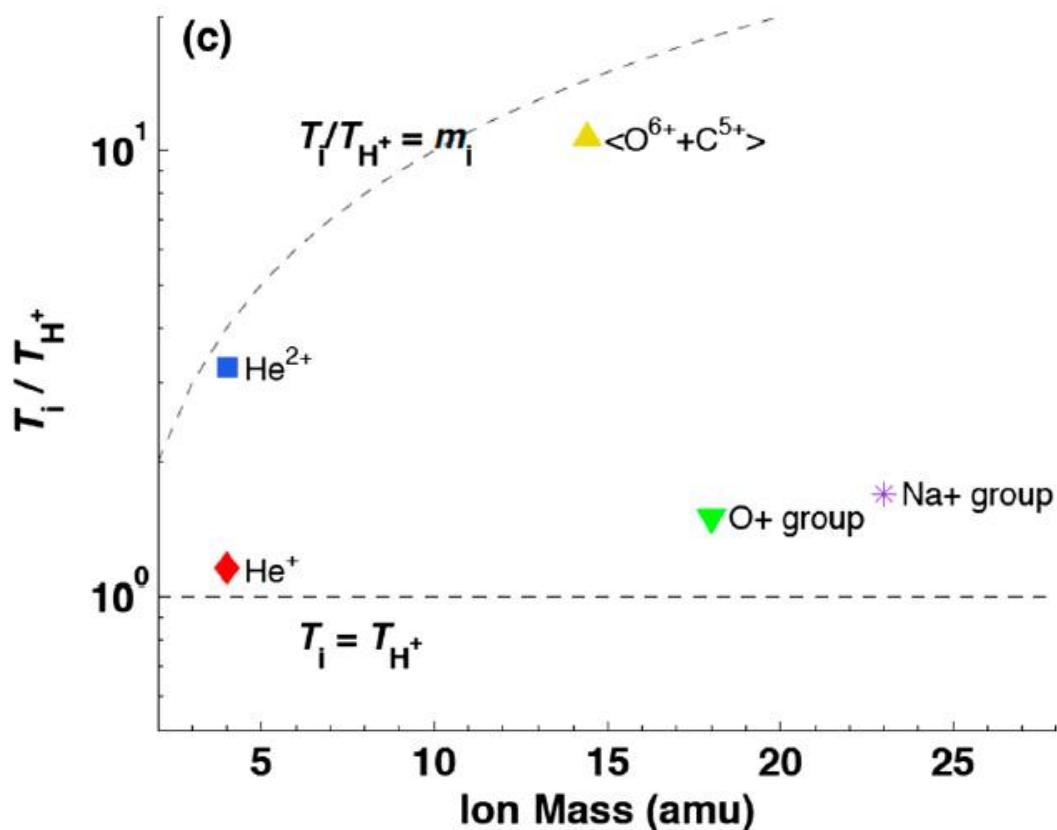


Figure 12. (a) Average temperature T_i of each species relative to that of H^+ . Dashed lines corresponding to $T_i/T_{H^+} = m_i$ are also shown.

893

894 4 Losses

895 There have been no studies of MESSENGER data focused on computing
 896 plasma loss rates from Mercury's magnetosphere. Estimating these rates from single
 897 spacecraft measurements of a highly dynamic system requires tightly coordinated and
 898 well-calibrated combination of models and data that has not yet been achieved. Work
 899 is heading in that direction, as described below in Section 5.1.2, so it is likely the

900 plasma loss rates will be derived in the near future. Studies of several magnetospheric
 901 processes that contribute to plasma loss are described below.

902 4.1 Observations of plasmoids and TCRs

903 Loading of the tail lobes and magnetopause flaring lead to thinning of the
 904 plasma sheet and its embedded cross-tail current layer for reasons that are still not
 905 well understood [Kuznetsova *et al.*, 2007; Winglee *et al.*, 2009; Raeder *et al.*, 2010].
 906 When the current sheet thins, the normal magnetic field component is sufficiently
 907 reduced such that it becomes unstable to reconnection. A fundamental aspect of the
 908 reconnection process is the formation of magnetic islands with helical or quasi-loop-
 909 like topologies in the cross-tail current layer [Hesse and Kivelson, 1998]. These
 910 magnetic structures are called “plasmoids” [Hones *et al.*, 1984]. Similar to the FTEs
 911 at the magnetopause (Section 3.1.2), the lobe magnetic field becomes draped and
 912 locally compressed about the plasmoid, which can be observed as TCRs [Slavin *et al.*,
 913 1993]. Because TCRs can be observed over a large fraction of the lobe region they are
 914 observed far more frequently than the underlying plasmoids that occupy a much
 915 smaller volume. Plasmoids and TCRs are highly correlated with the onset of
 916 magnetospheric substorms [Slavin *et al.*, 1992; Moldwin and Hughes, 1992]. Many
 917 flux rope- or magnetic loop-like plasmoids can be formed during a given reconnection
 918 event, with some being carried sunward and others tailward by the fast Alfvénic
 919 jetting of plasma away from reconnection X-lines [Slavin *et al.*, 2003]. Indeed, initial

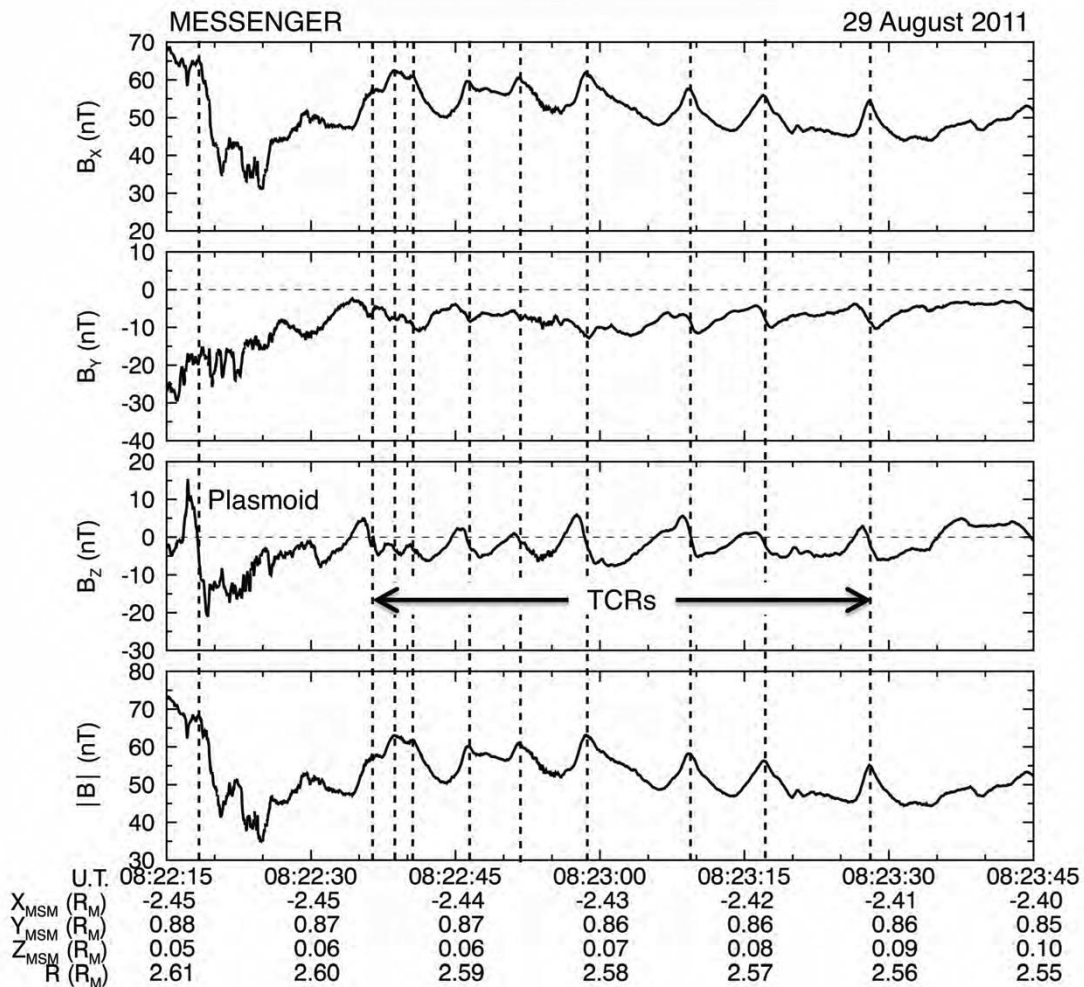


Figure 13. Quasi-periodic plasmoids and TCRs observed during the orbital phase of the MESSENGER mission are marked with vertical dashed lines.

920 analyses of the MESSENGER measurements have revealed the presence of sunward-
921 and anti-sunward-moving plasmoids and TCRs [Slavin *et al.*, 2009, 2012a].

922

923

924 Figure 13 displays a 90 sec-long interval on 29 August 2011 when
925 MESSENGER had just entered the north lobe of the magnetotail $\sim 2.4 R_M$
926 downstream of Mercury. The interval starts at 08:22:19 UTC with the spacecraft
927 encountering a plasmoid. It is identified by the ~ 1.5 sec-long, large amplitude, north-
928 then-south B_z perturbation followed by a ~ 6 sec interval of weaker magnetic field
929 with a southward orientation and higher frequency fluctuations. The plasmoid is then
930 followed by a series of 9 traveling compression regions, which are similarly
931 characterized by $\sim 1 - 2$ sec north-then-south B_z perturbations with a recovery period
932 of ~ 5 sec. However, the TCRs differ in that they are strongly correlated with 10 -
933 15% enhancements in the total magnetic field intensity. The absence of higher
934 frequency fluctuations and the steady sunward orientation of the magnetic field
935 indicate that all of these events take place in the northern lobe of the tail.

936 These observations are remarkably similar to the plasmoid and TCR events
937 observed during the second flyby [Slavin *et al.*, 2009]. MESSENGER does not have
938 the capability to measure the plasma flow during these events, but the mean ejection
939 speed for plasmoids in the Earth's near-tail is $\sim 500 - 600$ km/s [Ieda *et al.*, 1998;
940 Slavin *et al.*, 2003]. If we assume a speed of 500 km/s for these plasmoid and TCR
941 events at Mercury, then the average diameters of these structures at Mercury are \sim
942 500 km, or $0.2 R_M$. This compares with ~ 1 to $3 R_E$ plasmoid diameters in the near-tail
943 of Earth [Slavin *et al.*, 2003]. Given the factor ~ 8 scaling between the dimensions of
944 these two magnetospheres, the diameters of plasmoids at these two planets appear to
945 take up similar relative volumes at Mercury and Earth. It should also be noted that
946 "chains" of plasmoids and TCRs, such as displayed in Figure 13, are also common at
947 Earth [Slavin *et al.*, 1993, 2005; Imber *et al.*, 2011]. What is still not understood is
948 whether these chains form simultaneously due to reconnection at multiple X-lines, as
949 sometimes observed in simulations of ion tearing-mode reconnection [Schindler,
950 1974; Tanaka *et al.*, 2011] or to periodic episodes of reconnection at a smaller
951 number of X-lines. Interestingly, the mean interval of 9 sec between the plasmoid and
952 TCR events in Figure 13 is very close to the $\sim 8 - 10$ sec spacing between flux transfer
953 events observed at Mercury by Slavin *et al.* [2012b].

954 In a statistical survey of 49 flux rope-like plasmoids in Mercury's magnetotail,
955 observed between $1.7 R_M$ and $2.8 R_M$ down the tail from the center of the planet,
956 DiBraccio *et al.* [2014] analyzed MESSENGER MAG and FIPS orbital data to
957 determine the average characteristics of these structures. A superposed epoch
958 analysis of the plasmoid-type flux rope events with north-then-south B_z perturbations,
959 consistent tailward motion, from DiBraccio *et al.* is displayed in Figure 14. The
960 magnetic field shows the characteristic variation expected for this type of flux rope
961 [Slavin *et al.*, 2003]. In particular the strong core magnetic field in the +/- Y direction
962 centered on the bi-polar B_z variation associated with the outermost wraps of magnetic
963 flux. DiBraccio *et al.* concluded that This study concluded that the typical plasmoid
964 diameter was ~ 345 km, or $\sim 0.14 R_M$, which is comparable to a proton gyroradius in
965 the plasma sheet, or ~ 380 km. The events in this survey demonstrated that the
966 magnetic variations of flux ropes at Mercury are similar to those observed at Earth but
967 with timescales that are 40 times shorter at Mercury.

968

969

970
971

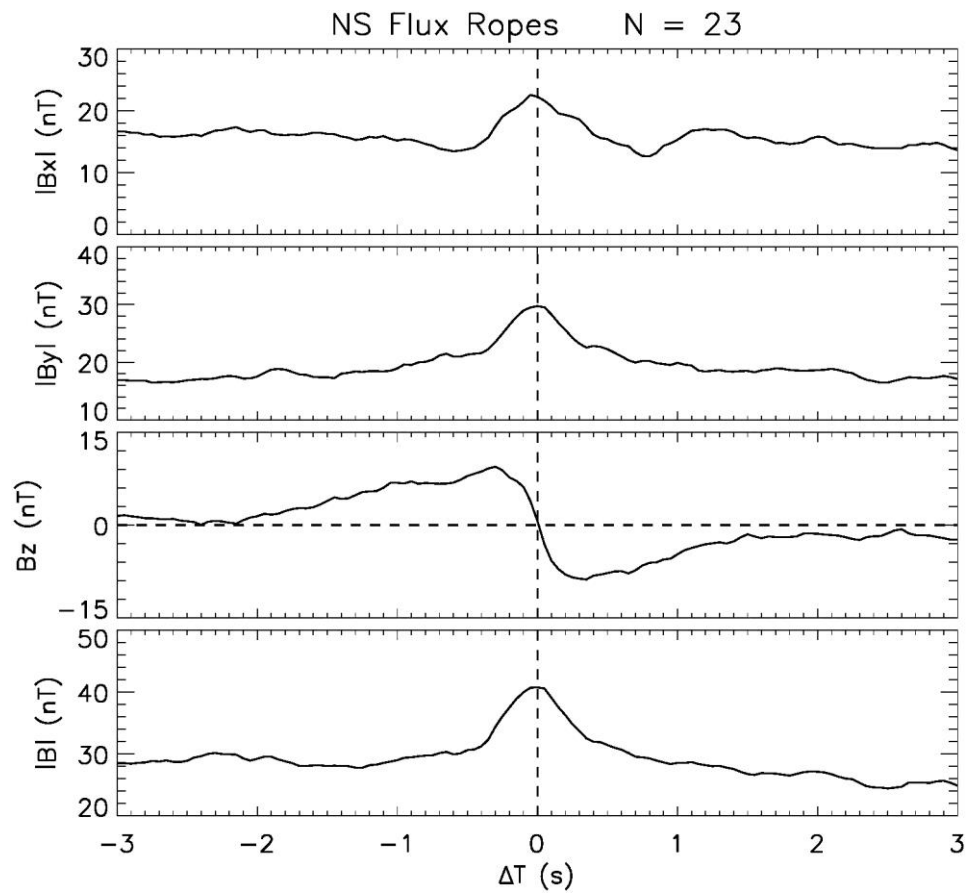


Figure 14. Superposed epoch analysis of the magnetic fields measured during 23 plasmoid-type flux ropes in Mercury Solar Orbital coordinates [from DiBraccio et al., 2014]. Note the strong core magnetic field coincident with the bipolar variation in the B_z perturbation. The continued negative B_z following the plasmoid is due to continued reconnection involving lobe magnetic flux after the plasmoid is released as observed at Earth.

972

973 **4.2 Observations of dipolarization**

974

975

976

977

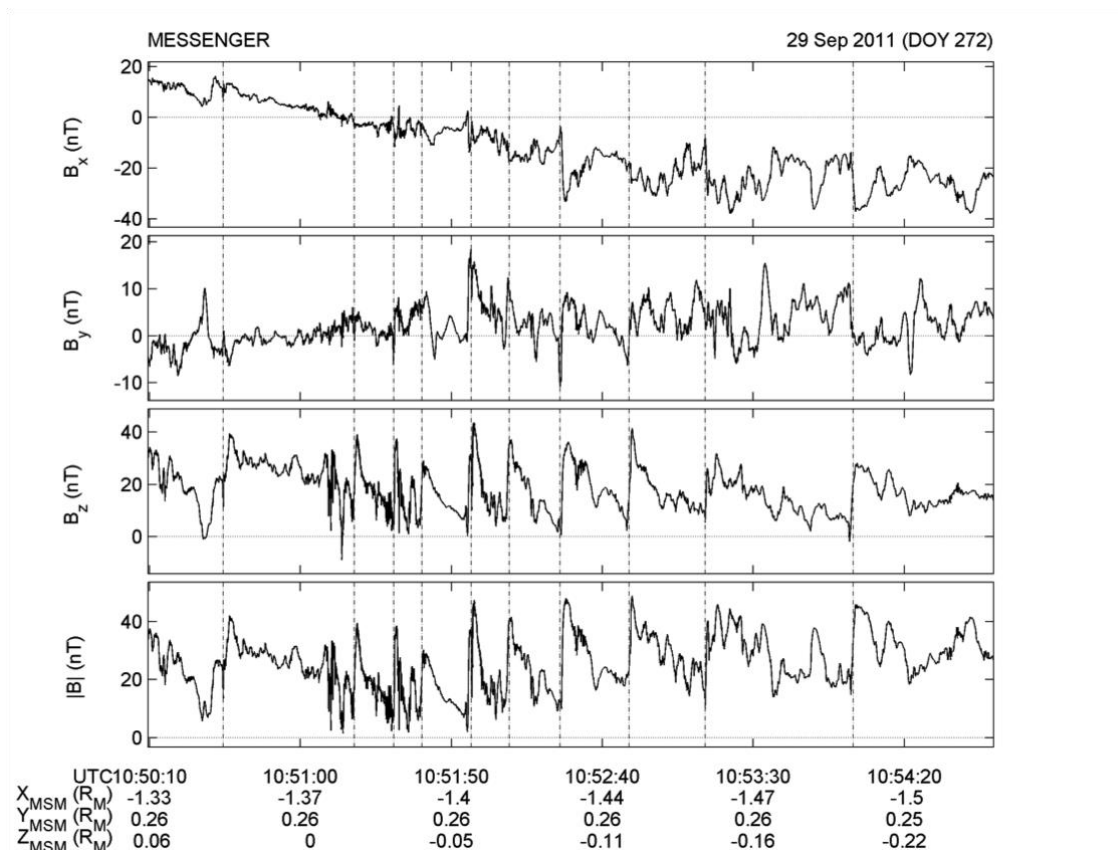


Figure 15. A series of dipolarizations of the magnetic field in the plasma sheet observed by MESSENGER and analyzed by Sundberg et al. [2012]. These brief, several second-long events are marked by vertical dashed line. Each has sudden, strong transitions from the magnetic field being highly stretched to a more dipolar configuration with a greatly enhanced B_z component.

978

979

An integral step in the substorm process is dipolarization of the fields in the near-tail [Baker et al., 1996]. The transient increases in the northward, or dipolar, component of the equatorial magnetic field are closely associated with the braking of sunward directed bursty-bulk flows originating at reconnection X-lines in the magnetotail [Angelopoulos et al., 1994]. This is most readily understood as the result of the reconfiguration of the magnetotail into a lower energy state in which the stretched field lines created by the tail loading process quickly return to a more dipolar configuration [Shiokawa et al., 1997]. At Earth these propagating dipolarization fronts are often accompanied by enhanced ion and electron fluxes up to hundreds of keV due to betatron acceleration as the magnetic field intensity increases [Ashour-Abdalla et al., 2011].

990

991

Earth-like dipolarization events were first observed at Mercury by Mariner 10 during its first flyby in 1974 [Baker et al., 1986; Christon et al., 1987]. The observed magnetic field signatures were in good agreement with those expected from terrestrial dipolarization events, but with durations only of order 1 to 10 sec as opposed to tens of min at Earth. Figure 15 displays an example of dipolarization events at Mercury on 29 September 2011 that have been analyzed by Sundberg et al. [2012]. As shown, a series of 10 dipolarizations are seen to occur during a single plasma sheet encounter of several minutes at a distance of $\sim 1.4 R_M$ downstream of Mercury's terminator plane. The dipolarization events, marked by dashed lines, are evident in the rapid (~ 1 sec) increases and slow (~ 10 s) decays in the B_z component of the magnetic field. The amplitudes of the magnetic field increases are 40–50 nT, similar to such events at

1000

1001 Earth [Runov *et al.*, 2011]. The relatively short lifetime of the events is attributed to
1002 fast decay of the field-aligned currents that must accompany such dipolarizations. At
1003 Earth these currents close through an ionosphere with a conductance that is expected
1004 to be one or even two orders of magnitude larger than that of Mercury's regolith. The
1005 recurrence rate is generally in good agreement with those of plasmoids and traveling
1006 compression regions discussed previously.

1007 **4.3 Precipitation**

1008 **4.3.1 Loss cone determination**

1009 Several studies provided a more quantitative look a proton precipitation at the
1010 cusp. Mapping of plasma pressures to invariant latitude [Korth *et al.*, 2014] showed a
1011 clear north-south asymmetry on the nightside. This indicated increased particle loss
1012 through precipitation in the southern hemisphere, as anticipated from larger cusp that
1013 is created there by the northern offset of the planetary dipole. Winslow *et al.* [2014]
1014 used FIPS data to provide the first quantitative estimates of Mercury's loss cones and,
1015 from those, estimates of the surface fields in the cusp regions. In that work, self-
1016 normalized pitch angle distributions were summed over many cusp passages and then
1017 fit to an equation for pitch angle diffusion. The best-fit solutions gave loss cones of
1018 $121^\circ \pm 3^\circ$ for the northern cusp and 47^{+7}_{-13} in the southern cusp. The locations of the
1019 cusps were also mapped assuming an offset dipole field down from the spacecraft
1020 altitude to the surface. The northern cusp was found to be centered around 76.4° N
1021 latitude and noon local time, with a 15.6° extent in latitude and 7.5 h extent in local
1022 time. In the southern hemisphere, the cusp observations mapped to $23^\circ - 34^\circ$ S
1023 latitude and 16 – 5.3 h local time. MESSENGER's orbit restricted the observation of
1024 the southern cusp to latitudes north of 30° S latitude, so uncertainties in the southern
1025 hemisphere are larger.

1026 **4.3.2 ULF waves**

1027 Ultra-low frequency (ULF) waves were first detected in Mercury's
1028 magnetosphere by Mariner 10 [Russell, 1989]. Aside from acting as an important
1029 mechanism of energy transfer, these waves can increase plasma losses by scattering
1030 them into the loss cone. During the first MESSENGER flyby, Slavin *et al.* [2008]
1031 detected ULF waves in the magnetic field data between closest approach and the
1032 outbound magnetopause crossing with frequencies of ~0.5 to 1.5 Hz. Boardsen *et al.*
1033 [2009] performed a detailed analysis of these waves and found their fundamental
1034 mode was at frequencies between the He⁺ and H⁺ cyclotron frequencies (Figure 16).
1035 Boardsen *et al.* [2009] concluded that wave frequency and amplitude increased from
1036 closest approach to the edge of a boundary layer located adjacent to the
1037 magnetopause; however, the frequency decreased by a factor of two and the
1038 amplitude increased by an order of magnitude inside the boundary layer.

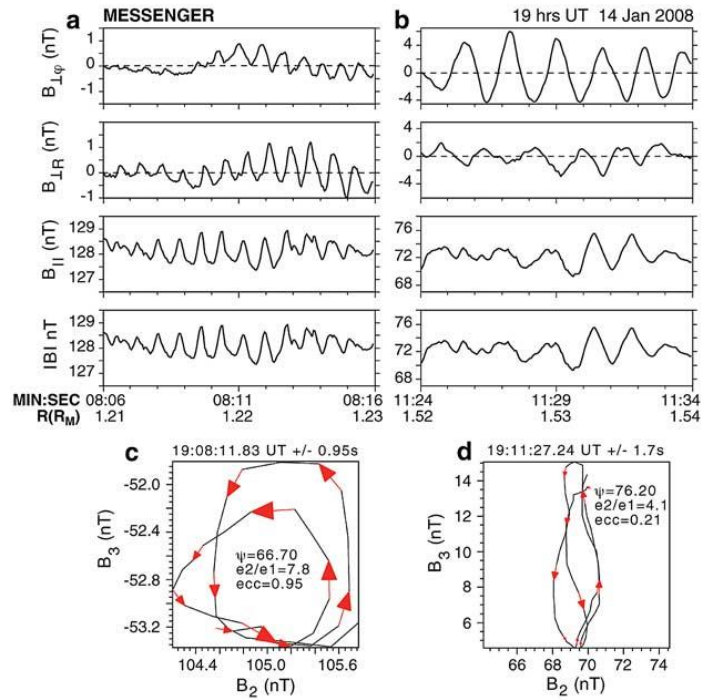


Figure 16. (a) Time-series examples of ULF waves detected outbound from closest approach. (b) Example ULF waves. Hodograms of the time series shown in Figures (c) 2a and (d) 2b. Axes B_2 and B_3 are the directions of intermediate and maximum variance, respectively. The wave-normal angle (Ψ), ratio of median to minimum eigenvalue (e_2/e_1) and ellipticity (ecc) are given for each hodogram. *Adapted from Boardsen et al., [2009].*

1039
 1040
 1041
 1042
 1043
 1044
 1045
 1046
 1047

Also inside Mercury's magnetosphere, *Boardsen et al. [2012]* surveyed coherent ULF waves at frequencies between 0.4–5 Hz. They were observed at the inner magnetosphere ($R < 0.2 R_M$) at all MLTs. The waves are observed to be compressional and at maximum power near the equator on the nightside (Figure 17), and become transverse with power decreasing for increasing magnetic latitudes. On average, the waves are strongly linear with wave-normal angles peaked around 90 deg and elliptical values < 0.3 .

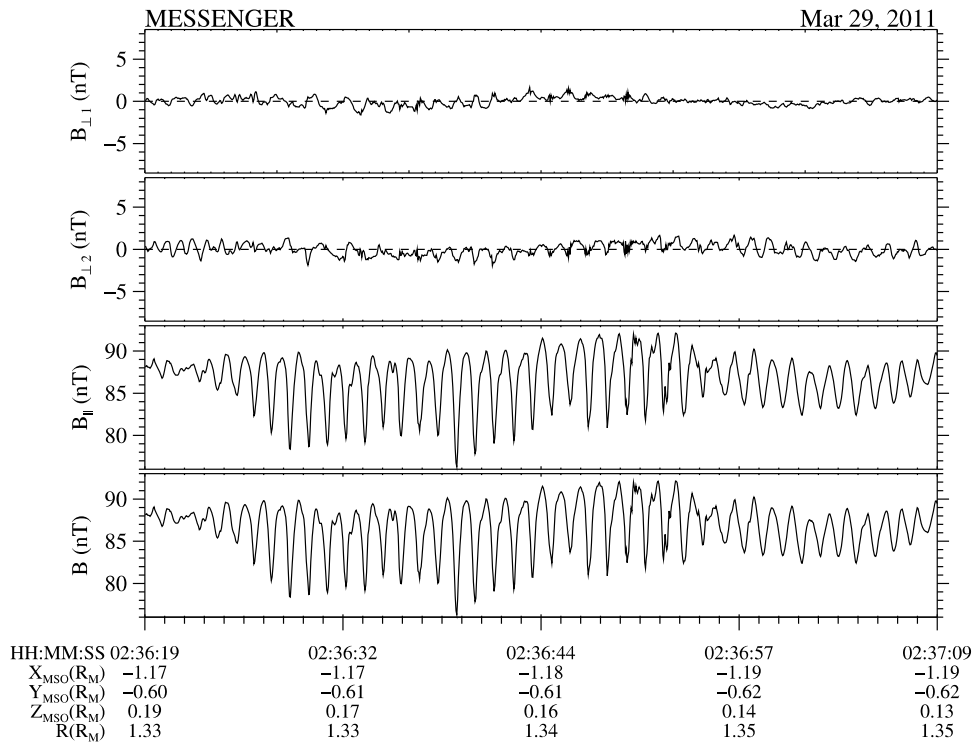


Figure 17. Strongly compressional waves near Mercury’s magnetic equator. Perpendicular components of the field from two-dimensional MVA are shown in the first (minimum perpendicular variance) and second (maximum perpendicular variance) panels. The third panel is the parallel field component and the fourth panel is the field magnitude. Peak-to-peak amplitudes are 10 nT. *Adapted from Boardsen et al. [2012].*

1048 5 Modeling

1049 5.1 Global Modeling of Mercury’s Magnetosphere

1050 5.1.1 MHD and hybrid models of Mercury’s magnetosphere

1051 Global simulation models have been developed and applied to Mercury to
 1052 understand the solar wind-magnetosphere interaction. These global models provide
 1053 global context for interpreting and linking measurements obtained in various parts of
 1054 the system, thereby extending our knowledge of Mercury’s magnetospheric
 1055 environment beyond that available from localized spacecraft observations. Two types
 1056 of simulation models have been widely used in the global modeling of Mercury’s
 1057 magnetosphere, i.e., magnetohydrodynamic (MHD) simulation and hybrid simulation.

1058 Global MHD simulation, in which both ions and electrons are treated as fluid,
 1059 usually can provide a description of the global interaction over a reasonably large
 1060 region around the obstacle and with relatively high resolution at a feasible
 1061 computational cost. MHD models have been used to characterize the large-scale
 1062 structure of Mercury’s magnetosphere under various solar wind and IMF conditions.
 1063 For example, *Kabin et al. [2000]* employed a single-fluid MHD model to characterize
 1064 the configuration of Mercury’s magnetosphere under extreme solar wind dynamic
 1065 pressure conditions. *Ip and Kopp [2002]*, also using a global MHD model,

1066 investigated the response of Mercury's magnetospheric configuration to different IMF
1067 orientations focusing particularly on the size of the polar caps, through which the
1068 solar wind particles can gain access to Mercury's surface. Recent MHD modeling
1069 efforts have been made to extend single-fluid MHD to multi-fluid MHD models.
1070 *Kidder et al.* [2008] adapted a multi-fluid model to Mercury that tracks the solar wind
1071 protons and planetary ions of Mercury origin as separate fluids, allowing for studying
1072 the effects of planetary heavy ions on the global magnetospheric structure. *Benna et*
1073 *al.* [2010] applied a two-fluid, Hall-MHD model in which the ion and electron fluids
1074 are treated separately with the inclusion of the Hall physics within the ideal MHD
1075 framework.

1076 Another type of global simulations frequently used in the modeling of Mercury's
1077 magnetosphere is the hybrid model in which electrons are treated as a massless fluid
1078 while ions are represented as individual macro-particles. This allows for modeling
1079 ion kinetic effects, e.g., finite gyroradius effects and non-Maxwellian particle
1080 distributions. Compared to MHD simulation, hybrid simulation normally needs
1081 relatively expensive computational resources to achieve reasonably good resolution
1082 and to reduce system noise. With the rapid increase of computing power, it has
1083 recently become viable to apply a three-dimensional hybrid model to simulate
1084 Mercury's magnetosphere on a global scale [e.g., *Kallio and Janhunen*, 2003;
1085 *Travnicek et al.*, 2007, 2010; *Wang et al.*, 2010; *Müller et al.*, 2012; *Richer et al.*,
1086 2012]. These hybrid simulations have provided significant insights into many of the
1087 fundamental plasma processes operating in Mercury's magnetosphere, especially
1088 those on the ion kinetic scale, such as energy-dependent particle drifts and wave
1089 generations resulting from ion temperature anisotropy.

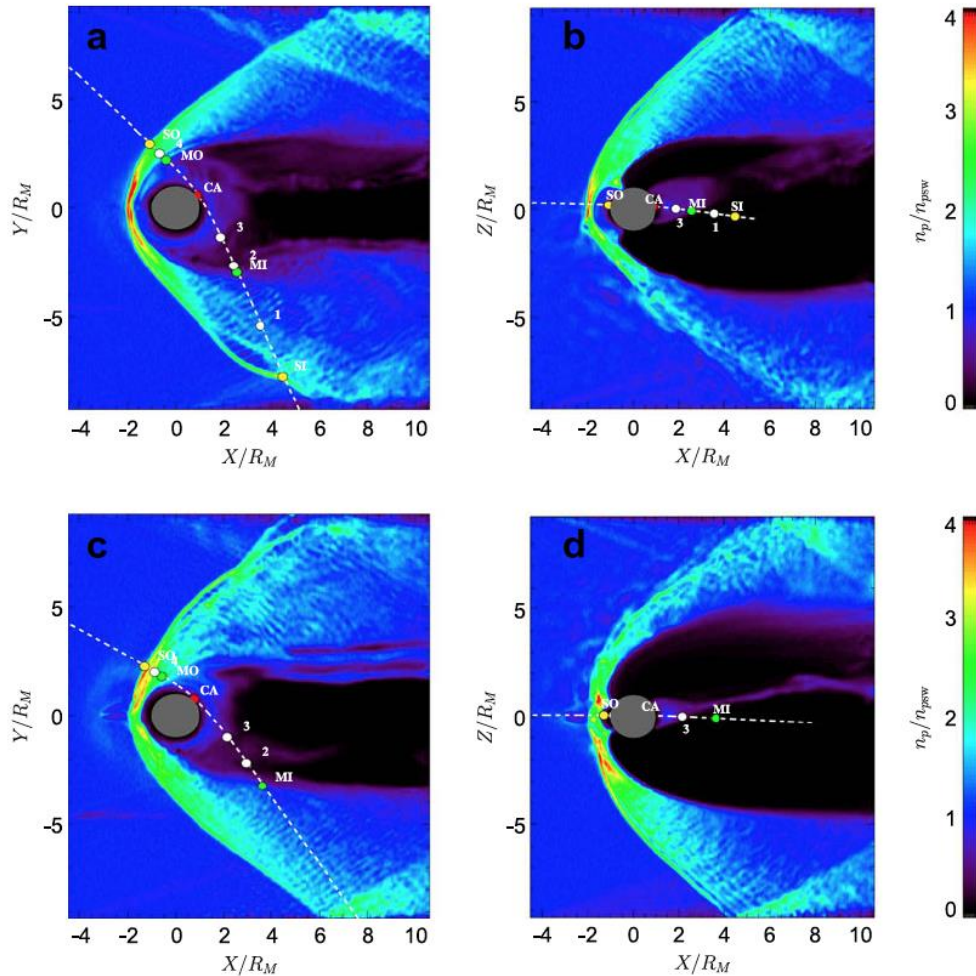


Figure 18: Simulated magnetospheric configuration from the global hybrid model of *Travenick et al. (2010)*. Panels (a) and (b) show the simulated solar wind proton density in the equatorial and noon-midnight meridional planes, respectively, under northward IMF conditions. Panels (c) and (d) are the same but for southward IMF. Colors in each panel represent the density of solar wind protons normalized to the upstream value. MESSENGER trajectories of the M1 and M2 flybys are superimposed as white dashed lines.

1090 5.1.1.1 Solar wind entry into the magnetosphere

1091 Various modeling studies using global MHD and hybrid simulations have in
 1092 general confirmed the picture of Mercury's magnetosphere derived from
 1093 measurements, that reconnection is the dominant process transferring solar wind
 1094 plasma and energy into Mercury's magnetosphere. Modeling has also shown that
 1095 other boundary processes, such as the Kelvin-Helmholtz instability [*Paral and*
 1096 *Rankin, 2013*] and ion kinetic motion across the magnetopause due to finite
 1097 gyroradius effect [e.g., *Müller et al., 2012*], also contribute to the transfer of
 1098 magnetosheath plasma into the magnetosphere as observed by MESSENGER. As an
 1099 example, Figure 18 shows the large-scale configuration of Mercury's magnetosphere
 1100 from the hybrid model of *Travenick et al. [2010]*. Familiar magnetospheric structures
 1101 can be readily identified in the figure, such as the bow shock, magnetosheath, cusps,
 1102 tail lobes and plasma sheet. Several modeling studies based on MHD and hybrid
 1103 simulations have found that Mercury's magnetosphere changes its configuration

1104 considerably when the IMF orientation varies. In particular, as shown in Figure 18,
 1105 the dayside magnetopause is located closer to the planet during southward IMF
 1106 compared to northward IMF [e.g., *Ip and Kopp, 2002; Kidder et al., 2008; Travenick*
 1107 *et al., 2010*], consistent with the suggestion by *Slavin and Holzer [1979]* that
 1108 enhanced low-latitude reconnection during periods of southward IMF can effectively
 1109 erode the dayside magnetopause causing the boundary to move closer to the planet's
 1110 surface. Correspondingly, the location and morphology of the cusps, through which
 1111 the solar wind plasma can gain access to the low altitude region, also vary in response
 1112 to solar wind and IMF changes. As described above, however, analysis of
 1113 MESSENGER data [e.g., *DiBraccio et al., 2013*] does not support the strong bias of
 1114 reconnection rate based on IMF direction alone. This behaviour has not yet been
 1115 captured in global models of Mercury's magnetosphere.

1116 Aside from the IMF, solar wind dynamic pressure is another important factor
 1117 that can significantly affect the size and configuration of Mercury's magnetosphere.
 1118 *Kabin et al. [2000]* using an MHD model simulated Mercury's interaction with the
 1119 solar wind for different upstream pressures. They showed that under extremely high
 1120 solar wind dynamic pressure conditions Mercury's dayside magnetopause can be
 1121 pushed all the way to the surface, a situation in which the solar wind plasma can
 1122 directly impinge on the planet. Similar results have also been found in the hybrid
 1123 simulation by *Kallio and Janhunen [2003]*. However, results from MESSENGER
 1124 observations paint a more nuanced picture: *Slavin et al. [2014]* found that increases
 1125 in magnetic field due to induction in the planet's core act to resist this compression,
 1126 where the resulting stand-off distance is the result of competition between these two
 1127 processes. Some models now included this induction (Section 5.1.1.3 below).

1128 5.1.1.2 Precipitation of solar wind particles onto Mercury's surface

1129 Once the solar wind enters the magnetosphere, the bulk of the plasma follows
 1130 the large-scale Dungey cycle magnetospheric convection driven by the solar wind.
 1131 Since precipitation of solar wind particles onto Mercury's surface is a major of its
 1132 exosphere and magnetosphere, it is of high interest to derive from global
 1133 magnetosphere models quantitative information about this process as well as its
 1134 dependence on the internal and external conditions.

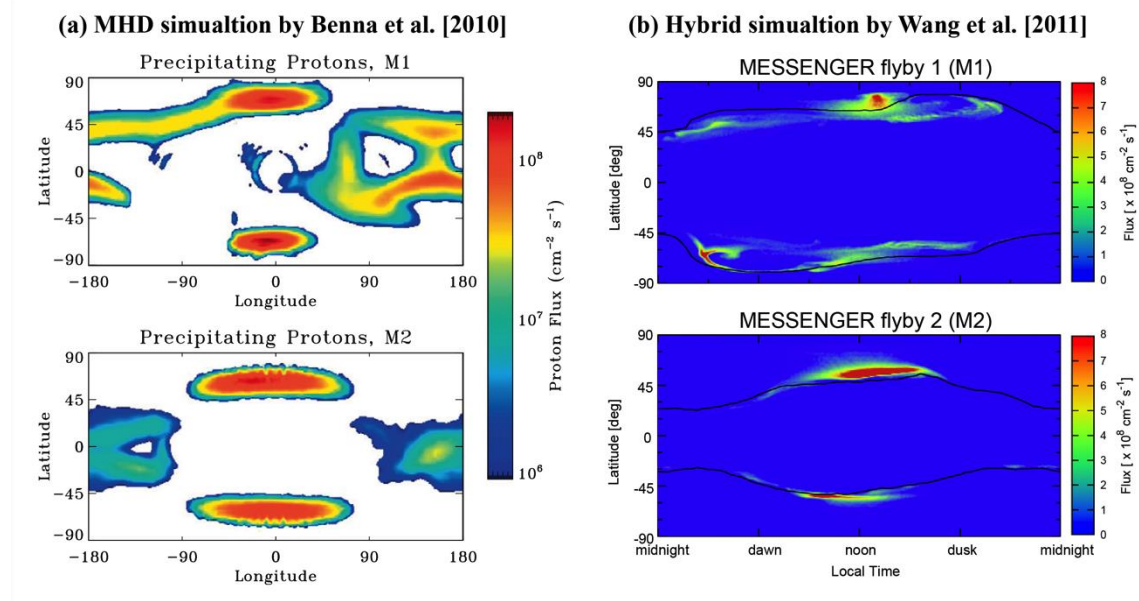


Figure 19. Maps of precipitating solar wind proton fluxes (in the unit of particles per cm^2 per

second) predicted by global magnetosphere simulations for the MESSENGER M1 and M2 flyby conditions. (a) From the MHD model by *Benna et al.* [2010] (figure adapted from *Burger et al.*, 2010). (b) From the hybrid model by *Wang and Ip* [2011]. For each model, the top panel shows the precipitation map for the M1 flyby conditions while the bottom panel is for the M2 flyby.

1135

1136 Figure 19 shows maps of the solar wind precipitation onto Mercury's surface
1137 as predicted by MHD and hybrid simulations for the first two MESSENGER flybys.
1138 It should be noted that the two simulation models discussed here used different
1139 modeling approaches (MHD versus hybrid) and differ in many aspects, such as the
1140 input parameters and details of the numerical codes. Nevertheless, the two models
1141 give qualitatively similar results on the general features of ion precipitation. In
1142 general, there are two main regions on the surface to which solar wind particles can
1143 have access. One is the cusp region on the dayside and the other is the low-latitude
1144 region on the night side. As mentioned above, the location and size of the two cusps
1145 responds to IMF changes. This can be clearly seen by comparing the precipitation
1146 maps between the cases for the M1 (northward IMF) and M2 (southward IMF) flybys.
1147 The peak fluxes are centered above 70 degree latitude for the M1 flyby conditions
1148 whereas they move equatorward to about 65 degree latitude for the M2 flyby
1149 conditions, which is in accordance with the variation of the open-closed field line
1150 boundary as shown in the hybrid case (Figure 19(b)). Both models predict a
1151 noticeable north-south asymmetry in the impact rate and the spatial distribution of the
1152 cusp precipitation. Such an asymmetry has been suggested to arise from the presence
1153 of a strong B_x component in the IMF [*Sarantos et al.*, 2001], a typical feature of the
1154 Parker spiral at Mercury's orbit. *Benna et al.* [2010] attributed a north/south
1155 asymmetry in the sodium density observed during a MESSENGER flyby to this
1156 precipitation flux asymmetry. Others have also invoked ion flux to help explain
1157 sodium exosphere observations via the processes of ion sputtering, ion-enhanced
1158 diffusion, and chemical sputtering, as in the Monte Carlo models of *Mura et al.*
1159 (2009), *Leblanc and Johnson* (2010), and *Burger et al.* (2010). In later work, the
1160 north/south asymmetry in precipitation was attributed mostly to Mercury's offset
1161 magnetic dipole [e.g. *Winslow et al.*, 2014].

1162 Ion precipitation is seen on the night side mainly at low latitudes where the
1163 magnetic field lines are closed field lines with both ends connected to the planet. The
1164 existence of such an ion impact region is consistent with the expectation that
1165 Mercury's plasma sheet ions have relatively large loss cone [*Korth et al.*, 2014]
1166 because of the planet's weak intrinsic magnetic field. While the MHD and hybrid
1167 models show similar features of the cusp precipitation, the nightside precipitation
1168 appears to have different characteristics between the two models. The MHD model
1169 predicts a broad region of ion precipitation on the night side, which has been
1170 attributed to the absorption of particles in the drift belt formed in the equatorial
1171 region. Hybrid models, on the other hand, also predict the existence of such a drift
1172 belt near the planet [e.g., *Travenick et al.*, 2010]. However, a surprising result of the
1173 hybrid simulations [e.g., *Travenick et al.*, 2010; *Wang et al.*, 2011] is that those ions
1174 precipitate onto the surface primarily at high latitudes, instead of near the equator as
1175 one might expect on the basis of finite gyroradius effect.

1176 In addition to the external conditions, the internal conditions, such as the
1177 magnetic properties of the planet, may also affect the distribution of ion precipitation
1178 onto the surface. *Richer et al.* [2012] using a hybrid model explored the sensitivity of
1179 the global magnetospheric interaction to details of Mercury's intrinsic magnetic field.
1180 Two different internal field representations were used in their simulations: one

1181 contains a northward offset dipole [Anderson *et al.*, 2011] and the other is a
1182 combination of a centered dipole and quadrupole fitted to the offset dipole derived
1183 from MESSENGER observations. They found that while the two internal field models
1184 yielded similar magnetic configuration in the northern hemisphere, the north-south
1185 asymmetry is more pronounced in the case with the a dipole plus a quadrupole field.
1186 This leads to very different precipitation patterns between the northern and southern
1187 hemispheres, an interesting result that needs to be checked against with observations
1188 of the low-altitude region of the southern hemisphere from future missions to
1189 Mercury, such as the BepiColombo mission.

1190 *5.1.1.3 Simulation of the induction effect arising from the planetary core*

1191 There is no doubt that the electromagnetic coupling between the planetary interior
1192 and the magnetosphere is an important element of Mercury's interaction system that
1193 needs to be included in global modeling, especially when considering the system
1194 response to time-varying external conditions. Most the global models applied to
1195 Mercury thus far excluded the planetary interior from the simulation domain. In those
1196 models, the electrical properties of the planet are mimicked through prescription of
1197 boundary conditions. To properly model the coupling between the magnetosphere and
1198 the core, it is desirable to explicitly include the planetary interior as part of the
1199 simulation domain. Such an attempt has been undertaken by Müller *et al.* [2012], who
1200 adapted a 3D hybrid model previously applied to planetary moons to Mercury and
1201 included the planetary interior with a specified conductivity distribution. The model
1202 has been applied to simulate MESSENGER flybys and shown to reproduce
1203 MESSENGER observations reasonably well. However, the induction effect arising
1204 from the core was not clearly demonstrated because the model employed steady solar
1205 wind conditions as input and focused on the steady-state behavior of the
1206 magnetosphere, as what has been done with most global models applied to Mercury.
1207 Jia *et al.* [2013] recently developed a global resistive MHD model that also explicitly
1208 includes the planetary interior with layers of different conductivities in their
1209 simulation. To characterize how the coupled system dynamically responds to the
1210 external forcing, they drive the simulation by using time-dependent solar wind
1211 conditions containing different types of disturbances typical of those seen at
1212 Mercury's orbit, such as Coronal Mass Ejections (CMEs) and IMF rotations. Their
1213 results show that the reconfiguration of Mercury's magnetosphere indeed induces
1214 intense electric currents at the core where the electrical conductivity is high.
1215 Associated with those induced currents are strong magnetic perturbations present not
1216 only inside of the planet but also throughout the magnetosphere, clearly
1217 demonstrating that the induction effect plays an important role in determining the
1218 global magnetospheric structure.

1219 While the modeling efforts discussed above represent a first step in characterizing
1220 Mercury's magnetosphere-core coupling in a self-consistent manner, future work is
1221 clearly needed to further quantify the induction effect. A particularly important
1222 question that should be addressed with self-consistent global simulations is how the
1223 strong magnetosphere-core coupling affects the extent to which the solar wind
1224 particles can have access to the planet's surface, which is of direct relevance to the
1225 plasma sources of Mercury's magnetosphere.

1226 5.1.2 Exospheric Modeling

1227 Global models of Mercury's neutral exosphere have made significant
1228 contributions to understanding of its origin from complex interactions between the
1229 Sun and the surface of the planet, as well as of seasonal variations due to Mercury's
1230 highly elliptical orbit [*Leblanc and Johnson, 2003, 2010; Mura et al., 2007; Burger et*
1231 *al., 2010, 2012; Wurz et al., 2010; Sarantos et al., 2011; Pfleger et al., 2015*]. Since
1232 the exosphere is collisionless, particle dynamics in these models are determined rather
1233 simply by gravity and radiation pressure; however, the sources and sinks of the
1234 exosphere add considerable complication and are the main area of active
1235 development. Global models typically include the source processes that have been
1236 described in Section 3.2.1: thermal desorption, ion sputtering, photon-stimulated
1237 desorption and micrometeoroid vaporization (TD, IS, PSD and MV). Additionally, the
1238 main loss processes included are photoionization, surface sticking and gravitational
1239 escape. Of these three loss mechanisms, photoionization of exospheric neutral atoms
1240 is particularly important because it is also a significant *source* of planetary ions to
1241 Mercury's magnetosphere. The physics of these processes is well understood from
1242 laboratory measurements. Nevertheless, there is sufficient uncertainty in crucial
1243 parameters – such as Mercury's surface composition and the incident solar wind
1244 plasma – that the relative contributions of these processes are not well determined.
1245 Many researchers have sought to remedy this problem by using observations to
1246 constrain their models, either from Earth (ground-based) or MESSENGER. This
1247 synthesis of models and observations has been very effective in narrowing the
1248 parameter space, but the relative contributions of the various surface processes are
1249 still in dispute.

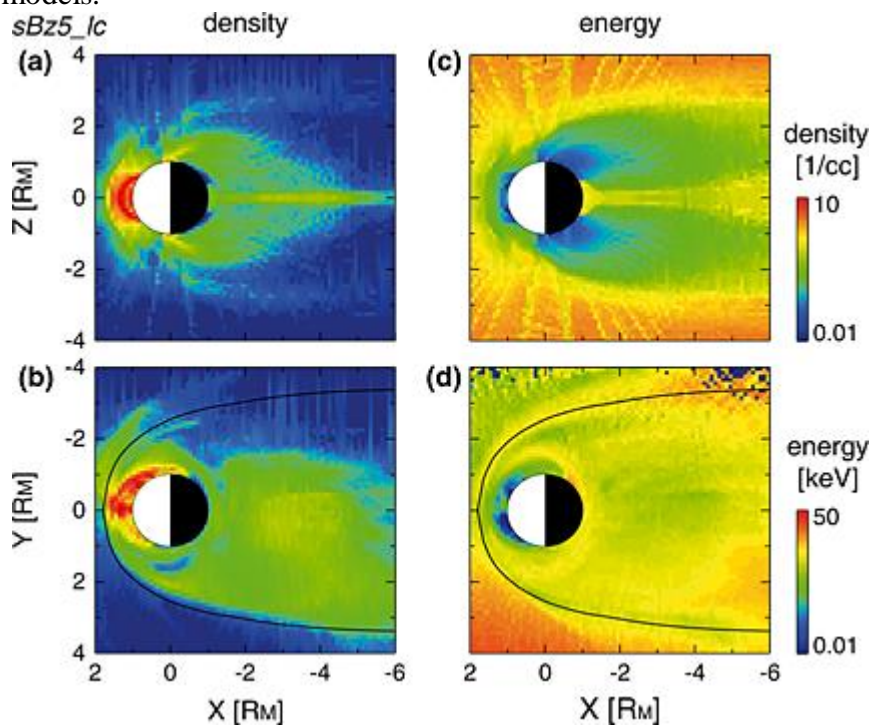
1250 A subset of global exosphere models are able to simulate the dynamics of
1251 planetary ions in the system once they are created [*Sarantos et al., 2009*]. This
1252 modeling capability is key to obtain a global understanding of plasma sources into
1253 Mercury's magnetosphere. It provides, thus far, the only quantitative connection to
1254 planetary ion sources from both the exosphere and surface, though their relative
1255 importance is also an open question. To model ion dynamics, exospheric models
1256 must also include the electric and magnetic fields of the magnetosphere. These
1257 models primarily focus on planetary ions, which are much lower in abundances than
1258 the solar wind ions that drive the magnetosphere. As a result, they incorporate static
1259 fields, typically from MHD models. Planetary ions are then *flown* through these
1260 fields by integrating their equation of motion directly. The ions are often treated as
1261 test particles, each representing a larger number of ions in the real system.

1262 The ion component of global exospheric modeling can feedback into
1263 understanding the composition of the exosphere itself. From MESSENGER FIPS
1264 measurements, as well as from ion composition measurements around the Moon [e.g.,
1265 *Mall et al., 1998*], we know that many more species exist that have not been observed.
1266 Many of these atmospheric species do not have emission lines in the MESSENGER
1267 UltraViolet and Visible Spectrometer (UVVS) spectral range; therefore FIPS
1268 measurements present the only way to update upper limits prior to BepiColombo orbit
1269 insertion. The observed seasonal variability of the exosphere [e.g., *Leblanc and*
1270 *Johnson, 2010, for Na; Burger et al., 2014, for Ca*] has not yet been folded into ion
1271 model calculations.

1272

1273 **5.1.2.1 Ions from the exosphere**

1274 Na⁺ of exospheric origin is the only species that has been systematically
 1275 studied with simulations. Trajectory tracings of Na ion test particles were performed
 1276 in analytical [Delcourt *et al.*, 2003], resistive MHD [Yagi *et al.*, 2010; Seki *et al.*,
 1277 2013], Hall MHD [Sarantos *et al.*, 2009] and hybrid [Paral *et al.*, 2010] simulated
 1278 fields (Figure 20). For the first three the exospheric model of Leblanc and Johnson
 1279 [2003] was used, in which the finite Na reservoir is quickly depleted by thermal
 1280 desorption leading to an exosphere with a dawn-dusk asymmetry, whereas the other
 1281 two considered different mixes of photon stimulated desorption and sputtering, both
 1282 spherically symmetric with respect to the Sun-Mercury line. Unfortunately, because
 1283 of the small size of Mercury's magnetosphere, these tracings are very sensitive to the
 1284 treatment of the inner boundary condition [Seki *et al.*, 2013] and therefore differ
 1285 between models.



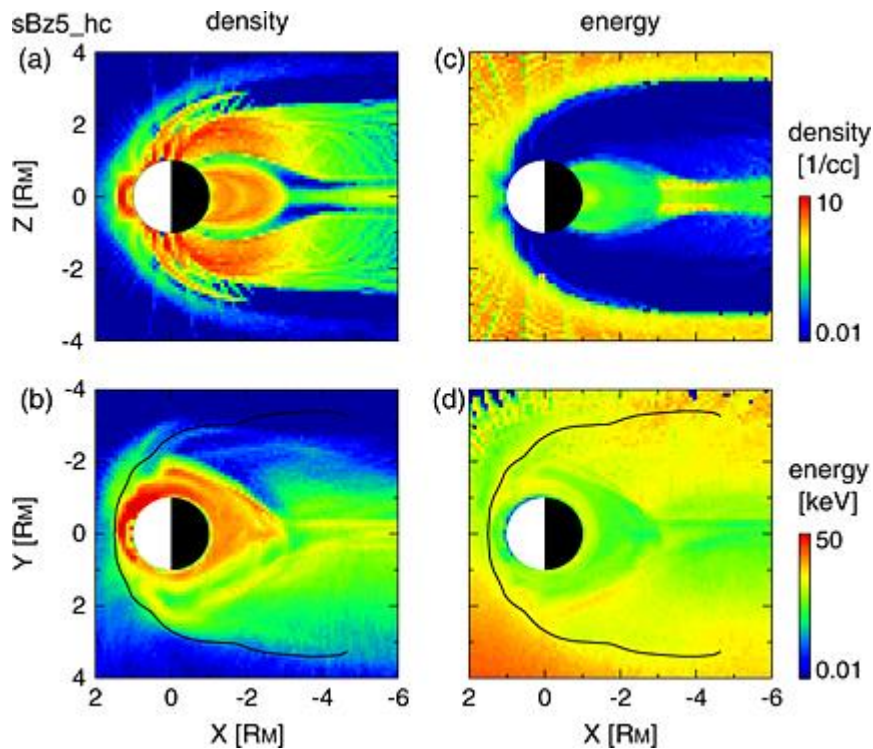


Figure 20. Na ion distribution under the same southward IMF ($B_z = -5$ nT) and solar wind conditions, initialized with the same exosphere model, but subject to different assumptions of the inner boundary condition. Case with high surface conductance shown in the bottom panel. The resulting ion distributions are markedly different as the formation of an X-line further from the planet inhibits escape in the second case. [From Seki et al., 2013]

1286

1287

1288 A common feature of these simulations is an enhancement of Na^+ near dawn
 1289 and in the morning sector. The estimated concentration peaks exceeded $10 \text{ Na}^+ \text{ cm}^{-3}$
 1290 near the equator [Yagi et al., 2010]. The pressure exerted by planetary ions in these
 1291 simulations can locally surpass 10% of the total, thus necessitating that sodium
 1292 becomes one of the species of the MHD and hybrid simulations. Escape of planetary
 1293 ions through a porous magnetopause, especially under southward IMF conditions, is
 1294 evident in the simulations [Paral et al., 2009].

1294

1295 Magnetospheric ion recycling and its effect has been the subject of several
 1296 works. "Self sputtering" is itself an inconsequential source for the exosphere [e.g.,
 1297 Delcourt et al., 2003; Poppe et al., 2013] as the recycled ion fluxes are a small
 1298 portion of the inferred neutral efflux ($\sim 10^7 \text{ Na cm}^{-2} \text{ s}^{-1}$). However, recycling could be
 1299 important if ions neutralized in the soil increase the available reservoir for trace
 1300 species [Killen et al., 2004]. High ion recycling rates will obviously increase the
 1301 reservoir for exogenous species of the exosphere that are in balance with the solar
 1302 wind influx (e.g., He, Ne); but they could also increase the reservoir for exospheric
 1303 Na and K, which are very nearly depleted on the dayside [Leblanc and Johnson, 2003,
 1304 2010] to levels that can be supported by grain diffusion [Killen et al., 2004]. Broad
 1305 bands of nightside precipitation of Na^+ with fluxes $\sim 10^5 \text{ Na}^+ \text{ cm}^{-2} \text{ s}^{-1}$ and extending
 1306 up to $\pm 50^\circ$ latitude form when realistic conditions about the surface conductance are
 1307 adopted [Seki et al., 2013]. These contain sub-keV ions which are deposited very near
 1308 the top of the grains and should quickly diffuse to the grain surface. Schmidt [2013]
 1309 proposed that ion precipitation to Mercury's nightside, which is shifted northward
 because the geomagnetic equator is displaced with respect to the geographic equator,

1310 is a mechanism for producing the north-south asymmetries of the dayside Na
1311 exosphere observed from ground-based telescopes [e.g., *Potter et al.*, 2006].

1312 **5.1.2.2 Ions from the surface**

1313 Both precipitating protons and electrons can contribute to a surface ion source.
1314 *McLain et al.* [2011] suggested that electron stimulated desorption (ESD) could be an
1315 important source of Mercury's ions. Thresholds for such emission (~20 eV) are
1316 typically too high for solar wind electrons impinging onto the Moon but can clearly
1317 be exceeded at Mercury. While the typical yield for sputtered ions by proton
1318 impingement is in the range of 10^{-4} to 10^{-1} per impacting ion [*Benninghoven*, 1975],
1319 the yields measured for ESD could be ten times higher, especially the more energetic
1320 the incident electrons [*Wang et al.*, 1984]. Ions and electrons from the solar wind
1321 should precipitate not only onto Mercury's cusp areas but also persistently onto the
1322 nightside in auroral regions as well as regions surrounding the geomagnetic equator
1323 [e.g., *Benna et al.*, 2010]. Thus, the Hermean surface at high latitudes of the dayside
1324 and low latitudes of the nightside are regions of planetary ion emission.

1325 Outflow of ions released directly from the surface could be responsible for
1326 some of the cusp signatures observed by MESSENGER FIPS [*Raines et al.*, 2014].
1327 Despite their sub-escape initial energies (~1 eV), such ions will be rapidly accelerated
1328 by centrifugal sources and escape into the magnetosphere [*Delcourt et al.*, 2012].
1329 Their importance relative to photoions is uncertain. At the Moon, predictions from
1330 *Sarantos et al.* [2012] suggest that ions from exospheric neutrals dominate over
1331 surface ions for many metallic constituents such as Na⁺, although for some species
1332 with more stringent exospheric limits (e.g., Ca⁺) the surface should be the most
1333 important source. At Mercury such calculations are yet to be performed.

1334 **5.1.2.3 Estimating total ion source rates**

1335 Models of the exosphere can provide a rough estimate for the sodium ion
1336 source rate in Mercury's magnetosphere, indirectly, via the commonly reported
1337 quantity of total exosphere content and the assumption, common to all models, that
1338 photoionization is the dominant ionization process. The answer varies from model to
1339 model, of course, but despite their major differences, all sodium models estimate the
1340 *content* to be on the order of 10^{28} sodium atoms [the exosphere content ranges 0.3-
1341 4×10^{28} in the following: *Smyth and Marconi*, 1995; *Killen et al.*, 2001; *Mura et al.*,
1342 2009; *Leblanc and Johnson*, 2010; *Mouawad et al.*, 2011].

1343 These models do not use the same data sets and they even have different basic
1344 assumptions, yet they estimate the sodium content within the same order of
1345 magnitude. Consider the difference between the models described by *Leblanc and*
1346 *Johnson* [2003, 2010] and *Burger et al.* [2010]: the two models have quite different
1347 mixtures of source processes and, even more fundamentally, differ in basic
1348 construction. The exosphere in *Leblanc and Johnson* is coupled to a large reservoir of
1349 adsorbed sodium atoms on Mercury's surface, while *Burger et al.* have no reservoir.
1350 *Leblanc et al.* [2010] ran their model for several simulated Mercury years and
1351 matched their results to several Earth years of ground-based observations; the *Burger*
1352 *et al.* model only simulated several hours and compared their result data taken during
1353 two of MESSENGER's Mercury flybys.

1354 The the ion source rate can be estimated from published results by multiplying
1355 this exosphere content by the photoionization frequency, which is on the order of 10^{-4}
1356 s⁻¹ [*Huebner et al.*, 1992]. Assuming that most of the exosphere is exposed to

1357 sunlight, this gives a sodium ion source rate on the order of 10^{24} sodium ions s^{-1} , or a
1358 mass loss of several 10s of $g s^{-1}$. This is comparable to the ion outflow from the other
1359 terrestrial planets [Strangeway *et al.*, 2010], but some fraction of Mercury's ion
1360 production is lost to its surface. As discussed above, Na^+ is the most abundant
1361 planetary ion detected by FIPS. Ionized magnesium may contribute to the sodium ion
1362 signature owing to its similar mass, but it is much less abundant in the exosphere and
1363 has a longer lifetime against photoionization.

1364 Sodium is the most abundant exospheric species identified so far, but there are
1365 several others. During one of MESSENGER's Mercury flybys, UVVS observed
1366 simultaneously neutral and ionized Ca (Figure 21). The observed sharp decrease in Ca
1367 away from the planet can be explained by quick ionization [Vervack *et al.*, 2010] and
1368 models applied to MASCS data support a strong localized source at dawn at high
1369 temperature (>50000 K), probably related to micrometeoritic impact vaporization of
1370 Ca in the form of CaO and CaOH, and subsequently dissociated [Burger *et al.*, 2014].
1371 The model of UVVS calcium observations provides a Ca^+ photoion source on the
1372 order of 10^{23} calcium ions s^{-1} [Burger *et al.*, 2014], though much of the calcium is
1373 ionized beyond the magnetosphere owing to its high-energy ejection process.
1374 Hydrogen and helium gases are thought to be neutralized solar wind plasma that are
1375 later (re-) ionized to contribute to the planetary ions detected by FIPS. The planetary
1376 helium is distinct from solar wind helium as it is singly, rather than doubly, ionized.
1377 Broadfoot *et al.* [1976] estimated that most of the planetary helium escapes Mercury's
1378 gravity before photoionization, although the energy distribution of the neutral helium
1379 is highly uncertain [Shemansky and Broadfoot, 1977; Leblanc and Chaufray, 2011].
1380 Broadfoot *et al.* [1976] estimated that the helium ion source rate from the helium
1381 exosphere is on the order of 10^{22} helium ions s^{-1} .
1382

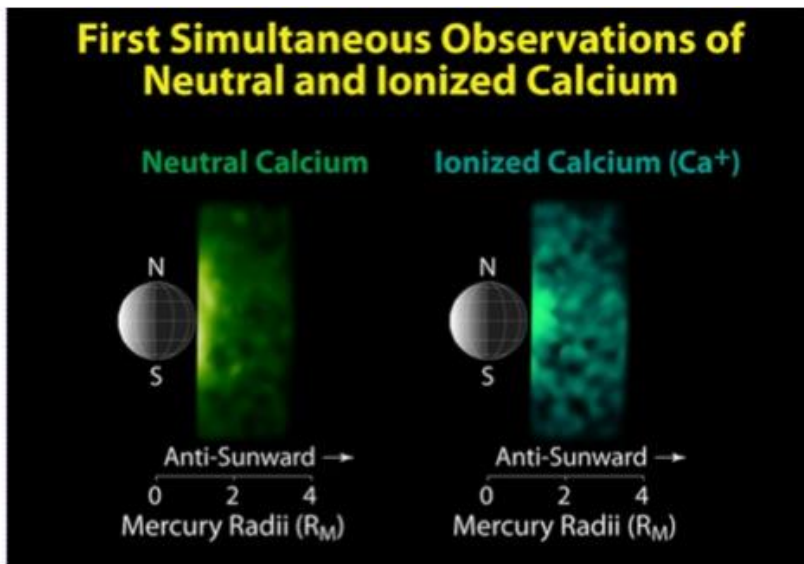


Figure 21. Ca and Ca^+ distribution tailward as detected by MESSENGER MASCS UVVS during flybys. *Additional (unpublished) material from Vervack *et al.*, [2010].*

1384 5.2 Ion Acceleration Processes and Non-adiabatic Behavior

1385 5.2.1 Centrifugal acceleration in Mercury's lobes

1386 To the first order, the large scale plasma circulation at Mercury resembles that
1387 at Earth, the coupling between the magnetosphere and the interplanetary magnetic
1388 field being responsible for a dawn-to-dusk convection electric field with antisunward
1389 transport at high latitudes (typically, above 50°) and return sunward flow at low
1390 latitudes. In this context, a process that readily affects planetary ions after their
1391 ejection into the magnetosphere is the centrifugal acceleration associated with the
1392 large scale $\mathbf{E} \times \mathbf{B}$ transport. Using a guiding center approach, *Cladis* [1986] showed
1393 that, during transport from high to low latitudes, ions expelled from the topside
1394 terrestrial ionosphere may be subjected to substantial acceleration in the parallel
1395 direction. Because of the small spatial scales of the Hermean environment, it was
1396 pointed out by *Delcourt et al.* [2002] that this acceleration is more pronounced at
1397 Mercury than at Earth, possibly leading to energization of heavy ions up to several
1398 hundreds of eVs or a few keVs in the lobes prior to their entry into the plasma sheet.
1399 This is at variance with the energy gain up to at most a few tens of eVs expected at
1400 Earth [e.g., *Yau et al.*, 2012].

1401 In particular, in contrast to Earth, the above centrifugal acceleration may play a
1402 specific role in the escape of planetary material at Mercury; hence, a prominent
1403 impact on the net plasma supply to the Hermean magnetosphere. Indeed, at Earth,
1404 unless a short-lived compression event affects the magnetosphere [e.g., *Cladis et al.*,
1405 2000], this acceleration is weak and operates over a long time as particles travel
1406 downtail in the lobes. Ions ejected from the terrestrial ionosphere with velocities
1407 smaller than the escape speed are not sufficiently accelerated by this mechanism to
1408 overcome gravity and return toward the ionosphere according to parabolic or hopping
1409 trajectories [e.g., *Horwitz*, 1984]. Because of the pronounced curvature of the
1410 magnetic field lines in the immediate vicinity of the planet surface, a different
1411 situation is obtained at Mercury with abrupt energization of the ions immediately after
1412 ejection into the magnetosphere [*Delcourt*, 2013]. In this latter study, it was found
1413 that the numerous populations that are released at very low energies such as those due
1414 to thermal desorption are rapidly accelerated up to $\sim 2V_{E \times B}$ ($V_{E \times B}$ being the $\mathbf{E} \times \mathbf{B}$ drift
1415 speed) in a like manner to the acceleration due to a moving magnetic mirror [*Cowley*,
1416 1984]. Accordingly, instead of being trapped near the planet surface due to ejection
1417 velocities smaller than the escape speed, these ions readily overcome gravity and flow
1418 into the magnetosphere. Also, since the parallel velocity realized does not depend
1419 upon mass-to-charge ratio, all ion species are transported into a similar region of
1420 space in the pre-midnight sector of the inner magnetotail which may explain the
1421 density enhancements locally recorded by MESSENGER [*Raines et al.*, 2013].

1422 Moreover, the study of *Delcourt* [2013] suggests that the centrifugal focusing of
1423 planetary material thus obtained depends little upon the convection rate, an increase
1424 of the convection electric field magnitude (and associated $\mathbf{E} \times \mathbf{B}$ drift speed) resulting
1425 into an increase of the particle parallel speed in the same proportion.

1426 **5.2.2 Spatial nonadiabaticity in Mercury's magnetotail**

1427 Upon reaching the field reversal in the magnetotail, particles may not conserve
1428 their magnetic moment (first adiabatic invariant) because of significant field
1429 variations on the length scale of the particle Larmor radius. A parameter that is often
1430 used to characterize this nonadiabatic behavior is the parameter κ defined as the
1431 square root of the minimum field line curvature radius-to-maximum Larmor radius
1432 ratio. For $\kappa > 3$, the particle motion is adiabatic and the guiding center approximation
1433 is valid while for κ of the order of unity or below, the motion is nonadiabatic with
1434 possibly large variations of the magnetic moment. (For more details see *Seki et al.*,
1435 2015, this volume). At Earth, the transition from adiabatic to nonadiabatic regimes,
1436 viz. $\kappa \approx 1$, occurs in the mid-tail for plasma sheet ions. This region has been viewed
1437 either as the onset of prominent injections into the atmospheric loss cone and
1438 subsequent ion precipitation (leading to the Isotropy Boundary interpretation
1439 framework of *Sergeev et al.* [1993]) or as a domain of enhanced trapping (hence, the
1440 "wall" picture put forward by *Ashour-Abdalla et al.* [1992]), both pictures being valid
1441 since particles are subjected to either magnetic moment damping or enhancement
1442 [e.g., *Delcourt et al.*, 1996]. At Mercury, because of the weak intrinsic magnetic field
1443 and of the strong solar wind dynamical pressure, the magnetosphere is small and the
1444 planet occupies a much larger volume of it than at Earth. The nearly dipolar region of
1445 the inner terrestrial magnetosphere where the particle motion is essentially adiabatic is
1446 thus absent at Mercury, and it is expected that most ions behave nonadiabatically
1447 throughout the magnetotail. Computations of the adiabaticity parameter κ in model
1448 magnetospheres of Mercury actually suggest that the condition $\kappa \approx 3$ is met in the
1449 immediate vicinity of the planet. Hybrid simulations where a kinetic description is
1450 used for ions while electrons are treated as a massless fluid are thus most appropriate
1451 at Mercury [e.g., *Kallio and Janhunen*, 2003; *Travnicek et al.*, 2007; *Richer et al.*,
1452 2012].

1453 The fact that ions behave nonadiabatically in most of the hermean magnetotail
1454 is of importance for its structure and dynamics. In particular, be they of solar wind or
1455 planetary origin, ions at $\kappa < 1$ may display either quasi-trapped orbits with repeated
1456 crossings of the field reversal or Speiser-type orbits [*Speiser*, 1965] with large
1457 energization along the dawn-dusk convection electric field during meandering motion
1458 about the midplane. Such nonadiabatic behaviors that are sometimes referred to as
1459 "quasi-adiabatic" because of possible conservation of the action integral I_z [*Büchner*
1460 *and Zelenyi*, 1989], are of paramount importance since they lead to the formation of

1461 thin current sheets embedded within a thick plasma sheet. Instability of these thin
1462 current sheets can lead to local current disruption and consequent reconfiguration of
1463 the magnetic field lines [e.g., *Mitchell et al.*, 1990]. Nonadiabatic particle behaviors
1464 also lead to the formation of nongyrotropic distribution functions ; hence, significant
1465 off-diagonal terms in the plasma pressure tensor and a stress balance that does not
1466 rely on a large pressure gradient along the tail axis.

1467 As planetary ions reach the magnetotail midplane after $\mathbf{E} \times \mathbf{B}$ transport over the
1468 polar cap, they are nearly aligned with the magnetic field owing to pitch angle folding
1469 from low to high altitudes. Would their motion be adiabatic (magnetic moment
1470 conserving), these ions would return to the planet vicinity after a single crossing of
1471 the magnetotail midplane and precipitate onto the surface. Far from such a behavior,
1472 planetary ions are subjected to prominent magnetic moment scattering upon
1473 interaction with the field reversal. As a result of this isotropization and temporary
1474 trapping, and without invoking other processes such as wave-particle interactions,
1475 these ions are found to substantially contribute to the plasma sheet populations. In a
1476 quantitative study of the Na^+ circulation at Mercury, *Delcourt et al.* [2003] considered
1477 a model exosphere of neutral sodium [*Leblanc and Johnson*, 2003] and showed that
1478 this planetary material may contribute up to a few tenths of ions/cm³ to the equatorial
1479 magnetotail, this contribution depending upon phase angle along Mercury orbit. Such
1480 densities are in qualitative agreement with those reported by *Raines et al.* [2013] in
1481 their analysis of MESSENGER data. Also, assuming a cross-polar cap potential drop
1482 of 20 kV, the simulations of *Delcourt et al.* [2003] put forward times of flight from
1483 the high-latitude dayside sector to the inner plasma sheet of the order of a few minutes
1484 on the average, together with a prominent asymmetry between dawn and dusk sectors
1485 due to westward drift of the ions.

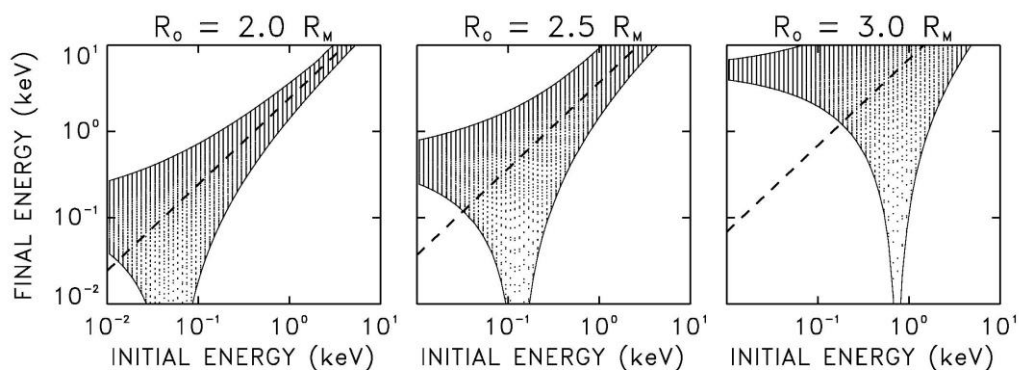
1486 During their nonadiabatic transport, Na^+ ions can be injected inside the loss
1487 cone which is much larger at Mercury than at Earth due to the weak planetary
1488 magnetic field; hence, their precipitation onto the planet surface. In the modified
1489 Luhmann-Friesen model considered by *Delcourt et al.* [2003], this ion precipitation is
1490 organized according to two narrow bands at mid-latitudes (between $\sim 30^\circ$ and $\sim 40^\circ$),
1491 the κ parameter varying from ~ 1 down to ~ 0.1 as the latitude increases. The poleward
1492 boundary of these precipitation bands is controlled by the width of the magnetotail,
1493 ions at higher latitudes (or, equivalently, at larger distances in the magnetotail)
1494 intercepting the magnetopause in the course of their duskward motion. Using results
1495 of MHD simulations, *Seki et al.* [2013] demonstrated that this overall precipitation
1496 pattern may significantly depend upon the planet surface conductivity as well as IMF
1497 orientation, the formation of a near-Mercury neutral line leading to significant
1498 downtail loss of planetary ions.

1499 **5.2.3 Temporal nonadiabaticity in Mercury's magnetotail**

1500 The nonadiabatic transport features described above in the magnetotail field
 1501 reversal result from large magnetic field variations on the length scale of the particle
 1502 Larmor radius. These features accordingly relate to spatial nonadiabaticity. In the case
 1503 of explicit temporal variations of the field on the time scale of the particle gyroperiod,
 1504 nonadiabatic features may appear as well. This latter temporal nonadiabaticity cannot
 1505 be characterized with the help of the κ parameter, and it may actually occur in regions
 1506 where $\kappa > 3$ (i.e., where the spatial adiabaticity condition is fulfilled). Such a temporal
 1507 nonadiabaticity may emerge for instance during short-lived reconfigurations of the
 1508 magnetospheric field lines. In this regard, it was shown that, at Earth, heavy ions
 1509 originating from the ionosphere such as O^+ may be subjected to prominent
 1510 nonadiabatic energization up to the hundred of keV range during substorm
 1511 dipolarization [e.g., *Delcourt, 2002*]. This energization due to the electric field
 1512 induced by the time-varying magnetic field preferentially affects O^+ ions that have
 1513 cyclotron periods comparable to the dipolarization time scale. In contrast, protons that
 1514 have smaller gyroperiods are transported adiabatically (provided that $\kappa > 3$) and
 1515 subjected to Fermi-type or betatron energization. Because of the smaller characteristic
 1516 time scales of the Mercury's environment (e.g., with a typical Dungey cycle time of
 1517 ~ 2 min as opposed to ~ 1 hour at Earth), it may be anticipated that protons will be
 1518 subjected to such a temporal nonadiabaticity during reconfigurations of the Hermean
 1519 magnetotail.

1520 Figure 22 shows the energy variations obtained for protons in the case of a 10-
 1521 second model dipolarization of the magnetic field lines in the inner magnetotail of
 1522 Mercury. In this figure, the H^+ post-dipolarization energy is shown as a function of
 1523 initial energy and for different initial gyrophases. Because the particles considered
 1524 here are equatorially trapped (i.e., 90° pitch angle at equator), no effect due to parallel
 1525 motion and spatial nonadiabaticity is to be expected.

1526



1527
 1528
 1529

Figure 22: Post-dipolarization energy versus initial energy for equatorially mirroring H^+ launched from different initial distances : (from left to right) 2, 2.5, and 3 R_M . In each panel, the various dots

1530 correspond to distinct initial gyrophases whereas the dashed line shows the final energy expected in the
1531 case of adiabatic (betatron-type) energization.

1532

1533 It is apparent from Figure 22 that protons with low initial energies are
1534 systematically energized up to a level that gradually increases with initial distance
1535 (from left to right). In particular, in the right panel of Figure 22, the low-energy
1536 protons initialized at $3 R_M$ are systematically energized up to ~ 4 keV while being
1537 transported down to $\sim 1.8 R_E$. This nonadiabatic behavior at low initial energies
1538 contrasts with that obtained at large initial energies where betatron-type energization
1539 (i.e., in proportion to the change in magnetic field magnitude) is obtained. Although
1540 short-lived fluctuations of the magnetic field that are not considered here may lead to
1541 deviations from these results, it is clearly apparent from Figure 22 that, in a like
1542 manner to O^+ at Earth, protons may be transported in a nonadiabatic manner during
1543 dipolarization events at Mercury. Under the effect of the transient induced electric
1544 field, these ions may experience energy gains significantly above that expected from
1545 the large scale convection electric field alone.

1546 Because temporal nonadiabaticity is to be expected whenever the magnetic field
1547 changes significantly on the time scale of the particle gyroperiod, it may be
1548 anticipated that ions will be transported nonadiabatically not only in the equatorial
1549 region but also at high latitudes. This follows from the short characteristic time scales
1550 at Mercury as well as from the weak intrinsic magnetic field that leads to large ion
1551 gyroperiods. An example of such behaviors is provided in Figure 23 that shows the
1552 results of Na^+ simulations during a 20-s turning of the IMF from $B_X = 0$ to $B_X = 20$ nT
1553 [Delcourt *et al.*, 2011]

1554 The leftmost panels of Figure 23 depict symmetrical Na^+ flows from the high
1555 latitude dayside sector above the polar cap as well as gradual centrifugal acceleration
1556 up to the keV range before reaching the nightside plasma sheet. On the other hand,
1557 during IMF turning (from left to right in Figure 23), it is apparent that the Na^+ average
1558 energy (bottom panels) off equator rapidly increases up to several keVs. As discussed
1559 above, this energization occurs in a nonadiabatic manner and follows from resonance
1560 between the induced electric field and the particle gyromotion. At high latitudes, such
1561 a resonance is achieved for Na^+ and Figure 23 thus suggests that IMF turning or short-
1562 lived magnetic transitions at Mercury may go together with the rapid production of
1563 heavy energetic material in the magnetospheric lobes.

1564

1565 **6 Summary**

1566
1567
1568
1569
1570
1571

Mercury's magnetosphere is dynamic and its environment is extreme. It is similar enough to allow application of terrestrial theory and approaches, yet it has differences sufficient to challenge some of them with the need for more sophistication. Mercury's intrinsic field is sufficient to stand off the solar wind, but creates a very small magnetosphere that responds dramatically to changing solar wind

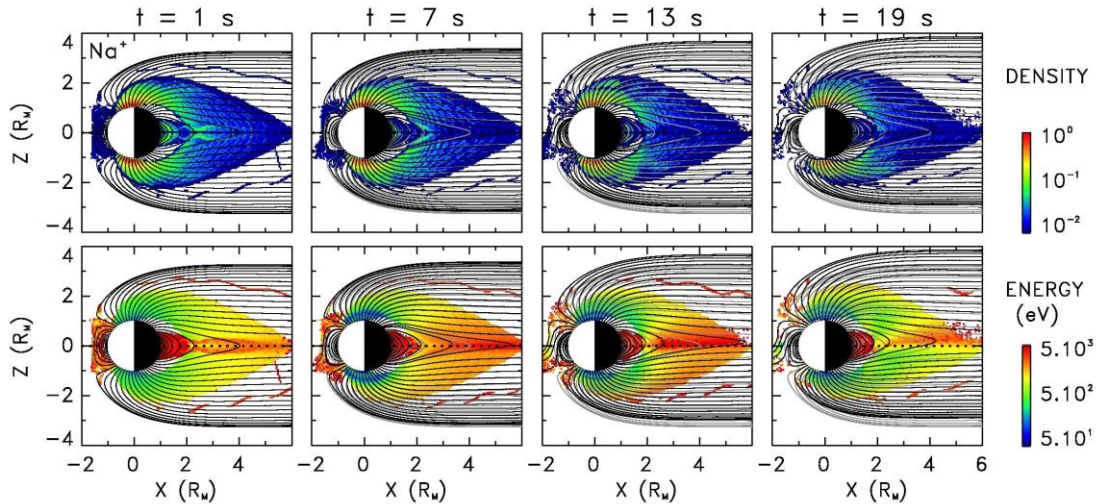


Figure 23 : (Top) Model normalized density and (bottom) average energy of Na⁺ ions in the noon-midnight meridian plane during a model IMF turning. Panels from left to right show snapshots at distinct times of the magnetic transition. Black and grey lines show the magnetic field lines at the corresponding time and in the initial configuration, respectively. Density and energy are coded according to the color scales at right. From *Delcourt et al. [2011]*.

1572
1573
1574
1575
1576
1577
1578
1579
1580
1581
1582
1583
1584
1585
1586
1587
1588
1589
1590
1591
1592
1593
1594

conditions. The main global dynamical behavior is Dungey cycle circulation but at a rate about 30 times faster than at Earth, contributing to the magnetosphere's ability to reconfigure very quickly. This convection is driven by magnetic reconnection at the dayside magnetopause, but unlike other planetary magnetospheres, the reconnection rate is independent of magnetic shear angle. As a consequence of frequent magnetopause reconnection, Mercury's magnetosphere is dominated by Dungey cycle convection.

MESSENGER measurements have unambiguously proven that Mercury's magnetosphere is populated with plasma of both solar wind and planetary origins. The magnetospheric plasma distribution is similar to Earth's, concentrated at high-latitudes in the dayside magnetospheric cusp and tail lobes as well as in the equatorial plane of the central plasma sheet in the tail. Solar wind protons are the most abundant species in those regions, followed by solar wind alpha particles and Mercury-derived Na⁺ ions (grouped with Mg⁺ and Si⁺ in observations). Two other planetary ion species have been studied, the O⁺ group and He⁺. Both are present in lower abundance than Na⁺-group ions and have not been studied in much detail. Other planetary ions with $m/q > 30$ appear in FIPS data and work is underway to identify them. In the cusp, Na⁺-group ions come from two sources: upwelling from the surface and swept in by reconnection from the vicinity of the dayside magnetopause. Plasma loss to the surface has been observed through the presence of a large loss cone of $\sim 59^\circ$ in a long-term average. In the central plasma sheet, protons dominate the number density by an order of magnitude, but Na⁺-group ions can comprise up to 50% of the mass density and 15% of the thermal pressure. Observations of Kelvin-Helmholtz waves, along the

1595 magnetopause boundary, have provided the first conclusive evidence that these
1596 planetary ions are dynamically important in Mercury's magnetosphere.

1597 The ultimate sources of planetary ions are certainly Mercury's tenuous
1598 exosphere and mineral surface, but their relative contributions have not yet been
1599 determined conclusively. Lacking a collisional ionosphere, Mercury's magnetosphere
1600 and exosphere are co-located, making their coupling via source and sink processes
1601 very direct. Global modeling of the exosphere is quite sophisticated, including all of
1602 these processes as well as effects related to surface reservoir and Mercury's extreme
1603 seasonal differences. Ground-based observations of the exosphere have been used
1604 extensively to constrain these models, though constraint with MESSENGER
1605 observations is just reaching maturity. Some of these models include generation and
1606 test particle tracing of planetary ions, but work to compare these quantitatively with
1607 MESSENGER plasma ion observations is only beginning.

1608 **7 Open Questions**

1609 Despite understanding many aspects of plasma sources in Mercury's
1610 magnetosphere, there are several top-level questions that still remain.

1611 **What is the role of the solar wind in generating the exosphere and**
1612 **populating the magnetosphere with planetary ions?** The solar wind is expected to
1613 act as a highly variable exospheric (and likewise magnetospheric) source via
1614 precipitation and ion sputtering. The search for concrete observational evidence of
1615 this effect is still on going. Precipitation of solar wind protons and upwelling surface
1616 ions has been observed *in situ* by MESSENGER but a definitive cause and effect
1617 relationship has not been established. One complication is the fact that newly created
1618 ions, from all processes involved, have peak energies of just a few eV and to be
1619 observed they must be accelerated above FIPS energy minimum, which has been 46
1620 eV for much of the MESSENGER mission. The limit was lowered in August 2014,
1621 down to effectively the spacecraft potential (10s of eV) but those measurements have
1622 not yet been analysed in detail. Ground-based exospheric observations have shown
1623 variability on the timescale of hours, consistent with solar wind generation of
1624 exospheric neutrals, but have not been correlated *in situ* solar wind observations.
1625 Finally, confirmation with MESSENGER UVVS observations has proven elusive,
1626 due partly to operational constraints that have allowed for only very limited UVVS
1627 observations in the magnetospheric cusps where variability due to solar wind should
1628 be at a maximum. The frequency of these observations increased toward the end of
1629 the mission so the nature of this relationship may still be established from
1630 MESSENGER data. In any case, the BepiColombo Mercury Planetary Orbiter will
1631 measure these neutral atoms directly with the Strofio instrument, a low energy neutral
1632 gas mass spectrometer of the SERENA particle package [Orsini *et al.* 2010].
1633 Working with the particles and fields instrument on the Mercury Magnetospheric
1634 Orbiter, this correlation should be established in a straightforward way.

1635 **In what proportions to other exogenic processes contribute and how do**
1636 **they vary with season?** Despite significant progress in tying observations to physical
1637 processes and the creation of realistic global models, no quantitative, consensus
1638 global picture of exosphere generation has emerged. One problem is that the system
1639 is under-constrained. The relative contributions to the exosphere of the many source
1640 and sink processes is likely different for each exospheric neutral species, and may be
1641 a function of Mercury season and even location on the surface. Exospheric
1642 composition depends on details of surface composition at significantly higher

1643 resolution than available. It may depend on other inputs such as micrometeoroid
1644 impact rates or traversal of the interplanetary dust disk, which are at best difficult to
1645 measure. On-going work combining the available measurements with self-consistent
1646 exosphere/magnetosphere models will likely continue to improve understanding, as
1647 will additional measurements from the two-spacecraft BepiColombo mission.
1648 However it is possible that there are just too many free parameters to adequately
1649 constrain with the relatively sparse measurements that are possible at Mercury.

1650 **Do heavy planetary ions make an important contribution to**
1651 **magnetospheric dynamics and if so, how?** MESSENGER observations have
1652 shown that planetary ions change the scale of Kelvin-Helmholtz waves along
1653 Mercury's tail magnetopause. This dynamical contribution could have significant
1654 effect on plasma entry through this process. Observations in Mercury's central
1655 plasma sheet have shown that they can make up a significant portion of the pressure
1656 and dominate the mass density. This certainly sets the stage for participating in
1657 magnetospheric dynamics. That said, planetary ions have not yet been shown to
1658 influence plasmoids in the magnetotail or act as more than a tracer of plasma flowing
1659 through Mercury's northern magnetospheric cusp on newly reconnected field lines.
1660 Further analysis of MESSENGER data will likely shed more light on this question.
1661 However, the BepiColombo mission, with two spacecraft, more complete particles
1662 and fields instrumentation and the larger fields of view possible without sunshade
1663 obstructions, is well-poised to address this very complex question.

1664 **Does surface impact and sputtering by magnetospheric ions constitute a**
1665 **significant source to Mercury's exosphere and magnetosphere?** Tracing protons
1666 on closed field lines in the magnetotail has shown losses that should be indicative of
1667 impact on the planet's surface. They have nearly the same energy as precipitating
1668 protons in the cusp and should, therefore, cause sputtering of ions and neutral atoms.
1669 Protons traveling toward the surface in closed field regions have not been observed,
1670 though MESSENGER's orbit and orientation is not well-suited to observing this
1671 precipitation. MHD and Hybrid simulations show this behavior, but as of yet,
1672 determining the contribution to the exosphere and magnetosphere of this process from
1673 simulations has not converged to clear values. In addition to protons, planetary ions
1674 such as Na⁺ present in the magnetotail should behave similarly. Their higher
1675 energies, up to 10 keV, could make their precipitation contribute more than would be
1676 expected by relative number densities alone.

1677 A lot has been learned about Mercury so far, from Mariner 10, ground
1678 observations, MESSENGER and modeling, but there is much left to do. Analysis of
1679 MESSENGER orbital data is really just in the early stages; new results should
1680 continue to come out for years to come. In less than a decade after the end of the
1681 MESSENGER mission, BepiColombo will arrive to enable a new and potentially
1682 more detailed study of the closest planet to the Sun.

1683 **8 Compliance with Ethical Standards**

1684 This article is in compliance with the ethical standards laid out by the COPE
1685 guidelines. There are no conflicts of interest and no human or animal subjects were
1686 used in this work. All co-authors have contributed to this manuscript and have given
1687 their consent to its submission.

1688
1689
1690
1691
1692
1693
1694
1695
1696
1697
1698
1699
1700
1701
1702
1703
1704
1705
1706
1707
1708
1709
1710
1711
1712
1713
1714
1715
1716
1717
1718
1719
1720
1721
1722
1723
1724
1725
1726
1727
1728
1729
1730
1731
1732
1733
1734
1735
1736
1737

9 References

- Alexeev, I. I., E. S. Belenkaya, J. A. Slavin, H. Korth, B. J. Anderson, D. N. Baker, S. A. Boardsen, C. L. Johnson, M. E. Purucker, M. Sarantos, and S. C. Solomon (2010), Mercury's magnetospheric magnetic field after the first two MESSENGER flybys, *Icarus*, *209*, 23–39.
- Anderson, B. J., M. H. Acuna, D. A. Lohr, J. Scheifele, A. Raval, H. Korth, and J. A. Slavin (2007), The Magnetometer instrument on MESSENGER, *Space Sci. Rev.*, *131*, 417–450.
- Anderson, B. J., et al. (2011), The global magnetic field of Mercury from MESSENGER orbital observations, *Science*, *333*, 1859–1862, doi:10.1126/science.1211001.
- Anderson, B. J., C. L. Johnson, H. Korth, R. M. Winslow, J. E. Borovsky, M. E. Purucker, J. A. Slavin, S. C. Solomon, M. T. Zuber, and R. L. McNutt Jr. (2012), Low-degree structure in Mercury's planetary magnetic field, *J. Geophys. Res.*, *117*, E00L12, doi:10.1029/2012JE004159.
- Anderson, B. J., C. L. Johnson, H. Korth, J. A. Slavin, R. M. Winslow, R. J. Phillips, R. L. McNutt Jr., and S. C. Solomon (2014), Steady-state field-aligned currents at Mercury, *Geophys. Res. Lett.*, *41*, 7444–7452, doi:10.1002/2014GL061677.
- Andrews, G. B., et al. (2007), The Energetic Particle and Plasma Spectrometer instrument on the MESSENGER spacecraft, *Space Sci. Rev.*, *131*, 523–556, doi:10.1007/s11214-007-9272-5.
- Angelopoulos, V., C. F. Kennel, F. V. Coroniti, R. Pellat, M. G. Kivelson, R. J. Walker, C. T. Russell, W. Baumjohann, W. C. Feldman, and J. T. Gosling (1994), Statistical characteristics of bursty bulk flow events, *J. Geophys. Res.*, *99*, 21,257–21,280.
- Armstrong, T. P., S. M. Krimigis, and L. J. Lanzerotti (1975), A reinterpretation of the reported energetic particle fluxes in the vicinity of Mercury, *J. Geophys. Res.*, *80*, 4015–4017, doi:10.1029/JA080i028p04015.
- Ashour-Abdalla, M., L. M. Zelenyi, J.-M. Bosqued, V. Perroomian, Z. Whang, D. Schriver, and R. L. Richard (1992), The formation of the wall region: Consequences in the near-Earth magnetotail, *Geophys. Res. Lett.*, *19*, 1739.
- Ashour-Abdalla, M., M. El-Alaoui, M. L. Goldstein, M. Zhou, D. Schriver, R. Richard, R. Walker, M. G. Kivelson, and K. J. Hwang (2011), Observations and simulations of non-local acceleration of electrons in magnetotail magnetic reconnection events, *Nature Phys.*, *7*, 360–365.
- Baker, D. N., J. A. Simpson, and J. H. Eraker (1986), A model of impulsive acceleration and transport of energetic particles in Mercury's magnetosphere, *J. Geophys. Res.*, *91*, 8742–8748.
- Baker, D. N., T. I. Pulkkinen, V. Angelopoulos, W. Baumjohann, and R. L. McPherron, (1996), Neutral line model of substorms: Past results and present view, *J. Geophys. Res.*, *101*, 12,975–13,010.
- Baker, D. N., G. Poh, D. Odstrcil, C. N. Arge, M. Benna, C. L. Johnson, H. Korth, D. J. Gershman, G. C. Ho, W. E. McClintock, T. A. Cassidy, A. Merkel, J. M. Raines, D. Schriver, J. A. Slavin, J. A., and S. C. Solomon (2013), Solar wind forcing at Mercury: WSA-ENLIL model results, *J. Geophys. Res. Space Physics*, *118*, 45–57.
- Baumjohann, W., and G. Paschmann (1989), Determination of the polytropic index in the plasma sheet, *Geophys. Res. Lett.*, *16*, 295–298.
- Behrisch, R., and W. Eckstein (2007), Sputtering by particle bombardment: experiments and computer calculations from threshold to MeV energies, Springer, 110.

1738 Benkhoff, J., J. van Casteren, H. Hayakawa, M. Fujimoto, H. Laakso, M. Novara, P.
1739 Ferri, H. R. Middleton, and R. Ziethe (2010), BepiColombo-Comprehensive
1740 exploration of Mercury: Mission overview and science goals, *Planet. Space Sci.*,
1741 58, 2–20.

1742 Benna, M., et al., (2010), Modeling of the magnetosphere of Mercury at the time of
1743 the first MESSENGER flyby, *Icarus*, 209, 3–10, doi:10.1016/j.icarus.2009.11.036.

1744 Benninghoven, A. (1975), Developments in secondary ion mass spectroscopy and
1745 applications to surface studies, *Surface Science*, 53, 596-625, doi:
1746 10.1016/0039-6028(75)90158-2.

1747 Bida, T. A., R. M. Killen, and T. H. Morgan (2000), Discovery of calcium in
1748 Mercury's atmosphere, *Nature*, 404, 159–161.

1749 Boardsen, S. A., B. J. Anderson, M. H. Acuña, J. A. Slavin, H. Korth, and S. C.
1750 Solomon (2009), Narrow-band ultra-low-frequency wave observations by
1751 MESSENGER during its January 2008 flyby through Mercury's magnetosphere,
1752 *Geophys. Res. Lett.*, 36, L01104, doi:10.1029/2008GL036034.

1753 Boardsen, S. A., T. Sundberg, J. A. Slavin, B. J. Anderson, H. Korth, S. C. Solomon,
1754 and L. G. Blomberg (2010), Observations of Kelvin-Helmholtz waves along the
1755 dusk-side boundary of Mercury's magnetosphere during MESSENGER's third
1756 flyby, *Geophys. Res. Lett.*, 37, L12101, doi:10.1029/2010GL043606.

1757 Boardsen, S. A., J. A. Slavin, B. J. Anderson, H. Korth, D. Schriver, and S. C.
1758 Solomon (2012), Survey of coherent ~1 Hz waves in Mercury's inner
1759 magnetosphere from MESSENGER observations, *J. Geophys. Res.*, 117, A00M05,
1760 doi:10.1029/2012JA017822.

1761 Borin, P., M. Bruno, G. Cremonese, F. Marzari (2010), Estimate of the neutral atoms'
1762 contribution to the Mercury exosphere caused by a new flux of micrometeoroids,
1763 *Astronom. and Astrophys.*, 517, A89.

1764 Broadfoot, A. L., S. Kumar, and M. J. S. Belton (1974), Mercury's atmosphere from
1765 Mariner 10: Preliminary results, *Science*, 185, 166–169.

1766 Broadfoot, A. L., D. E. Shemansky, and S. Kumar (1976), Mariner 10: Mercury
1767 atmosphere. *Geophys. Res. Lett.*, 3, 577–580.

1768 Broadfoot, A. L., S. S. Clapp, and F. E. Stuart (1977), Mariner 10 ultraviolet
1769 spectrometer: airglow experiment, *Space Sci. Instrum.*, 3, 199–208.

1770 Bruno, M., G. Cremonese, and S. Marchi (2007), Neutral sodium atoms release from
1771 the surfaces of the Moon and Mercury induced by meteoroid impacts, *Planet.*
1772 *Space Sci.* 55, 1494–1501.

1773 Büchner, J., and L. M. Zelenyi (1989), Regular and chaotic charged particle motion in
1774 magnetotaillike field reversals: 1. Basic theory of trapped motion, *J. Geophys.*
1775 *Res.*, 94, 11,821–11,842, doi:10.1029/JA094iA09p11821.

1776 Burger, M. H., R. M. Killen, R. J. Vervack, E. T. Bradley, W. E. McClintock, M.
1777 Sarantos, M. Benna, and N. Mouawad (2010), Monte Carlo modeling of sodium in
1778 Mercury's exosphere during the first two MESSENGER flybys, *Icarus*, 209, 63–
1779 74, doi: 10.1016/j.icarus.2010.05.007.

1780 Burger, M. H., R. M. Killen, W. E. McClintock, R. J. Vervack Jr., A. W. Merkel, A.
1781 L. Sprague, and M. Sarantos (2012), Modeling MESSENGER observations of
1782 calcium in Mercury's exosphere, *J. Geophys. Res.*, 117, E00L11,
1783 doi:10.1029/2012JE004158.

1784 Burger, M. H., R. M. Killen, W. E. McClintock, A. W. Merkel, R. J. Vervack, Jr., T.
1785 A. Cassidy, and M. Sarantos (2014), Seasonal variations in Mercury's dayside
1786 calcium exosphere, *Icarus*, 238, 51–58.

1787 Burlaga, L. F. (2001), Magnetic fields and plasmas in the inner heliosphere: Helios
1788 results, *Planet. Space Sci.*, *49*, 1619–1627.

1789 Caan, M. N., R. L. McPherron, and C. T. Russell (1973), Solar wind and substorm-
1790 related changes in lobes of geomagnetic tail, *J. Geophys. Res.*, *78*, 8087–8096.

1791 Cassidy, T. A., A. W. Merkel, M. H. Burger, M. Sarantos, R. M. Killen, W. E.
1792 McClintock, and R. J. Vervack (2015), Mercury's seasonal sodium exosphere:
1793 MESSENGER orbital observations, *Icarus*, *248*, 547-559, doi:
1794 10.1016/j.icarus.2014.10.037.

1795 Christon, S. P., J. Feynman, and J. A. Slavin, Dynamic substorm injections – Similar
1796 magnetospheric phenomena at Earth and Mercury, in *Magnetotail Physics*, edited
1797 by A. T. Y. Lui, pp. 393–400, Johns Hopkins Univ. Press, Baltimore, MD, 1987.

1798 Cintala, M. J. (1992), Impact induced thermal effects in the lunar and Mercurian
1799 regoliths, *J. Geophys. Res.*, *97*, 947–973.

1800 Cladis, J. B. (1986), Parallel acceleration and transport of ions from polar ionosphere
1801 to plasma sheet, *Geophys. Res. Lett.*, *13*, 893.

1802 Cladis, J. B., H. L. Collin, O. W. Lennartsson, T. E. Moore, W. K. Peterson, and C. T.
1803 Russell (2000), Observations of centrifugal acceleration during compression of
1804 magnetosphere, *Geophys. Res. Lett.*, *27*, 915.

1805 Cowley, S. W. H. (1982), The causes of convection in the Earth's magnetosphere: A
1806 review of developments during the IMS, *J. Geophys. Res.*, *20*, 531 – 565.

1807 Cowley, S. W. H., The distant geomagnetic tail in theory and observation, *AGU*
1808 *Monograph on "Magnetic reconnection in space and laboratory plasmas"*, vol. 30,
1809 p. 228, 1984.

1810 Cremonese, G., M. Bruno, V. Mangano, S. Marchi, and A. Milillo (2005), Release of
1811 neutral sodium atoms from the surface of Mercury induced by meteoroid impacts,
1812 *Icarus*, *177*, 122–128.

1813 Delcourt, D. C. (2002), Particle acceleration by inductive electric fields in the inner
1814 magnetosphere, *J. Atm. Solar Ter. Phys.*, *64*, 551.

1815 Delcourt, D. C. (2013), On the supply of heavy planetary material to the magnetotail
1816 of Mercury, *Ann. Geophys.*, *31*, 1673.

1817 Delcourt, D. C., T. E. Moore, and M.-C. Fok (2011), On the effect of IMF turning on
1818 ion dynamics at Mercury, *Ann. Geophys.*, *29*, 987.

1819 Delcourt, D. C., J.-A. Sauvaud, R. F. Martin Jr., and T. E. Moore (1996), On the
1820 nonadiabatic precipitation of ions from the near-Earth plasma sheet, *J. Geophys.*
1821 *Res.*, *101*, 17,409.

1822 Delcourt, D. C., T. E. Moore, S. Orsini, A. Millilo, and J.-A. Sauvaud (2002),
1823 Centrifugal acceleration of ions near Mercury, *Geophys. Res. Lett.*, *29*, 32, doi:
1824 10.1029/2001GL013829.

1825 Delcourt, D. C., S. Grimald, F. Leblanc, J.-J. Berthelier, A. Millilo, A. Mura, S.
1826 Orsini, and T. E. Moore (2003), A quantitative model of the planetary Na+
1827 contribution to Mercury's magnetosphere, *Ann. Geophys.*, *21*, 1723–1736,
1828 doi:10.5194/angeo-21-1723-2003.

1829 Delcourt, D. C., K. Seki, N. Terada, and T. E. Moore (2012), Centrifugally stimulated
1830 exospheric ion escape at Mercury, *Geophys. Res. Lett.*, *39*, L22105,
1831 doi:10.1029/2012GL054085.

1832 DiBraccio, G. A., J. A. Slavin, S. A. Boardsen, B. J. Anderson, H. Korth, T. H.
1833 Zurbuchen, J. M. Raines, D. N. Baker, R. L. McNutt Jr., and S. C. Solomon
1834 (2013), MESSENGER observations of magnetopause structure and dynamics at
1835 Mercury, *J. Geophys. Res. Space Physics*, *118*, 997–1008, doi:10.1002/jgra.50123.

1836 DiBraccio, G. A., J. A. Slavin, S. M. Imber, D. J. Gershman, J. M. Raines, C. M.
1837 Jackman, S. A. Boardsen, B. J. Anderson, H. Korth, T. H. Zurbuchen, R. L.
1838 McNutt, Jr., and S. C. Solomon (2014), MESSENGER observations of flux ropes
1839 in Mercury's magnetotail, *Planet. Space Sci.*, doi:10.1016/j.pss.2014.12.016.

1840 DiBraccio, G. A., J. A. Slavin, J. M. Raines, D. J. Gershman, P. J. Tracy, S. A.
1841 Boardsen, T. H. Zurbuchen, B. J. Anderson, H. Korth, R. L. McNutt Jr., and S. C.
1842 Solomon, First observations of Mercury's plasma mantle as seen by
1843 MESSENGER, in prep.

1844 Domingue, D. L., A. L. Sprague, and D. M. Hunten, (1997), Dependence of
1845 Mercurian atmospheric column abundance estimations on surface-reflectance
1846 modeling, *Icarus*, 128, 75–82.

1847 Domingue, D. L., P. L. Koehn, R. M. Killen, A. L. Sprague, M. Sarantos, A. F.
1848 Cheng, E. T. Bradley, and W. E. McClintock (2007), Mercury's atmosphere: A
1849 surface-bounded exosphere, *Space Sci. Rev.*, 131, 161–186.

1850 Doressoundiram, A., F. Leblanc, C. Foellmi, and S. Erard (2009), Metallic species in
1851 Mercury's exosphere: EMMI/New technology telescope observations, *Astron. J.*,
1852 137, 3859–3863.

1853 Dungey, J. W. (1961), Interplanetary magnetic field and the auroral zones, *Phys. Rev.*
1854 *Lett.*, 6, 47–48, doi:10.1103/PhysRevLett.6.47.

1855 Elphic, R. C., H. O. Funsten, B. L. Barraclough, D. J. McComas, M. T. Paffet, D. T.
1856 Vaniman, and G. Heiken (1991), Lunar surface composition and solar wind-
1857 induced secondary ion mass spectrometry, *Geophys. Res. Lett.*, 18, 2165–2168,
1858 doi:10.1029/91GL02669.

1859 Eraker, J. H., and J. A. Simpson (1986), Acceleration of charged particles in
1860 Mercury's magnetosphere, *J. Geophys. Res.*, 91, 9973–9993,
1861 doi:10.1029/JA091iA09p09973.

1862 Fairfield, D. H. (1971), Average and unusual locations for the Earth's magnetopause
1863 and bow shock, *J. Geophys. Res.*, 76, 6700–6716, doi:10.1029/JA076i028p06700.

1864 Farrell, W. M., J. S. Halekas, R. M. Killen, G. T. Delory, N. Gross, L. V. Bleacher, D.
1865 Krauss-Varben, P. Travnicek, D. Hurley, T. J. Stubbs, M. I. Zimmerman, and T. L.
1866 Jackson (2012), Solar-Storm/Lunar Atmosphere Model (SSLAM): An overview of
1867 the effort and description of the driving storm environment, *J. Geophys. Res.*, 117,
1868 E00K04, doi:10.1029/2012JE004070.

1869 Fjelbo, G., A. Kliore, D. Sweetnam, P. Esposito, B. Seidel, and T. Howard (1976),
1870 The occultation of Mariner 10 by Mercury, *Icarus*, 29, 407–415,
1871 doi:10.1016/0019-1035(76)90063-4.

1872 Gershman, D. J., T. H. Zurbuchen, L. A. Fisk, J. A. Gilbert, J. M. Raines, B. J.
1873 Anderson, C. W. Smith, H. Korth, and S. C. Solomon (2012), Solar wind alpha
1874 particles and heavy ions in the inner heliosphere observed with MESSENGER, *J.*
1875 *Geophys. Res.*, 117, A00M02, doi:10.1029/2012JA017829.

1876 Gershman, D. J., J. A. Slavin, J. M. Raines, T. H. Zurbuchen, B. J. Anderson, H.
1877 Korth, D. N. Baker, and S. C. Solomon (2013), Magnetic flux pileup and plasma
1878 depletion in Mercury's subsolar magnetosheath, *J. Geophys. Res.*, 118,
1879 doi:10.1002/2013JA019244.

1880 Gershman, D. J., J. A. Slavin, J. M. Raines, T. H. Zurbuchen, B. J. Anderson, H.
1881 Korth, D. N. Baker, and S. C. Solomon (2014), Ion kinetic properties in Mercury's
1882 premidnight plasma sheet, *Geophys. Res. Lett.*, 41, 5740–5747,
1883 doi:10.1002/2014GL060468.

1884 Gershman, D. J., J. M. Raines, J. A. Slavin, T. H. Zurbuchen, T. Sundberg, S. A.
1885 Boardsen, B. J. Anderson, H. Korth, and S. C. Solomon, MESSENGER

1886 observations of multi-scale Kelvin-Helmholtz vortices at Mercury, *J. Geophys.*
1887 *Res. Space Physics*, in revision.

1888 Glassmeier, K.-H., J. Grosser, U. Auster, D. Constantinescu, Y. Narita, and S.
1889 Stellmach (2007), Electromagnetic induction effects and dynamo action in the
1890 Hermean system, *Space Sci. Rev.*, *132*, 511–527, doi:10.1007/s11214-007-9244-9.

1891 Hapke, B. (1981), Bidirectional reflectance spectroscopy: 1. Theory, *J. Geophys. Res.*,
1892 *86*, 3039–3054.

1893 Hapke, B. (1984), Bidirectional reflectance spectroscopy: 3. Correction for
1894 macroscopic roughness, *Icarus*, *59*, 41–59.

1895 Hapke, B. (1986), Bidirectional reflectance spectroscopy: 4. The extinction
1896 coefficient and the opposition effect, *Icarus*, *67*, 264–280.

1897 Hesse, M. and Kivelson, M. G. (1998), The Formation and Structure of Flux Ropes in
1898 the Magnetotail, in *New Perspectives on the Earth's Magnetotail* (eds A. Nishida,
1899 D.N. Baker and S.W.H. Cowley), American Geophysical Union, Washington, D.
1900 C., doi:10.1029/GM105p0139

1901 Hidalgo, M. A., C. Cid, A. F. Vinas, and J. Sequeiros (2002a), A non-force-free
1902 approach to the topology of magnetic clouds in the solar wind, *J. Geophys. Res.*,
1903 *107*, 1002, doi:10.1029/2001JA900100.

1904 Hidalgo, M. A., T. Nieves-Chinchilla, and C. Cid (2002b), Elliptical cross-section
1905 model for the magnetic topology of magnetic clouds, *Geophys. Res. Lett.*, *29*,
1906 1637, doi:10.1029/2001GL013875.

1907 Hill, T. W., A. J. Dessler, and R. A. Wolf (1976), Mercury and Mars: The role of
1908 ionospheric conductivity in the acceleration of magnetospheric particles, *Geophys.*
1909 *Res. Lett.*, *3*, 429–432, doi:10.1029/GL003i008p00429.

1910 Ho, G. C., S. M. Krimigis, R. E. Gold, D. N. Baker, B. J. Anderson, H. Korth, J. A.
1911 Slavin, R. L. McNutt Jr., R. M. Winslow, and S. C. Solomon (2012), Spatial
1912 distribution and spectral characteristics of energetic electrons in Mercury's
1913 magnetosphere, *J. Geophys. Res.*, *117*, A00M04, doi:10.1029/2012JA017983.

1914 Hones, E. W., J. Birn, D. N. Baker, S. J. Bame, W. C. Feldman, D. J. McComas, R. D.
1915 Zwickl, J. A. Slavin, E. J. Smith, and B. T. Tsurutani (1984), Detailed examination
1916 of a plasmoid in the distant magnetotail with ISEE-3, *Geophys. Res. Lett.*, *11*,
1917 1046–1049.

1918 Hood, L. L., and G. Schubert (1979), Inhibition of solar wind impingement on
1919 Mercury by planetary induction currents, *J. Geophys. Res.* *84*, 2641–2647.

1920 Horwitz, J. L. (1984), Features of ion trajectories in the polar magnetosphere,
1921 *Geophys. Res. Lett.*, *11*, 1111.

1922 Huang, C.-S., A. D. DeJong, and X. Cai (2009), Magnetic flux in the magnetotail and
1923 polar cap during sawteeth, isolated substorms, and steady magnetospheric
1924 convection events, *J. Geophys. Res.*, *114*, A07202, doi:10.1029/2009JA014232.

1925 Huebner, W. F., J. J. Keady, and S. P. Lyon (1992), Solar photo rates for planetary
1926 atmospheres and atmospheric pollutants, *Astrophys. Space Sci.*, *195*, 1–289.

1927 Hunten, D. M., T. H. Morgan, and D. E. Shemansky (1988), The Mercury
1928 atmosphere, in *Mercury*, edited by F. Vilas, C. R. Chapman, and M. S. Matthews,
1929 pp. 562 – 612, Univ. of Ariz. Press, Tucson.

1930 Ieda, A., S. Machida, T. Mukai, Y. Saito, T. Yamamoto, A. Nishida, T. Terasawa, and
1931 S. Kokubun (1998), Statistical analysis of the plasmoid evolution with Geotail
1932 observations, *J. Geophys. Res.*, *103*, 4453–4465.

1933 Imber, S. M., J. A. Slavin, H. U. Auster, and V. Angelopoulos (2011), A THEMIS
1934 survey of flux ropes and traveling compression regions: Location of the near-Earth

1935 reconnection site during solar minimum, *J. Geophys. Res.*, *116*, A02201,
1936 doi:10.1029/2010JA016026.

1937 Imber, S. M., J. A. Slavin, S. A. Boardsen, B. J. Anderson, H. Korth, R. L. McNutt Jr.
1938 and S. C. Solomon (2014), MESSENGER observations of large dayside flux
1939 transfer events: Do they drive Mercury's substorm cycle?, *J. Geophys. Res Space*
1940 *Physics*, *119*, 5613–5623, doi:10.1002/2014JA019884.

1941 Ip, W. H. and A. Kopp (2002), MHD simulations of the solar wind interaction with
1942 Mercury, *J. Geophys. Res.*, *107*, 1348, doi:10.1029/2001JA009171.

1943 Jia, X., J. A. Slavin, T. I. Gombosi, L. Daldorff, and G. Toth (2013), Global MHD
1944 simulations of Mercury's interaction with the solar wind: Influence of the
1945 planetary conducting core on the magnetospheric interaction, AGU Fall Meeting
1946 Abstracts, A2139- doi:

1947 Johnson, R. E. and R. Baragiola (1991), Lunar surface: Sputtering and secondary ion
1948 mass spectrometry, *Geophys. Res. Lett.*, *18*, 2169–2172.

1949 Kabin, K., T. I. Gombosi, D. L. DeZeeuw, and K. G. Powell (2000), Interaction of
1950 Mercury with the solar wind, *Icarus*, *143*, 397–406.

1951 Kallio, E., and P. Janhunen (2003), Modelling the solar wind interaction with
1952 Mercury by a quasi-neutral hybrid model, *Ann. Geophys.*, *21*, 2133.

1953 Kameda, S., I. Yoshikawa, M. Kagitani, and S. Okano (2009), Interplanetary dust
1954 distribution and temporal variability of Mercury's atmospheric Na, *Geophys. Res.*
1955 *Lett.*, *36*, L15201, doi:10.1029/2009GL039036.

1956 Kidder, A., R. M. Winglee, and E. M. Harnett (2008), Erosion of the dayside
1957 magnetosphere at Mercury in association with ion outflows and flux rope
1958 generation, *J. Geophys. Res.*, *113*, A09223, doi:10.1029/2008JA013038.

1959 Killen, R. M. and W. H. Ip (1999), The surface-bounded atmospheres of mercury and
1960 the moon, *Rev. Geophys.*, *37*, 361–406.

1961 Killen, R. M. and J. M. Hahn (2015), Impact vaporization as a possible source of
1962 Mercury's calcium exosphere, *Icarus*, *250*, 230-237, doi:
1963 10.1016/j.icarus.2014.11.035.

1964 Killen, R. M., A. E. Potter, P. Reiff, M. Sarantos, B. V. Jackson, P. Hick, B. Giles
1965 (2001), Evidence for space weather at Mercury, *J. Geophys. Res.*, *106*, 20,509–
1966 20,525.

1967 Killen, R. M., M. Sarantos, A. E. Potter, and P. Reiff (2004), Source rates and ion
1968 recycling rates for Na and K in Mercury's atmosphere, *Icarus*, *171*, 1–19.

1969 Killen, R., G. Cremonese, H. Lammer, S. Orsini, A. E. Potter, A. L. Sprague, P.
1970 Wurz, M. Khodachenko, H. I. M. Lichtenegger, A. Milillo, and A. Mura (2007),
1971 Processes that Promote and Deplete the Exosphere of Mercury, *Space Sci. Rev.*
1972 *132*, 433–509.

1973 Killen, R., D. Shemansky, and N. Mouawad (2009), Expected emission from
1974 Mercury's exospheric species, and their ultraviolet-visible signatures, *Astrophys. J.*
1975 *Suppl.*, *181*, 351–359.

1976 Kivelson, M. G. and A. J. Ridley (2008), Saturation of the polar cap potential:
1977 Inference from Alfvén wing arguments, *J. Geophys. Res.*, *113*, A05214,
1978 doi:10.1029/2007JA012302.

1979 Korth, H., B. J. Anderson, J. M. Raines, J. A. Slavin, T. H. Zurbuchen, C. L.
1980 Johnson, M. E. Purucker, R. M. Winslow, S. C. Solomon, and R. L. McNutt Jr.
1981 (2011), Plasma pressure in Mercury's equatorial magnetosphere derived from
1982 MESSENGER Magnetometer observations, *Geophys. Res. Lett.*, *38*, L22201-
1983 doi: 10.1029/2011GL049451.

- 1984 Korth, H., B. J. Anderson, D. J. Gershman, J. M. Raines, J. A. Slavin, T. H.
1985 Zurbuchen, S. C. Solomon, and R. L. McNutt Jr. (2014), Plasma distribution in
1986 Mercury's magnetosphere derived from MESSENGER Magnetometer and Fast
1987 Imaging Plasma Spectrometer observations, *J. Geophys. Res. Space Physics*, *119*,
1988 2917–2932, doi:10.1002/2013JA019567.
- 1989 Kuznetsova, M. M., M. Hesse, L. Rastätter, A. Taktakishvili, G. Toth, D. L.
1990 DeZeeuw, A. Ridley, and T. I. Gombosi (2007), Multiscale modeling of
1991 magnetospheric reconnection, *J. Geophys. Res.*, *112*, A10210,
1992 doi:10.1029/2007JA012316.
- 1993 Lammer, H., P. Wurz, M. R. Patel, R. M. Killen, C. Kolb, S. Massetti, S. Orsini, and
1994 A. Milillo (2003), The variability of Mercury's exosphere by particle and radiation
1995 induced surface release processes, *Icarus*, *166*, 238–247.
- 1996 Lavraud, B., H. Rème, M. W. Dunlop, J.-M. Bosqued, I. Dandouras, J.-A. Sauvaud,
1997 A. Keiling, T. D. Phan, R. Lundin, P. J. Cargill, C. P. Escoubet, C. W. Carlson, J.
1998 P. MacFadden, G. K. Parks, E. Moebius, L. M. Kistler, E. Amata, M.-B.
1999 Bavassano-Cattaneo, A. Korth, B. Klecker, and A. Balogh (2005), Cluster observes
2000 the high-altitude cusp region, *Surv. Geophys.*, *26*, 135–175, doi:10.1007/s10712-
2001 005-1875-3.
- 2002 Leblanc, F., and R. E. Johnson (2003), Mercury's sodium exosphere, *Icarus*, *164*,
2003 261–281, doi:10.1016/S0019-1035(03)00147-7.
- 2004 Leblanc, F., and R. E. Johnson (2010), Mercury exosphere I. Global circulation model
2005 of its sodium component, *Icarus*, *209*, 280–300.
- 2006 Leblanc, F. and J. Y. Chaufray (2011), Mercury and Moon He exospheres: Analysis
2007 and modeling, *Icarus*, *216*, 551–559.
- 2008 Leblanc, F., E. Chassefiere, R. E. Johnson, D. M. Hunten, E. Kallio, D. C. Delcourt,
2009 R. M. Killen, J. G. Luhmann, A. E. Potter, A. Jambon, G. Cremonese, M.
2010 Mendillo, N. Yan, A. L. Sprague (2007), Mercury's exosphere origins and
2011 relations to its magnetosphere and surface, *Planet. Space Sci.*, *55*, 1069–1092.
- 2012 Leblanc, F., A. Doressoundiram, N. Schneider, V. Mangano, A. L. Ariste, C. Lemen,
2013 B. Gelly, C. Barbieri, G. Cremonese, (2008), High latitude peaks in Mercury's
2014 sodium exosphere: Spectral signature using THEMIS solar telescope, *Geophys.*
2015 *Res. Lett.*, *35*, L18204, doi:10.1029/2008GL035322.
- 2016 Leblanc, F., A. Doressoundiram, N. Schneider, S. Massetti, M. Wedlund, A. López,
2017 Ariste, C. Barbieri, V. Mangano, and G. Cremonese (2009), Short-term variations
2018 of Mercury's Na exosphere observed with very high spectral resolution, *Geophys.*
2019 *Res. Lett.* *36*, L07201.
- 2020 Lepping, R. P., J. A. Jones, and L. F. Burlaga (1990), Magnetic field structure of
2021 interplanetary magnetic clouds at 1 Au, *J. Geophys. Res.*, *95*, 11,957–11,965.
- 2022 Lepping, R. P., D. H. Fairfield, J. Jones, L. A. Frank, W. R. Paterson, S. Kokubun,
2023 and T. Yamamoto (1995), Cross-tail magnetic flux ropes as observed by the
2024 Geotail spacecraft, *Geophys. Res. Lett.*, *22*, 10, 1193–1196.
- 2025 Lepping, R. P., J. A. Slavin, M. Hesse, J. A. Jones, and A. Szabo (1996), Analysis of
2026 magnetotail flux ropes with strong core fields: ISEE 3 observations, *J. Geomag.*
2027 *Geoelec.*, *48*, 589–601.
- 2028 Liljeblad, E., T. Sundberg, T. Karlsson, and A. Kullen (2014), Statistical
2029 investigation of Kelvin-Helmholtz waves at the magnetopause of Mercury, *J.*
2030 *Geophys. Res. (Space Physics)*, *119*, 9670-9683, doi: 10.1002/2014JA020614.
- 2031 Mall, U., E. Kirsch, K. Cierpka, B. Wilken, A. Söding, F. Neubauer, G. Gloeckler,
2032 and A. Galvin (1998), Direct observation of lunar pick-up ions near the Moon,
2033 *Geophys. Res. Lett.*, *25*, 3799–3802, doi:10.1029/1998GL900003.

2034 Mangano, V., A. Milillo, A. Mura, S. Orsini, E. De Angelis, A.M. Di Lellis, and P.
2035 Wurz (2007), The contribution of impulsive meteoritic impact vapourization to the
2036 Hermean exosphere, *Planet. Space Sci.*, *55*, 1541–1556.

2037 Mangano, V., S. Massetti, A. Milillo, A. Mura, S. Orsini, and F. Leblanc (2013),
2038 Dynamical evolution of sodium anisotropies in the exosphere of Mercury, *Planet.*
2039 *Space Sci.*, *82-83*, 1–10.

2040 Massetti, S., S. Orsini, A. Milillo, A. Mura, E. De Angelis, H. Lammer, and P. Wurz
2041 (2003), Mapping of the cusp plasma precipitation on the surface of Mercury,
2042 *Icarus*, *166*, 229–237.

2043 Masters, A., J. A. Slavin, G. A. DiBraccio, T. Sundberg, R. M. Winslow, C. L.
2044 Johnson, B. J. Anderson, and H. Korth (2013), A comparison of magnetic
2045 overshoots at the bow shocks of Mercury and Saturn, *J. Geophys. Res.*, *118*,
2046 doi:10.1002/jgra.50428.

2047 McClintock, W. E., R. J. Vervack, E. T. Bradley, R. M. Killen, N. Mouawad, A. L.
2048 Sprague, M. H. Burger, S. C. Solomon, and N. R. Izenberg (2009), MESSENGER
2049 observations of Mercury’s exosphere: Detection of magnesium and distribution of
2050 constituents, *Science*, *324*, 610–613.

2051 McGrath, M. A., R. E. Johnson, and L. J. Lanzerotti (1986), Sputtering of sodium on
2052 the planet Mercury, *Nature*, *323*, 694–696.

2053 McLain, J. L., A. L. Sprague, G. A. Grieves, D. Schriver, P. Travnicek, and T. M.
2054 Orlando (2011), Electron-stimulated desorption of silicates: A potential source for
2055 ions in Mercury’s space environment, *J. Geophys. Res.*, *116*, E03007,
2056 doi:10.1029/2010JE003714.

2057 McPherron, R. L., C. T. Russell, and M. P. Aubry (1973), Satellite studies of
2058 magnetospheric substorms on August 15, 1968: 9. Phenomenological model for
2059 substorms, *J. Geophys. Res.*, *78*, 3131–3149, doi:10.1029/JA078i016p03131.

2060 Milan, S. E., S. W. H. Cowley, M. Lester, D. M. Wright, J. A. Slavin, M. Fillingim,
2061 C. W. Carlson, and H. J. Singer (2004), Response of the magnetotail to changes in
2062 the open flux content of the magnetosphere, *J. Geophys. Res.*, *109*, A04220,
2063 doi:10.1029/2003JA010350.

2064 Milillo, A., et al. (2010), The BepiColombo mission: An outstanding tool for
2065 investigating the Hermean environment, *Planet. Space Sci.*, *58*, 40–60.

2066 Mitchell, D. G., D. J. Williams, C. Y. Huang, L. A. Frank, and C. T. Russell (1990),
2067 Current carriers in the near-Earth cross-tail current sheet during substorm growth
2068 phase, *Geophys. Res. Lett.*, *17*, 583.

2069 Moldwin, M. B. and W. J. Hughes (1992), On the formation and evolution of
2070 plasmoids: A survey of Isee-3 Geotail data, *J. Geophys. Res.*, *97*, 19,259–19,282.

2071 Mouawad, N., Burger, M. H. Killen, R. M. Potter, A. E. McClintock, W. E. Vervack,
2072 R. J. Bradley, E. T. Benna, M. Naidu, S. (2011), Constraints on Mercury’s Na
2073 exosphere: Combined MESSENGER and ground-based data, *Icarus*, *211*, 21–36.

2074 Müller, J., S. Simon, Y.-C. Wang, U. Motschmann, D. Heyner, J. Schüle, W.-H. Ip,
2075 G. Kleindienst, and G. J. Pringle (2012), Origin of Mercury’s double
2076 magnetopause: 3D hybrid simulation study with A.I.K.E.F., *Icarus*, *218*, 666–687,
2077 doi:10.1016/j.icarus.2011.12.028.

2078 Müller, M., S. F. Green, N. McBride, D. Koschny, J. C. Zarnecki, and M. S. Bentley
2079 (2002), Estimation of the dust flux near Mercury, *Planet. Space Sci.*, *50*, 1101–
2080 1115.

2081 Mura, A., A. Milillo, S. Orsini, and S. Massetti (2007), Numerical and analytical
2082 model of Mercury’s exosphere: Dependence on surface and external conditions,
2083 *Planet. Space Sci.*, *55*, 1569–1583.

2084 Mura, A., P. Wurz, H. I. M. Lichtenegger, H. Schleicher, H. Lammer, D. Delcourt, A.
2085 Milillo, S. Massetti, M. L. Khodachenko, and S. Orsini (2009), The sodium
2086 exosphere of Mercury: Comparison between observations during Mercury's transit
2087 and model results, *Icarus*, 200, 1–11.

2088 Ness, N. F., K. W. Behannon, R. P. Lepping, Y. C. Whang, and K. H. Schatten
2089 (1974), Magnetic field observations near Mercury: Preliminary Results from
2090 Mariner 10, *Science*, 185, 151–160.

2091 Ogilvie, K. W., J. D. Scudder, R. E. Hartle, G. L. Siscoe, H. S. Bridge, A. J. Lazarus,
2092 J. R. Asbridge, S. J. Bame, and C. M. Yeates (1974), Observations at Mercury
2093 encounter by Plasma Science Experiment on Mariner 10, *Science*, 185, 145–151.

2094 Ogilvie, K. W., J. D. Scudder, V. M. Vasylunas, R. E. Hartle, and G. L. Siscoe
2095 (1977), Observations at planet Mercury by Plasma Electron Experiment: Mariner
2096 10, *J. Geophys. Res.*, 82, 1807–1824.

2097 Orsini, S., S. Livi, K. Torkar, S. Barabash, A. Milillo, P. Wurz, A. M. Di Lellis, E.
2098 Kallio and the SERENA team (2010) Mg, , "**SERENA: a suite of four
2099 instruments (ELENA, STROFIO, PICAM and MIPA) on board
2100 BepiColombo-MPO for particle detection in the Hermean Environment,**
2101 BepiColombo Special Issue on Planetary and," *Planet. Space Science*,
2102 doi:10.1016/j.pss.2008.09.012, *Sci.* 58, (2010) 166-181,

2103 Orsini, S., V. Mangano, A. Mura, D. Turrini, S. Massetti, A. Milillo, and C. Plainaki
2104 (2014), The influence of space environment on the evolution of Mercury, *Icarus*,
2105 239, 281–290.

2106 Paral, J., P. M. Trávníček, K. Kabin, R. Rankin, and T. H. Zurbuchen (2009), Spatial
2107 distribution and energy spectrum of heavy ions in the Hermean magnetosphere
2108 with applications to MESSENGER flybys, *Adv. Geosci.*, 15, 1–16.

2109 Paral, J., P. M. Trávníček, R. Rankin, and D. Schriver (2010), Sodium ion exosphere
2110 of Mercury during MESSENGER flybys, *Geophys. Res. Lett.*, 37, L19102,
2111 doi:10.1029/2010GL044413.

2112 Paral, J. and R. Rankin (2013), Dawn-dusk asymmetry in the Kelvin-Helmholtz
2113 instability at Mercury, *Nature Communications*, 4, 1645- doi:
2114 10.1038/ncomms2676.

2115 Pflieger, M., H.I.M. Lichtenegger, P. Wurz, H. Lammer, E. Kallio, M. Alho, A. Mura,
2116 J.A. Martín-Fernández, M.L. Khodachenko, and S. McKenna-Lawlor, "**3D-
2117 modeling of Mercury's solar wind sputtered surface-exosphere environment,**"
2118 *Planet. Sp. Sci.* (2015), submitted.

2119 Poppe, A. R., J. S. Halekas, M. Sarantos, G. T. Delory (2013), The self-sputtered
2120 contribution to the lunar exosphere, *J. Geophys. Res.*, 118, 1934–1944.

2121 Potter, A., and T. H. Morgan (1985), Discovery of sodium in the atmosphere of
2122 Mercury, *Science*, 229, 651–653.

2123 Potter, A., and T. H. Morgan (1986), Potassium in the atmosphere of Mercury, *Icarus*
2124 67, 336–340.

2125 Potter, A., and T. H. Morgan (1997), Sodium and potassium atmospheres of Mercury,
2126 *Planet. Space Sci.*, 45, 95–100.

2127 Potter, A., R. M. Killen, and T. H. Morgan (1999), Rapid changes in the sodium
2128 exosphere of Mercury, *Planet. Space Sci.*, 47, 1441–1448.

2129 Potter, A. E., R. M. Killen, and M. Sarantos (2006), Spatial distribution of sodium on
2130 Mercury, *Icarus*, 181, 1–12.

2131 Potter, A., R. M. Killen, and T. H. Morgan (2002), The sodium tail of Mercury,
2132 *Meteor. Planet. Sci.*, 37, 1165–1172.

2133 Potter, A. E., R. M. Killen, and T. H. Morgan (2007), Solar radiation acceleration
2134 effects on Mercury sodium emission, *Icarus*, *186*, 571–580.

2135 Raeder, J., P. Zhu, Y. Ge, and G. Siscoe (2010), Open Geospace General Circulation
2136 Model simulation of a substorm: Axial tail instability and ballooning mode
2137 preceding substorm onset, *J. Geophys. Res.*, *115*, A00I16,
2138 doi:10.1029/2010JA015876.

2139 Raines, J. M., J. A. Slavin, T. H. Zurbuchen, G. Gloeckler, B. J. Anderson, D. N.
2140 Baker, H. Korth, S. M. Krimigis, and R. L. McNutt Jr. (2011), MESSENGER
2141 observations of the plasma environment near Mercury, *Planet. Space Sci.*, *59*,
2142 2004–2015, doi:10.1016/j.pss.2011.02.004.

2143 Raines, J. M., D. J. Gershman, T. H. Zurbuchen, M. Sarantos, J. A. Slavin, J. A.
2144 Gilbert, H. Korth, B. J. Anderson, G. Gloeckler, S. M. Krimigis, D. N. Baker, R. L.
2145 McNutt Jr., and S. C. Solomon (2013), Distribution and compositional variations
2146 of plasma ions in Mercury’s space environment: The first three Mercury years of
2147 MESSENGER observations, *J. Geophys. Res. Space Physics*, *118*, 1604–1619,
2148 doi:10.1029/2012JA018073.

2149 Raines, J. M., D. J. Gershman, J. A. Slavin, T. H. Zurbuchen, H. Korth, B. J.
2150 Anderson, and S. C. Solomon (2014), Structure and dynamics of Mercury’s
2151 magnetospheric cusp: MESSENGER measurements of protons and planetary ions,
2152 *J. Geophys. Res. Space Physics*, *119*, 6587–6602, doi:10.1002/2014JA020120.

2153 Richer, E., R. Modolo, C. Chanteur, S. Hess, and F. Leblanc (2012), A global hybrid
2154 model for Mercury’s interaction with the solar wind: Case study of the dipole
2155 representation, *J. Geophys. Res.*, *117*, doi:10.1029/2012JA017898.

2156 Runov, A., V. Angelopoulos, X.-Z. Zhou, X.-J. Zhang, S. Li, F. Plaschke, and J.
2157 Bonnell (2011), A THEMIS multicase study of dipolarization fronts in the
2158 magnetotail plasma sheet, *J. Geophys. Res.*, *116*, A05216,
2159 doi:10.1029/2010JA016316.

2160 Russell, C. T., and R. J. Walker (1985), Flux transfer events at Mercury, *J. Geophys.*
2161 *Res.*, *90*, 11067.

2162 Russell, C. T., D. N. Baker, and J. A. Slavin, The magnetosphere of Mercury, in
2163 *Mercury*, edited by F. Vilas, C. R. Chapman, and M. S. Matthews, pp. 514–561,
2164 Univ. of Ariz. Press, Tucson, 1988.

2165 Russell, C. T. (1989), ULF waves in the Mercury magnetosphere, *Geophys. Res.*
2166 *Lett.*, *16*, 1253–1256, doi: 10.1029/GL016i011p01253.

2167 Sarantos, M., P. H. Reiff, T. W. Hill, R. M. Killen, A. L. Urquhart (2001), A B_X-
2168 interconnected magnetosphere model for Mercury, *Planet. Space Sci.*, *49*, 1629–
2169 1635.

2170 Sarantos, M., J. A. Slavin, M. Benna, S. A. Boardsen, R. M. Killen, D. Schriver, and
2171 P. Trávníček (2009), Sodium-ion pickup observed above the magnetopause during
2172 MESSENGER’s first Mercury flyby: Constraints on neutral exospheric models,
2173 *Geophys. Res. Lett.*, *36*, L04106, doi:10.1029/2008GL036207.

2174 Sarantos, M., R. M. Killen, W. E. McClintock, E. T. Bradley, R. J. Vervack, M.
2175 Benna, and J. A. Slavin (2011), Limits to Mercury’s magnesium exosphere from
2176 MESSENGER second flyby observations, *Planet. Space Sci.*, *59*, 1992–2003.

2177 Sarantos, M., Hartle, R. E., Killen, R. M., Saito, Y., J. A., Slavin, and A. Glocer
2178 (2012), Flux estimates of ions from the lunar exosphere. *Geophys. Res. Lett.*, *39*,
2179 L13101, doi:10.1029/2012GL052001.

2180 Schmidt, C. A. (2013), Monte Carlo modeling of north-south asymmetries in
2181 Mercury’s sodium exosphere, *J. Geophys. Res.*, *118*, 4564–4571,
2182 doi:10.1002/jgra.50396.

2183 Schmidt, C. A., J. Baumgardner, M. Mendillo, and J. K. Wilson (2012), Escape rates
2184 and variability constraints for high-energy sodium sources at Mercury, *J. Geophys.*
2185 *Res.*, *117*, A03301, doi:10.1029/2011JA017217.

2186 Seki, K., N. Terada, M. Yagi, D. C. Delcourt, F. Leblanc, and T. Ogino (2013),
2187 Effects of the surface conductivity and IMF strength on the dynamics of planetary
2188 ions in Mercury's magnetosphere, *J. Geophys. Res.*, *118*, doi:10.1002/jgra.50181.

2189 Sergeev, V. A., M. Malkov, and K. Mursula (1993), Testing the isotropic boundary
2190 algorithm to evaluate the magnetic field configuration of the tail, *J. Geophys.*
2191 *Res.*, *98*, 7609.

2192 Shelley, E. G., R. G. Johnson, and R. D. Sharp (1972), Satellite observations of
2193 energetic heavy ions during a geomagnetic storm, *J. Geophys. Res.*, *77*, 6104.

2194 Shemansky, D. E., and A. L. Broadfoot (1977), Interaction of the surfaces of the
2195 Moon and Mercury with their exospheric atmospheres, *Rev. Geophys.*, *15*, 491–
2196 499, doi:10.1029/RG015i004p00491.

2197 Shiokawa, K., K. Yumoto, Y. Tanaka, T. Oguti, Y. Kiyama (1994), Low-latitude
2198 auroras observed at Moshiri and Rikubetsu (L=1.6) during magnetic storms on
2199 February 26, 27, 29, and May 10, 1992, *J. Geomag. Geoelec.*, *46*, 231–252.

2200 Simpson, J. A., J. H. Eraker, J. E. Lamport, and P. H. Walpole (1974), Electrons and
2201 protons accelerated in Mercury's magnetic field, *Science*, *185*, 160–166.

2202 Siscoe, G. L., N. F. Ness, and C. M. Yeates (1975), Substorms on Mercury?, *J.*
2203 *Geophys. Res.*, *80*, 4359–4363, doi:10.1029/JA080i031p04359.

2204 Slavin, J. A., and R. E. Holzer (1979), The effect of erosion on the solar wind stand-
2205 off distance at Mercury, *J. Geophys. Res.*, *84*, 2076–2082.

2206 Slavin, J. A., M. F. Smith, E. L. Mazur, D. N. Baker, T. Iyemori, H. J. Singer, and E.
2207 W. Greenstadt (1992), ISEE-3 plasmoid and TCR observations during an extended
2208 interval of substorm activity, *Geophys. Res. Lett.*, *19*, 825–828.

2209 Slavin, J. A., M. F. Smith, E. L. Mazur, D. N. Baker, E. W. Hones, T. Iyemori, and E.
2210 W. Greenstadt (1993), ISEE-3 observations of traveling compression regions in the
2211 Earth's magnetotail, *J. Geophys. Res.*, *98*, 15,425–15,446.

2212 Slavin, J. A., R. P. Lepping, J. Gjerloev, D. H. Fairfield, M. Hesse, C. J. Owen, M. B.
2213 Moldwin, T. Nagai, A. Ieda, and T. Mukai (2003), Geotail observations of
2214 magnetic flux ropes in the plasma sheet, *J. Geophys. Res.*, *108*, 1015,
2215 doi:10.1029/2002JA009557.

2216 Slavin, J. A., E. I. Tanskanen, M. Hesse, C. J. Owen, M. W. Dunlop, S. Imber, E. A.
2217 Lucek, A. Balogh, and K.-H. Glassmeier (2005), Cluster observations of traveling
2218 compression regions in the near-tail, *J. Geophys. Res.*, *110*, A06207,
2219 doi:10.1029/2004JA010878.

2220 Slavin, J. A., R. P. Lepping, J. Gjerloev, D. H. Fairfield, M. Hesse, C. J. Owen, M. B.
2221 Moldwin, T. Nagai, A. Ieda, and T. Mukai (2007), MESSENGER: Exploring
2222 Mercury's magnetosphere, *Space Sci. Rev.*, *131*, 133–160.

2223 Slavin, J. A., et al. (2008), Mercury's magnetosphere after MESSENGER's first
2224 flyby, *Science*, *321*, 85–89, doi:10.1126/science.1159040.

2225 Slavin, J. A., et al. (2009), MESSENGER observations of magnetic reconnection in
2226 Mercury's magnetosphere, *Science*, *324*, 606–610.

2227 Slavin, J. A., et al. (2010), MESSENGER observations of extreme loading and
2228 unloading of Mercury's magnetic tail, *Science*, *329*, 665–668.

2229 Slavin, J. A., et al. (2012a), MESSENGER and Mariner 10 flyby observations of
2230 magnetotail structure and dynamics at Mercury, *J. Geophys. Res.*, *117*, A01215,
2231 doi:10.1029/2011JA016900.

2232 Slavin, J. A., et al. (2012b), MESSENGER observations of a flux-transfer-event
2233 shower at Mercury, *J. Geophys. Res.*, *117*, A00M06, doi:10.1029/JA017926.

2234 Slavin, J. A., G. A. DiBraccio, D. J. Gershman, S. M. Imber, G. K. Poh, T. H.
2235 Zurbuchen, X. Jia, D. N. Baker, S. A. Boardsen, M. Sarantos, T. Sundberg, A.
2236 Masters, C. L. Johnson, R. M. Winslow, B. J. Anderson, H. Korth, R. L. McNutt
2237 Jr., and S. C. Solomon (2014), MESSENGER observations of Mercury's
2238 magnetosphere under extreme solar wind conditions, *J. Geophys. Res. Space*
2239 *Physics*, *119*, 8087–8116, doi:10.1002/2014JA020319.

2240 Smith, M. F., and M. Lockwood (1996), Earth's magnetospheric cusps, *Rev.*
2241 *Geophys.*, *34*, 233–260, doi: 10.1029/96RG00893.

2242 Smith, D. E., et al. (2012), Gravity field and internal structure of Mercury from
2243 MESSENGER, *Science*, *336*, 214–271, doi:10.1126/science.1218809.

2244 Smyth, W. H., and M. L. Marconi (1995), Theoretical overview and modeling of the
2245 sodium and potassium atmospheres of Mercury, *Astrophys. J.*, *441*, 839–864.

2246 Solomon, S. C., R. L. McNutt, R. E. Gold, and D. L. Domingue (2007),
2247 MESSENGER: Mission Overview, *Space Sci. Rev.*, *131*, 3–39.

2248 Speiser, T. W. (1965), Particle trajectory in model current sheets: 1. Analytical
2249 solutions, *J. Geophys. Res.*, *70*, 4219.

2250 Sprague, A. L., R. W. H. Kozlowski, D. M. Hunten, N. M., Schneider, D. L.
2251 Domingue, W. K. Wells, W. Schmitt, and U. Fink (1997), Distribution and
2252 abundance of sodium in Mercury's atmosphere, *Icarus*, *129*, 506–527.

2253 Stern, S. A. (1999), The lunar atmosphere: history, status, current problems, and
2254 context, *Rev. Geophys.*, *37*, 453–491.

2255 Strangeway, R. J., C. T. Russell, J. G. Luhmann, T. E. Moore, J. C. Foster, S. V.
2256 Barabash, and H. Nilsson (2010), Does a planetary-scale magnetic field enhance or
2257 inhibit ionospheric plasma outflows? AGU Fall Meeting Abstracts, 1893.

2258 Suess, S. T., and B. E. Goldstein (1979), Compression of the Hermean magnetosphere
2259 by the solar wind, *J. Geophys. Res.*, *84*, 3306–3312.

2260 Sundberg, T., S. A. Boardsen, J. A. Slavin, L. G. Blomberg, and H. Korth (2010), The
2261 Kelvin-Helmholtz instability at Mercury: An assessment, *Planet. Space Sci.*, *58*,
2262 1434–1441, doi:10.1016/j.pss.2010.06.008.

2263 Sundberg, T., S. A. Boardsen, J. A. Slavin, L. G. Blomberg, J. A. Cumnock, S. C.
2264 Solomon, B. J. Anderson, and H. Korth (2011), Reconstruction of propagating
2265 Kelvin-Helmholtz vortices at Mercury's magnetopause, *Planet. Space Sci.*, *59*,
2266 2051–2057.

2267 Sundberg, T., S. A. Boardsen, J. A. Slavin, B. J. Anderson, H. Korth, T. H.
2268 Zurbuchen, J. M. Raines, and S. C. Solomon (2012), MESSENGER orbital
2269 observations of large-amplitude Kelvin-Helmholtz waves at Mercury's
2270 magnetopause, *J. Geophys. Res.*, *117*, A04216, doi:10.1029/2011JA017268.

2271 Trávníček, P., P. Hellinger, and D. Schriver (2007), Structure of Mercury's
2272 magnetosphere for different pressure of the solar wind: Three dimensional hybrid
2273 simulations, *Geophys. Res. Lett.*, *34*, 5104, doi: 10.1029/2006GL028518.

2274 Trávníček, P., et al. (2010), Mercury's magnetosphere-solar wind interaction for
2275 northward and southward interplanetary magnetic field: Hybrid simulation results,
2276 *Icarus*, *209*, doi: 10.1016/j.icarus.2010.01.008.

2277 Vervack, R. J., W. E. McClintock, R. M. Killen, A. L. Sprague, B. J. Anderson, M. H.
2278 Burger, E. T. Bradley, N. Mouawad, S. C. Solomon, and N. R. Izenberg (2010),
2279 Mercury's complex exosphere: Results from MESSENGER's third flyby, *Science*,
2280 *329*, 672–675, doi:10.1126/science.1188572.

2281 Vervack, R. J., W. E. McClintock, R. M. Killen, A. L. Sprague, M. H. Burger, A. W.
2282 Merkel, and M. Sarantos (2011), MESSENGER searches for less abundant or
2283 weakly emitting species in Mercury's Exosphere, AGU Fall Meeting Abstracts A2.
2284 Vilas, F., C. R. Chapman, and M. S. Mathews (1988), *Mercury*, Univ. Arizona Press,
2285 Tucson, AZ.

2286 Wang, Y.-C., and W.-H. Ip (2011), Source dependency of exospheric sodium on
2287 Mercury, *Icarus*, 216, 387–402, doi:10.1016/j.icarus.2011.09.023.

2288 Wang, Y.-C., J. Mueller, U. Motschmann, and W.-H. Ip (2010), A hybrid simulation
2289 of Mercury's magnetosphere for the MESSENGER encounters in year 2008,
2290 *Icarus*, 209, 10.1016/j.icarus.2010.05.020.

2291 Wang, Y. X., F. Ohuchi, and P. H. Holloway (1984), Mechanisms of electron
2292 stimulated desorption from soda-silica glass surfaces, *J. Vac. Sci. Technol. A*, 2(2),
2293 732–737, doi:[10.1116/1.572560](https://doi.org/10.1116/1.572560).

2294 Winglee, R. M., E. Harnett, and A. Kidder (2009), Relative timing of substorm
2295 processes as derived from multifluid/multiscale simulations: Internally driven
2296 substorms, *J. Geophys. Res.*, 114, A09213, doi:10.1029/2008JA013750.

2297 Winslow, R. M., C. L. Johnson, B. J. Anderson, H. Korth, J. A. Slavin, M. E.
2298 Purucker, and S. C. Solomon (2012), Observations of Mercury's northern cusp
2299 region with MESSENGER's Magnetometer, *Geophys. Res. Lett.*, 39, L08112,
2300 doi:10.1029/2012GL051472.

2301 Winslow, R. M., B. J. Anderson, C. L. Johnson, J. A. Slavin, H. Korth, M. E.
2302 Purucker, D. N. Baker, and S. C. Solomon (2013), Mercury's magnetopause and
2303 bow shock from MESSENGER Magnetometer observations, *J. Geophys. Res.*,
2304 118, 2213–2227, doi:10.1002/jgra.50237.

2305 Winslow, R. M., et al. (2014), Mercury's surface magnetic field determined from
2306 proton-reflection magnetometry, *Geophys. Res. Lett.*, 41, 4463–4470,
2307 doi:10.1002/2014GL060258.

2308 Wurz, P., and L. Blomberg (2001), Particle populations in Mercury's magnetosphere,
2309 *Planet. Space Sci.*, 49, 1643–1653.

2310 Wurz, P., and H. Lammer (2003), Monte-Carlo simulation of Mercury's exosphere,
2311 *Icarus*, 164, 1–13.

2312 Wurz, P., J. A. Whitby, U. Rohner, J. A. Martín-Fernández, H. Lammer, and C. Kolb
2313 (2010), Self-consistent modelling of Mercury's exosphere by sputtering, micro-
2314 meteorite impact and photon-stimulated desorption, *Planet. Space Sci.*, 58, 1599–
2315 1616.

2316 Wurz, P., U. Rohner, J. A. Whitby, C. Kolb, H. Lammer, P. Dobnikar, and J. A.
2317 Martín-Fernández (2007), The Lunar exosphere: The sputtering contribution,
2318 *Icarus*, 191, 486–496, doi:10.1016/j.icarus.2007.04.034.

2319 Yagi, M., K. Seki, Y. Matsumoto, D. C. Delcourt, and F. Leblanc (2010), Formation
2320 of a sodium ring in Mercury's magnetosphere, *Journ. Geophys. Res.*, 115, A10,
2321 doi:10.1029/2009JA015226.

2322 Yakshinskiy, B. V., and T. E. Madey (1999), Photon-stimulated desorption as a
2323 substantial source of sodium in the lunar atmosphere, *Nature*, 400, 642.

2324 Yakshinskiy, B. V. and T. E. Madey (2005), Temperature-dependent DIET of alkalis
2325 from SiO₂ films: Comparison with a lunar sample, *Surf. Sci.*, 593, 202–209.

2326 Yakshinskiy, B. V., and T. E. Madey (2004), Photon-stimulated desorption of Na
2327 from a lunar sample: temperature-dependent effects, *Icarus*, 168, 53–59.

2328 Yakshinskiy, B. V., T. E. Madey, and V. N. Ageev (2000), Thermal desorption of
2329 sodium atoms from thin SiO₂ films, *Surf. Rev. Lett.*, 7, 75–87.

- 2330 Yau, A. W., A. Howarth, W. K. Peterson, and T. Abe (2012), Transport of thermal-
2331 energy ionospheric oxygen (O^+) ions between the ionosphere and the plasma sheet
2332 and ring current at quiet times preceding magnetic storms, *J. Geophys. Res.*, *117*,
2333 doi:10.1029/2012JA017803.
- 2334 Zurbuchen, T. H., et al. (2011), MESSENGER observations of the spatial distribution
2335 of planetary ions near Mercury, *Science*, *333*, 1862.
- 2336 Zurbuchen, T. H., J. M. Raines, G. Gloeckler, S. M. Krimigis, J. A. Slavin, P. L.
2337 Koehn, R. M. Killen, A. L. Sprague, R. L. McNutt Jr., and S. C. Solomon (2008),
2338 MESSENGER observations of the composition of Mercury's ionized exosphere
2339 and plasma environment, *Science*, *321*, 90–92, doi:10.1126/science.1159314.
- 2340 Zwan, B. J., and R. A. Wolf (1976), Depletion of solar wind plasma near a planetary
2341 boundary, *J. Geophys. Res.*, *81*, 1636–1648.